UNIVERSITÀ DEGLI STUDI DELL'AQUILA

DIPARTIMENTO DI INGEGNERIA INDUSTRIALE, DELL'INFORMAZIONE E DI ECONOMIA

in co-tutela con la Vrije Universiteit Brussel (Belgio)

Dottorato di Ricerca in Ingegneria Industriale dell'Informazione e di Economia

Curriculum Ingegneria elettrica, elettronica e dell'informazione

XXXVII ciclo

Titolo della tesi

Advanced Model Order Reduction Techniques for Delayed PEEC Models

SSD IIET-01/A

Dottorando:

Muhammad Altaf Khattak

Coordinatore del corso:

Prof. Katia Gallucci

Tutors:

Prof. Giulio Antonini

Prof. Francesco Ferranti

a.a. 2023/2024

Table of Contents

Abstract **vi**

Description of the Thesis **viii**

Acknowledgments **ix**

List of abbreviations **1**

1 Introduction **1**
1.1 The need for model order reduction 2
1.2 Motivation for the research 2
1.3 Problem statement 3
1.4 Objectives 3
1.5 Thesis organization 4

2 The PEEC method **5**
2.1 Integral formulation of Maxwell's equations 6
2.1.1 Choice of the basis and weighting functions for the conductor surfaces 10
2.1.2 Choice of the basis and weighting functions for the conductor volumes 11
2.2 Development of equivalent circuit models 14
2.2.1 Model for electric field coupling 14
2.2.2 Model for magnetic field coupling 16
2.2.3 PEEC equivalent circuit 17
2.2.4 Enforcement of Kirchhoff's current and voltage laws 17
2.3 Computation of partial elements 19
2.3.1 Computation of partial inductances 19
2.3.2 Computation of coefficients of potential 22

2.4 Dielectrics modeling . . . 27
2.4.1 External incident electric fields . . . 32
2.5 Analysis of PEEC models . . . 33
2.5.1 Frequency domain solver . . . 33
2.5.2 Time domain solver . . . 33

3 The concept of model order reduction 36
3.1 Formulation of reduced order model . . . 37
3.2 Proper orthogonal decomposition . . . 40
3.3 Moment matching based MOR . . . 41
3.3.1 Padé and Padé-type approximation . . . 42
3.3.2 Krylov subspace and IRKA . . . 43
3.3.3 Tangential interpolation based MOR . . . 43
3.4 Balanced truncation . . . 44
3.5 Loewner framework . . . 46

4 Reduced order modeling of the delayed PEEC models 47
4.1 MOR of full-wave PEEC models . . . 48
4.2 Mutlipoint moment matching technique for delayed PEEC model . . 52

5 MOR of delayed PEEC models using POD techniques 55
5.1 Frequency domain proper orthogonal decomposition . . . 56
5.2 Incremental POD in frequency domain . . . 57
5.3 Numerical results . . . 59
5.3.1 L-shaped conductor over a ground plane . . . 61
5.3.2 Two coplanar microstrips . . . 68

6 Derivatives-enhanced POD-based MOR for delayed PEEC models 82
6.1 Proper orthogonal decomposition and frequency-domain derivatives . 83
6.2 Numerical results . . . 84
6.2.1 L-shaped conductor example . . . 84
6.2.2 Two microstrip interconnection . . . 88

7 Conclusions and future work 93
7.1 Summary of contributions . . . 93
7.1.1 Proper orthogonal decomposition-based model order reduction 93
7.1.2 Derivative-enhanced proper orthogonal decomposition . . . 94
7.1.3 Comparison with multipoint moment matching . . . 94
7.2 Future work . . . 94
7.2.1 Optimal selection of snapshots . . . 94
7.2.2 Higher derivative snapshots incorporation . . . 94

7.2.3 Extension to nonlinear systems 95
7.2.4 Parameterized model order reduction 95
7.2.5 Error estimators and bounds for ROMs 95
7.3 Final remarks 95

A List of publications **96**

Bibliography **98**

Vita **114**

Abstract

The partial element equivalent circuit (PEEC) is a relatively popular computational technique in electromagnetics (EM) because it can model electromagnetic phenomena as equivalent circuits. It is used in many areas such as interconnect modeling, antenna and integrated circuit design, signal integrity analysis, and electromagnetic compatibility (EMC) assessment. The PEEC technique is based on transforming the Maxwell's equations into circuit representations which makes it easier to analyze complex EM systems. Certain quasi-static PEEC models can be represented by a set of ODEs, and for some systems with negligible propagation delays, this works well. PEEC models with time delays become necessary to model electrically large and complicated structures that are severely affected by signal propagation delays. These models incorporate time delays through neutral delayed differential equations (NDDEs), which accurately capture the electromagnetic behavior of large-scale systems.

Despite its advantages, the PEEC method often leads to high-dimensional state-space representations. Simulation of such systems result in high computational cost and memory requirement. To overcome the challenge of high computational requirements, model order reduction (MOR) techniques are essential. MOR techniques enable the reduction of complex dynamical models while preserving their input-output behavior, significantly improving computational efficiency without sacrificing accuracy.

This PhD research aims to develop advanced MOR techniques specifically for delayed PEEC models. The focus is on Proper Orthogonal Decomposition (POD)-based MOR approaches, which have been widely used in various scientific and engineering applications. This work introduces two POD-based MOR strategies that use frequency-domain snapshots of the system's transfer function to generate reduced-order models (ROMs). These methods are then compared with another MOR technique based on multipoint moment matching which proves their effectiveness in both frequency-domain and time-domain simulations.

To further enhance the performance of POD-based MOR, this research modifies the snapshot collection process by incorporating frequency-domain derivatives of the transfer function. By including derivative snapshots, the reduced-order models achieve higher accuracy while simultaneously reducing computational complexity during the construction phase. This innovation allows for a more efficient reduction process, ensuring that the important features of the original system are well-preserved with fewer basis vectors.

The effectiveness of these proposed techniques is validated through extensive numerical examples covering a wide range of test cases in both frequency and time-domain. The results demonstrate significant improvements in computational efficiency, achieving faster simulations while maintaining high accuracy in predicting the system behavior. The study also provides a comparative analysis between different MOR techniques which provide the trade-offs among accuracy, efficiency, and computational cost.

Beyond theoretical contributions, this research has practical implications in the field of computational electromagnetics. The development of efficient MOR techniques for delayed PEEC models facilitates faster and more accurate simulations which makes it possible to analyze large-scale EM systems easily. This work extends the applicability of delayed PEEC models to more complex EM problems, contributing to advancements in high-frequency interconnect modeling, EM propagation problems, signal integrity analysis, power electronics, and EMC studies.

In summary, this research marks a significant advancement in applying MOR techniques to PEEC models, particularly those formulated with NDDEs. The proposed POD-based methods, enhanced with derivative-based snapshots, provide an efficient solution for reducing the computational complexity of PEEC simulations. Future research could explore multiple directions as including design parameters into the MOR process and extensions to nonlinear systems. Ultimately, this study contributes to the advancement of electromagnetic simulations, enabling faster, more efficient, and scalable computational methods for practical engineering applications.

Description of the Thesis

The thesis deals with the model order reduction (MOR) of the partial element equivalent circuit (PEEC) method to make simulations more efficient. In particular, several contributions have been made to make the simulation of PEEC models efficient.
The thesis is organized as follows:

Chapter 1 explains the structure and outline of the thesis.

Chapter 2 summarizes the construction of the delayed PEEC model, focusing on both electromagnetic compatibility (EMC) and computational electromagnetics (CEM) problems. Starting from Maxwell's equations, we explain the steps to develop a delayed PEEC model using a typical delayed linear state-space formulation. Different numerical schemes for simulating the delayed PEEC model are also presented.

Chapter 3 introduces the basic concept of MOR, explaining various techniques.

Chapter 4 discusses MOR of delayed PEEC models. Previously available techniques for the MOR of delayed PEEC models have also been reviewed.

Chapter 5 presents a novel approach to MOR based on proper orthogonal decomposition (POD) in the frequency-domain. Collecting snapshots in the frequency-domain for POD-based MOR is explained. A method is introduced to avoid the one-shot singular value decomposition (SVD) of large matrices. The proposed techniques have been validated using several numerical examples.

In Chapter 6, the POD-based MOR for the delayed PEEC model is further enhanced, with improvements demonstrated in the snapshot collection process. These improvements have been shown through different numerical examples.

Finally, Chapter 7 summarizes the key conclusions of this research and outlines potential directions for future work.

Acknowledgments

I am deeply grateful to Prof. Giulio Antonini and Prof. Francesco Ferranti for their invaluable support throughout my doctorate. I could not have achieved this without your guidance and encouragement. I also sincerely thank Dr. Daniele Romano for providing the necessary data and for his collaboration.

I am profusely thankful to my beloved parents, who raised me and supported me through every step of my life.

Special thanks to my Wife, Leena Khan, for her love and unwavering trust in me.

Lastly, I would like to thank all my friends in L'Aquila who stood by me through every thick and thin during my stay in L'Aquila.

List of abbreviations

Below, the list of abbreviations that has been used throughout this thesis, can be found. This list is made per chapter to show where each abbreviation appears first. No new entry will be made if a certain abbreviation returns in a later chapter.

$PEEC$	Partial element equivalent circuit
EMC	Electromagnetic compatibility
EMI	Electromagnetic interference
$MPIE$	Mixed potential integral equation
FEM	Finite element method
MoM	Method of moments
PCB	Printed circuit board
PDN	Power distribution network
$SPICE$	Simulation program with integrated circuit emphasis
ACA	Adaptive cross approximation
ROM	Reduced order model
$ODEs$	Ordinary differential equations
MQS	Magneto-quasi-static
$NDDE$	Neutral delay differential equation
MOR	Model order reduction
FOM	Full order model
ROM	Reduced order model
SVD	Singular value decomposition
POD	Proper orthogonal decomposition
LTI	Linear time-invariant
$IRKA$	Iterative rational Krylov algorithm
$Krylov$	Krylov subspace method
CFD	Computational fluid dynamics
$SISO$	Single input single output
$MIMO$	Multiple input multiple output
MNA	Modified nodal analysis
$NDDE$	Neutral delay differential equation
$FD-POD$	Frequency domain proper orthogonal decomposition
$MM-mp$	Multipoint expansion moment matching
$INCR-FDPOD$	Incremental singular value decomposition
$INCR-SVD$	Incremental singular value decomposition
$FDPOD-D$	Frequency domain proper orthogonal decomposition with derivatives

Chapter 1

Introduction

Electromagnetic and circuit simulation and modeling play a critical role in the design and analysis of modern electronic systems, as they enable accurate predictions of the electromagnetic behavior, signal integrity, and power distribution in complex circuits. The increasing complexity of electronic devices, such as high-speed digital circuits, integrated RF components, and power electronic systems, has led to a growing demand for computationally efficient methods that can accurately model electromagnetic interactions.

One of the widely used techniques for electromagnetic modeling is the partial element equivalent circuit (PEEC) method, which provides a circuit-based representation of electromagnetic interactions [1–3]. Unlike full-wave numerical methods, such as the finite element method (FEM) or the method of moments (MoM), the PEEC method offers a natural integration with circuit solvers, making it a preferred choice for co-simulation of electromagnetic and circuit components. By discretizing Maxwell's equations, the PEEC method converts the electromagnetic problem into an equivalent lumped-element circuit, consisting of inductances, capacitances, and resistances. This enables engineers to analyze complex electromagnetic interactions using circuit simulation tools, leading to more intuitive and computationally manageable solutions.

However, as modern electronic systems continue to evolve, the number of elements in PEEC models grows exponentially, resulting in large-scale systems that require significant computational resources. In practical applications, PEEC models for complex structures, such as printed circuit boards (PCBs), power distribution networks (PDNs), and on-chip interconnects, may consist of thousands or even millions of unknowns. The computational burden associated with solving such large-scale systems, especially in transient and frequency domain simulations, can become a major bottleneck in the design and verification process. Moreover, the presence of delays (i.e., time retardation effects) in PEEC models further complicates the nu-

merical solution, making standard simulation techniques inefficient or infeasible for many applications.

1.1 The need for model order reduction

To address the computational challenges posed by large-scale PEEC models, model order reduction (MOR) techniques have emerged as an essential tool for reducing the dimensionality of complex systems while preserving their essential dynamic behavior. The primary goal of MOR is to generate a reduced order model (ROM) that approximates the original system with significantly fewer degrees of freedom, thereby enabling faster simulations without compromising accuracy. Over the years, various MOR techniques have been developed, including Krylov subspace methods, moment matching techniques, balanced truncation, and projection based methods. These approaches have been successfully applied to a wide range of engineering problems, including circuit simulation, structural dynamics, and fluid dynamics.
Among the available MOR techniques, proper orthogonal decomposition (POD) has gained considerable attention due to its ability to efficiently extract dominant information from large-scale datasets. POD is a data-driven approach that constructs a reduced order basis by analyzing a set of system snapshots obtained from high fidelity simulations. This method is particularly advantageous for reducing electromagnetic models, as it allows the identification of dominant electromagnetic information that capture the key dynamical features of the system.
However, while POD based MOR has demonstrated great success in reducing the computational complexity of large-scale models, its application to delayed systems, such as delayed PEEC models, remains a challenging research problem. Traditional MOR methods often fail to efficiently handle systems with retarded (delayed) differential equations, which arise naturally in electromagnetic interactions due to the finite speed of light. The presence of delays introduces memory effects, making conventional reduction techniques less effective. This has motivated researchers to explore enhanced MOR techniques capable of addressing the unique challenges posed by delayed differential systems.

1.2 Motivation for the research

In electromagnetic modeling, particularly in the PEEC framework, incorporating delays is crucial for accurately capturing effects in electrically large/long systems where distributed phenomena cannot be neglected. For instance, in high frequency circuits and power electronic systems, ignoring delay effects can lead to significant inaccuracies in transient and frequency-domain analyses. Therefore, developing ef-

ficient and robust MOR techniques that can handle delayed PEEC models is an urgent research need.
This thesis aims to advance the application of POD-based MOR techniques to efficiently reduce the complexity of delayed PEEC models while preserving their essential characteristics. By leveraging mathematical techniques, such as frequency-domain snapshots and efficient singular value decomposition (SVD) strategies, this research seeks to develop a novel framework that can significantly improve the computational efficiency of delayed PEEC models by novel dedicated MOR techniques. Moreover, the methodologies developed in this work can be extended to other domains involving delayed differential equations, such as electromagnetic wave propagation in electrically large/long structures, circuit design with increasingly higher operating frequencies, and power system simulations. By addressing the computational challenges associated with large-scale and delayed systems, this research contributes to the development of more efficient simulation framework.

1.3 Problem statement

As circuit complexity increases, solving large-scale PEEC models becomes computationally expensive, particularly when delay effects are present. Traditional MOR methods may not efficiently handle these delays, leading to reduced accuracy or increased computational cost. The key research question addressed in this thesis to explore and develop new MOR methodologies that can work for delayed PEEC models.

1.4 Objectives

The primary objectives of this thesis have been:

1. To analyze the limitations of existing MOR techniques for delayed PEEC models.

2. To develop frequency-domain POD approaches to efficiently construct reduced order delayed PEEC models using different SVD-based approaches.

3. To incorporate derivative snapshots in the frequency-domain POD framework to improve the ROM accuracy without affecting the computational cost needed for its generation.

4. To validate the proposed methodologies through several numerical examples.

1.5 Thesis organization

The remainder of this thesis is structured as follows:

- Chapter 2 summarizes the construction of delayed PEEC models, focusing on both electromagnetic compatibility (EMC) and computational electromagnetics (CEM) problems. Starting from Maxwell's equations, we explain the steps to develop a delayed PEEC model using a typical delayed linear state space formulation. Different numerical schemes for simulating the delayed PEEC model are also presented.
- Chapter 3 introduces the basic concept of MOR, explaining various techniques.
- Chapter 4 discusses the formulation of ROMs of delayed PEEC models. Previously available techniques for the MOR of delayed PEEC models have also been reviewed.
- Chapter 5 presents two novel POD-based MOR approaches in the frequency-domain for delayed PEEC models. How to collect snapshots in the frequency-domain for this technique is explained. Also, an approach is introduced to avoid the one-shot SVD of large matrices based on an incremental strategy. The proposed techniques have been validated using several numerical examples.
- Chapter 6 presents the inclusion of frequency-domain derivatives snapshots in the POD scheme to improve the ROM accuracy without affecting the computational cost needed for its generation. These improvements have been shown through different numerical examples.
- Chapter 7 summarizes the key conclusions of this research and outlines potential directions for future work.

By addressing the computational challenges in large-scale electromagnetic simulations, this research aims to contribute to the development of more efficient and accurate MOR techniques, benefiting both academia and industry in the field of circuit and electromagnetic modeling.

Chapter 2

The PEEC method

Among the numerical techniques built to solve Maxwell's equations in order to analyze interference problems or design less susceptible to interference systems, the PEEC method has proven to be very effective in modeling interconnects composed of conductors and dielectrics and well suited to represent parasitic effects, either conductive or radiated, which are the common sources of EMC/EMI problems [1–3]. The PEEC method was initially developed to address inductive effects in interconnects within free space [4], commonly referred to as magneto-quasistatic (MQS) PEEC. However, this general integral-equation-based approach was later expanded to account for capacitive effects [5] and full-wave phenomena [6]. Recent advancements have extended the method to include dielectric and magnetic materials [7–17]. The primary difference between the PEEC method and other integral equation-based techniques, i.e., the Method of Moments (MoM) [18], lies in its ability to offer a circuit-based interpretation of the Mixed Potential Integral Equation (MPIE) [19]. This interpretation is achieved through partial elements, including resistances, partial inductances, and coefficients of potential. As a result, the equivalent circuit derived from the PEEC method can be analyzed using SPICE-like circuit solvers [20] in both the time and frequency domains.

Over the years, numerous advancements have been made to the PEEC method, enabling it to address complex problems involving the interplay between circuits and electromagnetic fields [6, 9, 10, 21–32].

To accelerate the analysis of equivalent circuits, fast multipole-based techniques [33] and the adaptive cross approximation (ACA) method [34–39] have been employed. Additionally, effective model reduction techniques [40–46] can be utilized to create compact models, also known as ROMs, that maintain accuracy at the ports while preserving the physical properties of the original system. Other approaches are discussed in [28, 45, 47–50].

The volumes and surfaces are discretized into elementary regions using the conven-

tional approach, specifically hexahedra and quadrilateral patches, respectively [25]. Current and charge densities are expanded within these regions using a series of basis functions. Pulse basis functions are typically used as both expansion and weighting functions. This choice implies constant current density over the elementary volume (inductive cells) and constant charge density over the surface (capacitive cells). Using the standard Galerkin testing procedure, topological elements such as nodes and branches are generated, and electrical lumped elements are identified to model the coupling of magnetic and electric fields. Conductors are represented by their ohmic resistance, while dielectrics are modeled by accounting for the excess charge resulting from dielectric polarization [7]. The coupling of magnetic and electric fields is described using partial inductances and coefficients of potential, respectively.
The purpose of this chapter is to provide a comprehensive overview of the PEEC method, beginning with Maxwell's Equations.

2.1 Integral formulation of Maxwell's equations

The Maxwell differential equations in the time domain [19] are given by

$$\nabla \times \boldsymbol{H}(\boldsymbol{r},t) = \frac{\partial \boldsymbol{D}(\boldsymbol{r},t)}{\partial t} + \boldsymbol{J}(\boldsymbol{r},t) \tag{2.1}$$

$$\nabla \times \boldsymbol{E}(\boldsymbol{r},t) = -\frac{\partial \boldsymbol{B}(\boldsymbol{r},t)}{\partial t} \tag{2.2}$$

$$\nabla \cdot \boldsymbol{B}(\boldsymbol{r},t) = 0 \tag{2.3}$$

$$\nabla \cdot \boldsymbol{D}(\boldsymbol{r},t) = q(\boldsymbol{r},t) \tag{2.4}$$

where $q(\boldsymbol{r},t)$ denotes the charge density and $\boldsymbol{J}(\boldsymbol{r},t)$ represents the current density; the fields $\boldsymbol{H}, \boldsymbol{B}, \boldsymbol{E}$ and $\boldsymbol{D}$ are governed by the following constitutive relations

$$\boldsymbol{B}(\boldsymbol{r},t) = \mu_0 \mu_r \boldsymbol{H}(\boldsymbol{r},t) \tag{2.5}$$

$$\boldsymbol{D}(\boldsymbol{r},t) = \varepsilon_0 \varepsilon_r \boldsymbol{E}(\boldsymbol{r},t) \tag{2.6}$$

where μ_r and ε_r represent the relative permeability and permittivity, respectively. It is useful to express fields in terms of potential. From the solenoidality of $\boldsymbol{B}$ in Eq. (2.3), the magnetic vector potential is defined as

$$\boldsymbol{B}(\boldsymbol{r},t) = \nabla \times \boldsymbol{A}(\boldsymbol{r},t). \tag{2.7}$$

Substituting (2.7) into (2.2), we obtain

$$\nabla \times \left(\boldsymbol{E}(\boldsymbol{r},t) + \frac{\partial \boldsymbol{A}(\boldsymbol{r},t)}{\partial t} \right) = \boldsymbol{0}. \tag{2.8}$$

This equation allows us to define the electric scalar potential $\boldsymbol{\Phi}(\boldsymbol{r},t)$ in such a way that

$$\boldsymbol{E}(\boldsymbol{r},t)+\frac{\partial \boldsymbol{A}(\boldsymbol{r},t)}{\partial t}=-\nabla\Phi(\boldsymbol{r},t). \tag{2.9}$$

Such an equation connects the electric field $\boldsymbol{E}$ with the potentials $\boldsymbol{A}$ and Φ. Next, we express such potentials $\boldsymbol{A}$ and Φ in terms of $\boldsymbol{J}$ and q, respectively. To this aim, by substituting (2.7) and (2.9) into (2.1), we obtain

$$\nabla\times\nabla\times\boldsymbol{A}(\boldsymbol{r},t)=\mu_0\varepsilon_0\frac{\partial}{\partial t}\left(-\frac{\partial \boldsymbol{A}(\boldsymbol{r},t)}{\partial t}-\nabla\Phi(\boldsymbol{r},t)\right)-\mu_0\boldsymbol{J}(\boldsymbol{r},t). \tag{2.10}$$

By applying the Laplacian identity

$$\nabla\times\nabla\times\boldsymbol{A}(\boldsymbol{r},t)=\nabla(\nabla\cdot\boldsymbol{A}(\boldsymbol{r},t))-\nabla^2\boldsymbol{A}(\boldsymbol{r},t) \tag{2.11}$$

and imposing the Lorenz gauge

$$\nabla\cdot\boldsymbol{A}(\boldsymbol{r},t)=-\mu_0\varepsilon_0\frac{\partial\Phi(\boldsymbol{r},t)}{\partial t}, \tag{2.12}$$

we obtain the Helmholtz equation for the magnetic vector potential

$$\nabla^2\boldsymbol{A}(\boldsymbol{r},t)-\mu_0\varepsilon_0\frac{\partial \boldsymbol{A}(\boldsymbol{r},t)}{\partial t^2}=-\mu_0\boldsymbol{J}(\boldsymbol{r},t). \tag{2.13}$$

By following the same procedure, it is possible to express the potential $\Phi(\boldsymbol{r},t)$ in terms of the charge density, which leads to the Helmholtz equation for the electric scalar potential

$$\nabla^2\Phi(\boldsymbol{r},t)-\mu_0\varepsilon_0\frac{\partial\Phi(\boldsymbol{r},t)}{\partial t^2}=-\frac{q(\boldsymbol{r},t)}{\varepsilon_0}. \tag{2.14}$$

In an homogeneous medium Eq. (2.13) has a closed-form solution for the magnetic vector potential $\boldsymbol{A}(\boldsymbol{r},t)$ caused by a current $\boldsymbol{J}(\boldsymbol{r},t)$ in the volume V'; it is

$$\boldsymbol{A}(\boldsymbol{r},t) \;=\; \frac{\mu_0}{4\pi}\int_{V'}\frac{\boldsymbol{J}(\boldsymbol{r}',t')}{|\boldsymbol{r}-\boldsymbol{r}'|}dV'. \tag{2.15}$$

Similarly, in an homogeneous, Eq. (2.14) has a closed-form solution for the electric scalar potential $\Phi(\boldsymbol{r},t)$ due to the charge distribution $q(\boldsymbol{r}',t)$, Assuming the charge resides on the exterior surface of conductors, the solution of (2.14) in a homogeneous medium is

$$\Phi(\boldsymbol{r},t)=\frac{1}{4\pi\varepsilon_0}\int_{S'}\frac{q(\boldsymbol{r}',t')}{|\boldsymbol{r}-\boldsymbol{r}'|}dS'. \tag{2.16}$$

In Eqs. (2.15) and (2.16), t' denotes the time at which the current and charge distributions, $\boldsymbol{J}$ and q, act as sources of $\boldsymbol{A}$ and Φ respectively; it differs from t

because of the finite speed of light in the homogeneous medium, $c = 1/\sqrt{\mu\varepsilon}$. This implies that the two times are related by

$$t' = t - \frac{|\boldsymbol{r} - \boldsymbol{r}'|}{c}. \tag{2.17}$$

In deriving relations (2.15) and (2.16) all the Maxwell's equations (2.1)–(2.4) were used along with the Lorenz gauge condition (2.12). At this stage, Eq. (2.9) for the electric field has not yet been utilized.
In a conductor, the following constitutive relation holds

$$\boldsymbol{E}(\boldsymbol{r}, t) = \frac{\boldsymbol{J}(\boldsymbol{r}, t)}{\sigma} \tag{2.18}$$

where σ represents the conductivity of the conductor. Substituting Eq. (2.18) into the electric field Eq. (2.9) and taking into account that an external electric field $\boldsymbol{E}_0(\boldsymbol{r}, t)$ can be impressed at point $\boldsymbol{r}$ at time t, the electric field integral equation (EFIE) is derived as

$$\boldsymbol{E}_0(\boldsymbol{r}, t) = \frac{\boldsymbol{J}(\boldsymbol{r}, t)}{\sigma} + \frac{\partial}{\partial t}\frac{\mu_0}{4\pi}\int_{V'} \frac{\boldsymbol{J}(\boldsymbol{r}', t')}{|\boldsymbol{r} - \boldsymbol{r}'|} dV' + \nabla\Phi(\boldsymbol{r}, t), \tag{2.19}$$

which holds at any point in a conductor. The electric scalar potential is related to the charge distribution by Eq. (2.16), here repeated for clarity

$$\Phi(\boldsymbol{r}, t) = \frac{1}{4\pi\varepsilon_0}\int_{S'} \frac{q(\boldsymbol{r}', t')}{|\boldsymbol{r} - \boldsymbol{r}'|} dS'. \tag{2.20}$$

To ensure charge conservation, the continuity equation must be satisfied

$$\nabla \cdot \boldsymbol{J}(\boldsymbol{r}, t) = -\frac{\partial q(\boldsymbol{r}, t)}{\partial t}. \tag{2.21}$$

Assuming that the charge is only located on the surface of conductors, Eq. (2.21) is simplified in the interior of the conductor, which becomes

$$\nabla \cdot \boldsymbol{J}(\boldsymbol{r}, t) = 0. \tag{2.22}$$

On the surface of the conductors, by applying the surface divergence, we obtain

$$\hat{\boldsymbol{n}} \cdot \boldsymbol{J}(\boldsymbol{r}, t) = \frac{\partial q(\boldsymbol{r}, t)}{\partial t}, \tag{2.23}$$

where $\hat{\boldsymbol{n}}$ represents the outward normal to the surface S'.

Finally, the set of equations to be solved is

$$\boldsymbol{E}_0(\boldsymbol{r},t) = \frac{\boldsymbol{J}(\boldsymbol{r},t)}{\sigma} + \frac{\partial}{\partial t}\frac{\mu_0}{4\pi}\int_{V'}\frac{\boldsymbol{J}(\boldsymbol{r}',t')}{|\boldsymbol{r}-\boldsymbol{r}'|}dV' + \nabla\Phi(\boldsymbol{r},t) \tag{2.24}$$

$$\Phi(\boldsymbol{r},t) = \frac{1}{4\pi\varepsilon_0}\int_{S'}\frac{q(\boldsymbol{r}',t')}{|\boldsymbol{r}-\boldsymbol{r}'|}dS' \qquad \boldsymbol{r}\in S' \tag{2.25}$$

$$\nabla\cdot\boldsymbol{J}(\boldsymbol{r},t) = 0 \qquad \boldsymbol{r}\in V' \tag{2.26}$$

$$\hat{\boldsymbol{n}}\cdot\boldsymbol{J}(\boldsymbol{r},t) = \frac{\partial q(\boldsymbol{r},t)}{\partial t} \qquad \boldsymbol{r}\in S'. \tag{2.27}$$

The unknowns of such a problem are the current density $\boldsymbol{J}(\boldsymbol{r},t)$ within the conductors, the charge density $q(\boldsymbol{r},t)$ on the surface of the conductors and the electric scalar potential distribution $\Phi(\boldsymbol{r},t)$ in the conductors which can be directly represented as a function of the charge density for $\boldsymbol{r}\in S'$.
Equations (2.24)–(2.27) can be reformulated in the Laplace domain as follow

$$\boldsymbol{E}_0(\boldsymbol{r},s) = \frac{\boldsymbol{J}(\boldsymbol{r},s)}{\sigma} + \frac{s\mu_0}{4\pi}\int_{V'}\frac{\boldsymbol{J}(\boldsymbol{r}',s)\,e^{-s\tau}}{|\boldsymbol{r}-\boldsymbol{r}'|}dV' + \nabla\Phi(\boldsymbol{r},s) \tag{2.28}$$

$$\Phi(\boldsymbol{r},s) = \frac{1}{4\pi\varepsilon_0}\int_{S'}\frac{q(\boldsymbol{r}',s)\,e^{-s\tau}}{|\boldsymbol{r}-\boldsymbol{r}'|}dS' \qquad \boldsymbol{r}\in S' \tag{2.29}$$

$$\nabla\cdot\boldsymbol{J}(\boldsymbol{r},s) = 0 \qquad \boldsymbol{r}\in V' \tag{2.30}$$

$$\hat{\boldsymbol{n}}\cdot\boldsymbol{J}(\boldsymbol{r},s) = sq(\boldsymbol{r},s) \qquad \boldsymbol{r}\in S' \tag{2.31}$$

where $\tau = |\boldsymbol{r}-\boldsymbol{r}'|/c$ and s represents the Laplace variable.
The most widely used technique for discretizing integral equations is referred to by Harrington as MoM [18], which has been seen with different implementations [51–55]. Typically, the solution is sought in the frequency domain by assuming $s = j\omega$. In the first step, the unknown quantities $\boldsymbol{J}(\boldsymbol{r},s)$ and $q(\boldsymbol{r},s)$ are approximated by a weighted sum of a finite set of basis functions $\boldsymbol{b}\in\mathcal{R}^{\ni}$ and $p\in\mathcal{R}$

$$\boldsymbol{J}(\boldsymbol{r},s) \cong \sum_{n=1}^{N_v}\boldsymbol{b}_n(\boldsymbol{r})\,I_n(s) \tag{2.32}$$

$$q(\boldsymbol{r},s) \cong \sum_{m=1}^{N_s}p_m(\boldsymbol{r})\,Q_m(s) \tag{2.33}$$

where $I_n(s)$ and $Q_m(s)$ are the weights of the basis function, which must be determined at each angular frequency s, N_v and N_s represent the number of volume and surface basis functions and the corresponding elementary volume and surface sub-regions, respectively. The expansion in Eqs. (2.32)–(2.33) are substituted into (2.28)–(2.29), evaluated for $s = j\omega$, yielding

$$\begin{aligned}\boldsymbol{E}_0(\boldsymbol{r},s) &= \sum_{n=1}^{N_v}\frac{\boldsymbol{b}_n(\boldsymbol{r})\,I_n(s)}{\sigma}+\frac{s\mu_0}{4\pi}\sum_{n=1}^{N_v}\int_{V_n}\boldsymbol{b}_n(\boldsymbol{r}_n)\,I_n(s)\,\frac{e^{-s\tau}}{|\boldsymbol{r}-\boldsymbol{r}_n|}dV_n+\\ &+ \nabla\Phi(\boldsymbol{r},s) \qquad (2.34)\\ \Phi(\boldsymbol{r},s) &= \frac{1}{4\pi\varepsilon_0}\sum_{m=1}^{N_s}\int_{S_m}p_m(\boldsymbol{r}_m)\,Q_m(s)\,\frac{e^{-s\tau}}{|\boldsymbol{r}-\boldsymbol{r}_m|}dS_m. \qquad (2.35)\end{aligned}$$

Next, the Galerkin's method of testing or weighting [54] is employed to generate a system of equations for the unknown weight functions $I_n(s), n=1,\ldots,N_v$ and $Q_m(s), m=1,\ldots,N_s$. This is achieved by enforcing the residuals of Eqs. (2.28)–(2.29) be orthogonal to a set of weighting functions. These weighting functions are chosen to coincide with the basis functions, which give us the following equations

$$\begin{aligned}&\left\langle -\boldsymbol{E}_0(\boldsymbol{r},s)+\frac{\sum_{n=1}^{N_v}\boldsymbol{b}_n(\boldsymbol{r})\,I_n(s)}{\sigma}+\right.\\ &+\left.\frac{s\mu_0}{4\pi}\left(\sum_{n=1}^{N_v}\int_{V_n}\boldsymbol{b}_n(\boldsymbol{r}_n)\,I_n(s)\,\frac{e^{-s\tau}}{|\boldsymbol{r}-\boldsymbol{r}_n|}\right)dV_n+\nabla\Phi(\boldsymbol{r},s),\boldsymbol{b}_i(\boldsymbol{r})\right\rangle=0 \qquad (2.36)\\ &\left\langle\Phi(\boldsymbol{r},s)-\frac{1}{4\pi\varepsilon_0}\sum_{m=1}^{N_s}\int_{S_m}p_m(\boldsymbol{r}_m)\,Q_m(s)\,\frac{e^{-s\tau}}{|\boldsymbol{r}-\boldsymbol{r}_m|}dS_m,p_j(\boldsymbol{r})\right\rangle=0, \qquad (2.37)\end{aligned}$$

where the inner products are defined as

$$\begin{aligned}\langle\boldsymbol{f}(\boldsymbol{r}),\boldsymbol{b}_i(\boldsymbol{r})\rangle &= \int_{V_i}\boldsymbol{f}(\boldsymbol{r})\cdot\boldsymbol{b}_i(\boldsymbol{r})\,dV_i \qquad \text{for } i=1,\ldots,N_v \qquad (2.38)\\ \langle g(\boldsymbol{r}),p_j(\boldsymbol{r})\rangle &= \int_{S_j}g(\boldsymbol{r})\cdot p_j(\boldsymbol{r})\,dS_j \qquad \text{for } j=1,\ldots,N_s. \qquad (2.39)\end{aligned}$$

2.1.1 Choice of the basis and weighting functions for the conductor surfaces

Various types of basis and weighting functions can be selected to form the equations (2.36) and (2.37). The most commonly used options include the piecewise constant, piecewise linear, RWG [52] set of basis and/or weighting functions. For the purpose of this analysis, we will assume the use of piecewise constant functions, which are particularly suitable for modeling Manhattan-type structures. Specifically, we assume that the conductors are orthogonal, and their surfaces are discretized into N_s elementary rectangular patches, which are electrically small compared to the wavelength of the highest frequency of interest. In this model, the unknown electric current and charge densities are assumed to be constant over each discrete patch.

Under this assumption, the basis functions that are used to expand the charge density are defined as

$$p_m(\boldsymbol{r}) = \begin{cases} \frac{1}{S_m} & \text{if } \boldsymbol{r} \in S_m \\ 0 & \text{otherwise.} \end{cases} \tag{2.40}$$

With this choice of the basis function, the corresponding weight Q_m represents the charge on patch m. Therefore, equation (2.35) can be rewritten as

$$\Phi(\boldsymbol{r}, s) = \sum_{m=1}^{N_s} \left[\frac{1}{4\pi\varepsilon_0} \frac{1}{S_m} \int_{S_m} \frac{e^{-s\tau}}{|\boldsymbol{r} - \boldsymbol{r}_m|} dS_m \right] Q_m(s). \tag{2.41}$$

This expression allows the evaluation of the potential at point $\boldsymbol{r}$ and angular frequency s, due to the charge on the N_s patches covering the conductors. This way, the equation models the electric field coupling in the background medium with permittivity ε_0.
Applying the Galerkin's method results in the evaluation of the average value of $\Phi(\boldsymbol{r}, s)$ over the surface of each patch

$$\begin{aligned} \Phi_\ell(\boldsymbol{r}_\ell, s) &= \frac{1}{S_\ell} \int_{S_\ell} \Phi(\boldsymbol{r}_\ell, s)\, dS_\ell = \\ &= \sum_{m=1}^{N_s} \left[\frac{1}{4\pi\varepsilon_0} \frac{1}{S_\ell} \frac{1}{S_m} \int_{S_\ell} \int_{S_m} \frac{e^{-s\tau}}{|\boldsymbol{r}_\ell - \boldsymbol{r}_m|} dS_m dS_\ell \right] Q_m(s) = \\ &= P_{\ell,m}(s)\, Q_m(s) \qquad \text{for } \ell = 1, \ldots, N_s, \end{aligned} \tag{2.42}$$

where coefficient of potential $P_{\ell,m}(s)$ is

$$P_{\ell,m}(s) = \frac{1}{4\pi\varepsilon_0} \frac{1}{S_\ell S_m} \int_{S_\ell} \int_{S_m} \frac{e^{-s\tau}}{|\boldsymbol{r}_\ell - \boldsymbol{r}_m|} dS_m dS_\ell. \tag{2.43}$$

Thus, the potential of the N_s patches can be expressed in terms of the charges located on those patches, at a given angular frequency s, by

$$\boldsymbol{\Phi}(s) = \mathbf{P}(s)\, \mathbf{Q}(s), \tag{2.44}$$

where the entries of the matrix $\mathbf{P}$ are referred to as coefficients of potential. These coefficients are generally frequency-dependent due to the full-wave type of analysis. The displacement currents in the surrounding medium are given by

$$\mathbf{I}_c(s) = s\mathbf{Q}(s) = s\mathbf{P}(s)^{-1} \boldsymbol{\Phi}(s). \tag{2.45}$$

2.1.2 Choice of the basis and weighting functions for the conductor volumes

Conductor volumes are discretized into N_v elementary orthogonal hexahedra (parallelepiped) which are electrically small compared to the wavelength corresponding

to the highest frequency of interest. We consider that ℓ_n represents the length and a_n represents the cross-section of volume V_n.
The basis functions used to represent the current density are defined as

$$\boldsymbol{b}_n(\boldsymbol{r}) = \begin{cases} \frac{\hat{\boldsymbol{u}}_n}{a_n} & \text{if } \boldsymbol{r} \in V_n \\ \mathbf{0} & \text{otherwise} \end{cases}, \tag{2.46}$$

where $\hat{\boldsymbol{u}}_n$ is the unit vector indicating the direction of the current in the volume V_n. With this choice of the basis function, the associated weight corresponds to the current flowing in the volume V_n along the direction $\hat{\boldsymbol{u}}_n$. Equation (2.34), after the Galerkin scheme is applied, can be rewritten as

$$\begin{aligned} E_0(\boldsymbol{r}_i, s)\,\ell_i &= \frac{\ell_i I_i(s)}{\sigma a_i} + \frac{s\mu_0}{4\pi}\sum_{n=1}^{N_v}\frac{1}{a_i}\frac{1}{a_n}\int_{V_i}\int_{V_n}\hat{\boldsymbol{u}}_i\cdot\hat{\boldsymbol{u}}_n I_n(s)\,\frac{e^{-s\tau}}{|\boldsymbol{r}_i-\boldsymbol{r}_n|}dV_n dV_i + \\ &+ \Phi_{2i}(s) - \Phi_{1i}(s) \qquad \text{for } i = 1,\ldots,N_v. \end{aligned} \tag{2.47}$$

In deriving the previous equation, we assumed that the external electric field $\boldsymbol{E}_0(\boldsymbol{r}, s)$ is uniform within the volume V_i.Additionally, the following approximation was made

$$\frac{1}{a_i}\int_{V_i}\hat{\boldsymbol{u}}_i\cdot\nabla\Phi(\boldsymbol{r}, s)\,dV_i = \frac{1}{a_i}\int_{a_i}\left(\int_{l_i}\hat{\boldsymbol{u}}_i\cdot\nabla\Phi(\boldsymbol{r}, s)\,dl_i\right)da_i = \Phi_{i_2}(s) - \Phi_{i_1}(s), \tag{2.48}$$

where $\Phi_{i_1}(s)$ and $\Phi_{i_2}(s)$ represent the potential at the extremes of the volume V_i along the $\hat{\boldsymbol{u}}_i$ direction.
Each term in equation (2.47) can be interpreted as a voltage drop across the volume V_i along the $\hat{\boldsymbol{u}}_i$ direction and, thus, it can be rewritten as

$$\Phi_{i_1}(s) - \Phi_{i_2}(s) = V_{0_i}(s) + R_i I_i + s\sum_{n=1}^{N_v} L_{p_{i,n}} I_n(s), \tag{2.49}$$

where

$$V_{0_i}(s) = -E_0(\boldsymbol{r}_i, s)\,\ell_i, \tag{2.50}$$

represents the voltage source due to external fields;

$$R_i = \frac{\ell_i}{\sigma a_i}, \tag{2.51}$$

is the resistance of the cell i where current flows along ℓ_i;

$$L_{p_{i,n}}(s) = \frac{\mu_0}{4\pi}\frac{1}{a_i a_n}\int_{V_i}\int_{V_n}\hat{\boldsymbol{u}}_i\cdot\hat{\boldsymbol{u}}_n\frac{e^{-s\tau}}{|\boldsymbol{r}_i-\boldsymbol{r}_n|}dV_n dV_i, \tag{2.52}$$

is the partial inductance [4] between volume cells i and n (as defined in [4];

$$\Phi_{i_1}(s) - \Phi_{i_2}(s), \tag{2.53}$$

is the potential difference between the nodes at the extremes of volume V_i, along the $\hat{\boldsymbol{u}}_i$ direction.
In a more compact matrix form equation (2.49) can be expressed as

$$-\mathbf{A}\boldsymbol{\Phi}(s) - \mathbf{R}\mathbf{I}(s) - s\mathbf{L}_p(s)\,\mathbf{I}(s) - \mathbf{V}_0(s) = \mathbf{0} \tag{2.54}$$

where vectors $\boldsymbol{\Phi}$ and $\mathbf{I}$ collect the potentials to infinity and the currents flowing through the longitudinal branches, respectively, and the matrix $\mathbf{A}$ is the connectivity matrix whose entries are

$$a_{n,k} = \begin{cases} +1 & \text{if current } I_n \text{ enters node } k \\ -1 & \text{if current } I_n \text{ leaves node } k \\ 0 & \text{otherwise.} \end{cases} \tag{2.55}$$

It is important to highlight that the discretization process described above has facilitated the generation of circuit topological elements such as branches, through which currents I_i, $i = 1, \ldots, N_v$, flow, and nodes, whose potential to infinity is Φ_ℓ, $\ell = 1, \ldots, N$ where $N > N_s$, since in the case of 3D structures, nodes may also exist within the interior of the conductors.
With this foundation, generating equivalent circuits becomes a straightforward process, as explained in the next section.

2.2 Development of equivalent circuit models

The procedure described above has allowed to write equations (2.24)–(2.27) in such a way that circuit unknowns are used, namely currents $I_i(s)$, $i = 1, \ldots, N_v$, potentials $\Phi_\ell(s)$, $\ell = 1, \ldots, N$ and charges $Q_m(s)$, $m = 1, \ldots, N_s$. The synthesis of the equivalent circuit is best described by applying the procedure to the very simple example of a zero-thickness strip of conductor depicted in Fig. 2.1. The discretization process has been accomplished, leading to three nodes, 1,2, and 3, and two branches connecting them. The corresponding unknowns are the currents I_1 and I_2 flowing through the branches, and the potential to infinity of the nodes, Φ_1,Φ_2 and Φ_3.

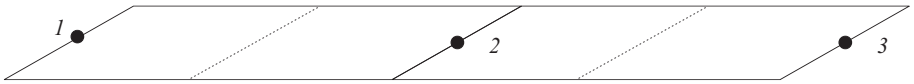


Figure 2.1: Single zero thickness conductor with three nodes.

2.2.1 Model for electric field coupling

A circuit model for the electric field coupling can be obtained stemming from equation (2.44), which, in the considered example, reads

$$\Phi_1 = P_{1,1}Q_1 + P_{1,2}Q_2 + P_{1,3}Q_3 \tag{2.56}$$
$$\Phi_2 = P_{2,1}Q_1 + P_{2,2}Q_2 + P_{2,3}Q_3 \tag{2.57}$$
$$\Phi_3 = P_{3,1}Q_1 + P_{3,2}Q_2 + P_{3,3}Q_3. \tag{2.58}$$

To carry on implementation in the time domain, it is helpful to distinguish between the self-effect and the mutual effects. The displacement currents are determined by evaluating the derivative of both the equations (2.56)–(2.58) with respect to time, yielding

$$I_{c_1} = sQ_1 = s\frac{1}{P_{1,1}}\Phi_1 - s\frac{P_{1,2}}{P_{1,1}}Q_2 - s\frac{P_{1,3}}{P_{1,1}}Q_3 \tag{2.59}$$
$$I_{c_2} = sQ_2 = s\frac{1}{P_{2,2}}\Phi_2 - s\frac{P_{2,1}}{P_{2,2}}Q_1 - s\frac{P_{2,3}}{P_{2,2}}Q_3 \tag{2.60}$$
$$I_{c_3} = sQ_3 = s\frac{1}{P_{3,3}}\Phi_3 - s\frac{P_{3,1}}{P_{3,3}}Q_1 - s\frac{P_{3,2}}{P_{3,3}}Q_2. \tag{2.61}$$

This separation allows for a more structured treatment of interactions within and between elements, simplifying the application of these equations to time-domain analysis. These derivatives allow us to identify the contribution of the self cell,

which can be modeled as a capacitor, from the mutual coupling, which is modeled in terms of current controlled current sources (CCCSs) $I_{d_1}, I_{d_2}, I_{d_3}$ as

$$I_{d_1} = s\frac{P_{1,2}}{P_{1,1}}Q_2 + s\frac{P_{1,3}}{P_{1,1}}Q_3 \tag{2.62}$$

$$I_{d_2} = s\frac{P_{2,1}}{P_{2,2}}Q_1 + s\frac{P_{2,3}}{P_{2,2}}Q_3 \tag{2.63}$$

$$I_{d_3} = s\frac{P_{3,1}}{P_{3,3}}Q_1 + s\frac{P_{3,2}}{P_{3,3}}Q_2. \tag{2.64}$$

In the most general case, the displacement current associated with the $k-$th CCCS can be expressed as

$$I_{d_k} = \sum_{\substack{m=1 \\ m\neq k}}^{N_s} \frac{P_{k,m}}{P_{k,k}} sQ_m = \sum_{\substack{m=1 \\ m\neq k}}^{N_s} \frac{P_{k,m}}{P_{k,k}} I_{c_m}. \tag{2.65}$$

where $P_{k,m}$ and $P_{k,k}$ are coefficients of potential, Q_m represents the charge on the m-th patch, and I_{c_m} denotes the displacement current through the m-th cell.
The relationship between the currents $\mathbf{I}_d$ (displacement currents in CCCSs) and $\mathbf{I}_c$ (displacement currents in the capacitors) is given by:

$$\mathbf{I}_d = \mathbf{K}\mathbf{I}_c \tag{2.66}$$

where

$$\mathbf{K} = \begin{bmatrix} 0 & \frac{P_{1,2}}{P_{1,1}} & \cdots & \frac{P_{1,N_s}}{P_{1,1}} \\ \frac{P_{2,1}}{P_{2,2}} & 0 & \cdots & \frac{P_{2,N_s}}{P_{2,2}} \\ \vdots & \vdots & \vdots & \vdots \\ \frac{P_{N_s,1}}{P_{N_s,N_s}} & \frac{P_{N_s,2}}{P_{N_s,N_s}} & \cdots & 0 \end{bmatrix}. \tag{2.67}$$

To account for the self-induced effects, we introduce a matrix $\mathbf{\Lambda}$, defined as

$$s\mathbf{\Lambda}\mathbf{\Phi} \tag{2.68}$$

where

$$\mathbf{\Lambda} = \begin{bmatrix} \frac{1}{P_{1,1}} & 0 & \cdots & 0 \\ 0 & \frac{1}{P_{2,2}} & \cdots & 0 \\ \vdots & \vdots & \vdots & \vdots \\ 0 & 0 & \cdots & \frac{1}{P_{N_s,N_s}} \end{bmatrix}. \tag{2.69}$$

Equations (2.59)-(2.61), in a more compact form, read

$$\mathbf{I}_d = s\mathbf{\Lambda}\mathbf{\Phi} - \mathbf{K}\mathbf{I}_c. \tag{2.70}$$

Such equations are well suited for a circuit interpretation, shown in Fig. 2.2.

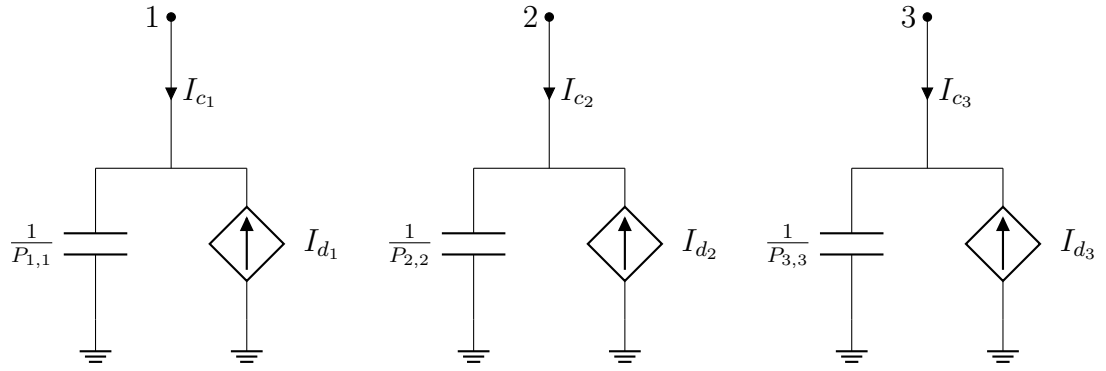


Figure 2.2: Equivalent circuit model for electric field coupling.

The following $\mathbf{P}^{-1}$ matrix factorization can also be expressed as

$$\mathbf{P}^{-1} = \mathbf{\Lambda}\mathbf{S}^{-1} = \left(\mathbf{S}\mathbf{\Lambda}^{-1}\right)^{-1} = \left(\mathbf{S}^{-1}\right)^{K}\mathbf{\Lambda} \tag{2.71}$$

where matrix $\mathbf{S}$ is given as

$$\mathbf{S} = \begin{bmatrix} 1 & \frac{P_{1,2}}{P_{2,2}} & \cdots & \frac{P_{1,N_s}}{P_{N_s,N_s}} \\ \frac{P_{2,1}}{P_{1,1}} & 1 & \cdots & \frac{P_{2,N_s}}{P_{N_s,N_s}} \\ \vdots & \vdots & \vdots & \vdots \\ \frac{P_{N_s,1}}{P_{1,1}} & \frac{P_{N_s,2}}{P_{2,2}} & \cdots & 1 \end{bmatrix}. \tag{2.72}$$

It is easy to verify that the following is satisfied

$$\mathbf{S}^T = \mathbf{K} + \mathbb{1}, \tag{2.73}$$

where $\mathbb{1}$ represents the all-ones matrix. It has to be pointed out that equations (2.56)–(2.58) provide a framework for modeling the electric field coupling in the background medium.

2.2.2 Model for magnetic field coupling

A circuit model for the magnetic field coupling can be derived starting from equation (2.47), which enforces the discrete form of the electric field equation (2.9) in the considered example, which can be defined as

$$\Phi_1 - \Phi_2 = \left(R_1 + sL_{p_{1,1}}I_1 + sL_{p_{1,2}}I_2 + V_{0_1}\right) \tag{2.74}$$

$$\Phi_2 - \Phi_3 = \left(R_2 + sL_{p_{2,2}}I_2 + sL_{p_{2,1}}I_1 + V_{0_2}\right). \tag{2.75}$$

It is suited for the circuit synthesis shown in Fig. 2.3

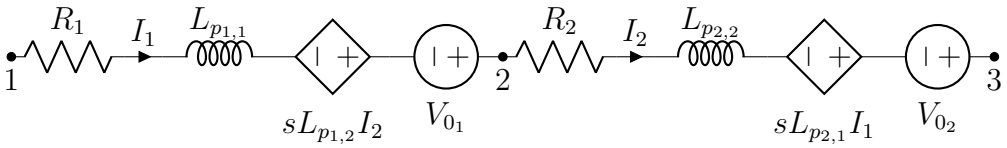


Figure 2.3: Equivalent circuit model for magnetic field coupling.

In the considered example, no interior node occurs, implying $N_s = N = 3$.

2.2.3 PEEC equivalent circuit

Once the equivalent circuits for the electric and magnetic field coupling have been generated, the next step is to connect equivalent circuits, as shown in Figs. 2.2 and 2.3. This can be done by simply connecting nodes 1,2 and 3 in Figs. 2.2 and 2.3, resulting in the combined equivalent circuit shown in Fig. 2.4.

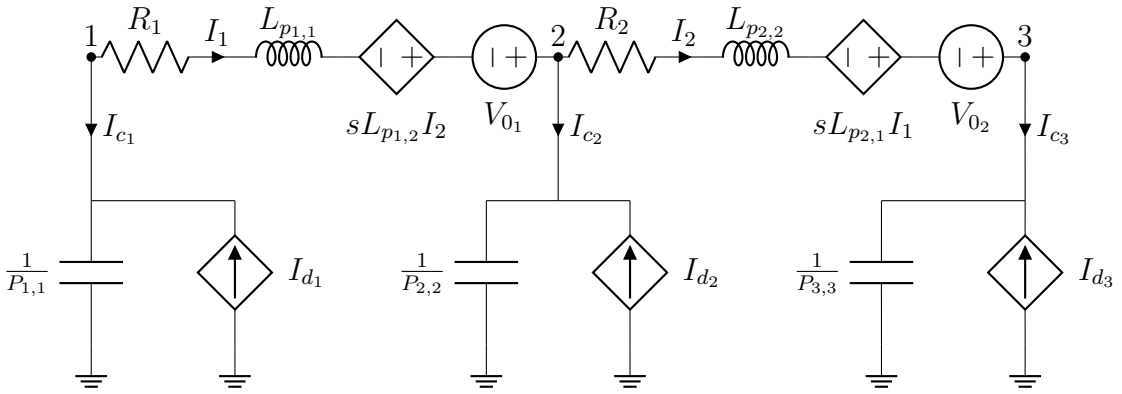


Figure 2.4: Equivalent circuit model for the simple example shown in Fig. 2.1.

2.2.4 Enforcement of Kirchhoff's current and voltage laws

Once the equivalent circuit is generated, Kirchhoff's current and voltage laws can be applied. The first set of equations can be derived by enforcing Kirchhoff's voltage law (KVL) on a mesh formed by the resistive-inductive branch connecting each couple of nodes and the capacitive branch connecting each node to infinity. It results in the set of equations (2.54), which is repeated here for the sake of clarity,

$$-\mathbf{A}\boldsymbol{\Phi}(s) - \mathbf{R}\mathbf{I}(s) - s\mathbf{L}_p(s)\,\mathbf{I}(s) - \mathbf{V}_0(s) = \mathbf{0}. \tag{2.76}$$

The PEEC method enforces the continuity equation in the form of Kirchhoff's current law (KCL). Taking into account that both $\mathbf{I}$ and $\mathbf{I}_c$ are present, and that external current sources $\mathbf{I}_s$ can be connected to each node, we write KCL as

$$\mathbf{I}_c(s) - \mathbf{A}^T\mathbf{I}(s) = \mathbf{I}_s(s) \tag{2.77}$$

where $\mathbf{A}^T$ represents the transpose matrix $\mathbf{A}$. Considering that the displacement currents $\mathbf{I}_c$ can be defined as a function of the potentials $\mathbf{\Phi}$ (2.45), it is possible to write

$$s\mathbf{P}(s)^{-1}\mathbf{\Phi}(s) + \mathbf{Y}_{le}\mathbf{\Phi}(s) - \mathbf{A}^T\mathbf{I}(s) = \mathbf{I}_s(s) \tag{2.78}$$

where $\mathbf{Y}_{le}$ represents the lumped elements admittance matrix eventually connecting nodes.
From the implementation perspective, it may be desirable to avoid the matrix inversion $\mathbf{P}(s)^{-1}$ due to its complexity ($O(n^3)$). Instead, The matrix $\mathbf{P}(s)$ can be used as a preconditioner, allowing the previous equation to be rewritten as

$$s\mathbf{\Phi}(s) + \mathbf{P}\mathbf{Y}_{le}\mathbf{\Phi}(s) - \mathbf{P}(s)\mathbf{A}^T\mathbf{I}(s) = \mathbf{P}(s)\mathbf{I}_s(s). \tag{2.79}$$

2.3 Computation of partial elements

As discussed in the previous section, constructing a PEEC model involves calculating partial elements, including partial inductances and coefficients of potential, which describe the magnetic and electric couplings, respectively, and resistances that account for power dissipation in conductive materials. This section focuses on calculating partial elements and presents existing closed-form formulas that enable fast and accurate computation of these elements.

2.3.1 Computation of partial inductances

The computation of partial inductances involves evaluating double-folded volume integrals such as the one in equation (2.80)

$$L_{p_{i,n}}(s) = \frac{\mu_0}{4\pi}\frac{1}{a_i a_n}\int_{V_i}\int_{V_n} \hat{\boldsymbol{u}}_i \cdot \hat{\boldsymbol{u}}_n \frac{e^{-s\tau}}{|\boldsymbol{r}_i - \boldsymbol{r}_n|} dV_n dV_i. \tag{2.80}$$

If the discretization satisfies the $\lambda_{min}/20$ rule ($\max(\text{dim}) < \lambda_{min}/20$) where $\max(\text{dim})$ represents the maximum dimension of cells and λ_{min} represents the minimum wavelength of interest, a center to center approximation can be assumed, and the partial inductance can be computed as

$$L_{p_{i,n}}(s) = \frac{\mu_0}{4\pi}\frac{e^{-s\tau_{in}^{cc}}}{a_i a_n}\int_{V_i}\int_{V_n} \hat{\boldsymbol{u}}_i \cdot \hat{\boldsymbol{u}}_n \frac{1}{|\boldsymbol{r}_i - \boldsymbol{r}_n|} dV_n dV_i = L_{p_{i,n}}^{st} e^{-s\tau_{in}^{cc}} \tag{2.81}$$

where τ_{in}^{cc} is the center to center distance between volume cells i and n.
Numerical integration techniques must be used for general geometries and when delay effects are non-negligible. In the quasi-static case and orthogonal geometry, analytical formulas are available. In the quasi-static case with orthogonal geometry, analytical formulas are available. The following section provides an overview of techniques for computing partial inductances. A more detailed description of closed-form formulas for evaluating partial inductances in standard configurations can be found in [4, 56–58].

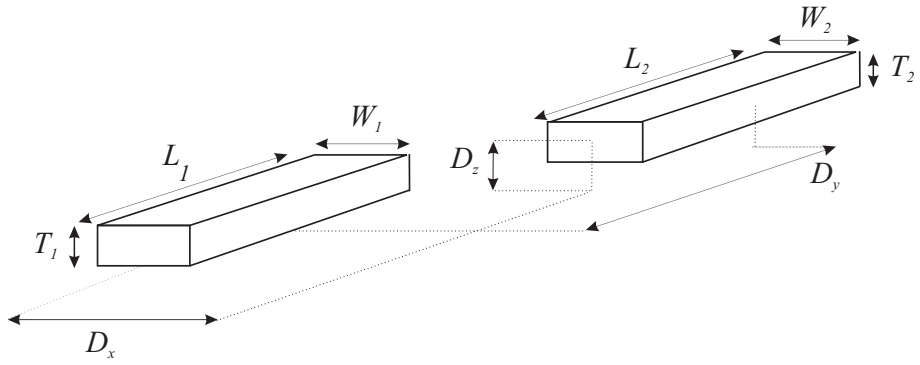


Figure 2.5: Geometry and notation for the computation of self and mutual partial inductances.

Self Partial Inductance of a 3D rectangular cell

$$\begin{aligned}
\frac{L_{p_{i,i}}}{L} &= \frac{2\mu_0}{\pi}\{\frac{\omega^2}{24u}\left[\log\left(\frac{1+A_2}{\omega}\right)-A_5\right]+\frac{1}{24u\omega}\left[\log\left(\omega+A_2\right)-A_6\right]+ \\
&+ \frac{\omega^2}{60u}(A_4-A_3)+\frac{\omega^2}{24}[\log\left(\frac{u+A_3}{\omega}\right)-A_7]+\frac{\omega^2}{60u}(\omega-A_2)+\frac{1}{20u}(A_2-A_4)+ \\
&+ \frac{u}{4}A_5-\frac{u^2}{6\omega}\arctan\left(\frac{\omega}{uA_4}\right)+\frac{u}{4\omega}A_6-\frac{\omega}{6}\arctan\left(\frac{u}{\omega A_4}\right)+\frac{A_7}{4}+ \\
&- \frac{1}{6\omega}\arctan\left(\frac{u\omega}{A_4}\right)+\frac{1}{24\omega^2}\left[\log(u+A_1)-A_7\right]+\frac{u}{20\omega^2}(A_1-A_4)+ \\
&+ \frac{1}{60\omega^2 u}(1-A_2)+\frac{1}{60u\omega^2}(A_4-A_1)+\frac{u}{20}(A_3-A_4)+ \\
&+ \frac{u^3}{24\omega^2}\left[\log\left(\frac{1+A_1}{u}\right)-A_5\right]+\frac{u^3}{24\omega}\left[\log\left(\frac{\omega+A_3}{u}\right)-A_6\right]+ \\
&+ \frac{u^3}{60\omega^2}\left[(A_4-A_1)+(u-A_3)\right]\},
\end{aligned} \tag{2.82}$$

where $u = L/W$, $\omega = T/W$ and the following notation is adopted

$$\begin{aligned}
A_1 &= \sqrt{1+u^2}, & A_2 &= \sqrt{1+\omega^2} \\
A_3 &= \sqrt{\omega^2+u^2}, & A_4 &= \sqrt{1+\omega^2+u^2} \\
A_5 &= \log\left(\tfrac{1+A_4}{A_3}\right), & A_6 &= \log\left(\tfrac{\omega+A_4}{A_1}\right) \\
A_7 &= \log\left(\tfrac{u+A_4}{A_2}\right).
\end{aligned} \tag{2.83}$$

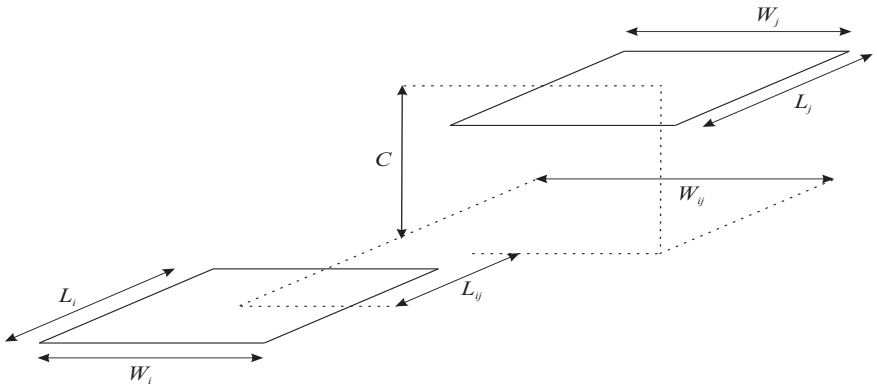


Figure 2.6: Co-planar zero-thickness conductor geometry for the evaluation of the mutual partial inductance and coefficient of potential.

Mutual partial inductance of 2D rectangular cells

$$
\begin{aligned}
L_{p_{i,j}} &= \frac{\mu_0}{4\pi}\frac{1}{W_i W_j}\sum_{k=1}^{4}\sum_{m=1}^{4}(-1)^{m+k}\left[\frac{b_m^2-C^2}{2}a_k\,\log\left(a_k+\rho\right)+\right. \qquad (2.84)\\
&+ \left.\frac{a_k^2-C^2}{2}b_m\,\log\left(b_m+\rho\right)-\frac{1}{6}(b_m^2-2C^2+a_k^2)\rho-b_m\,C\,a_k\arctan\left(\frac{a_k\,b_m}{\rho\,C}\right)\right],
\end{aligned}
$$

where

$$
\begin{array}{ll}
\rho=\sqrt{a_k^2+b_m^2+C^2}, & \\
a_1=W_{ij}-\frac{W_i}{2}-\frac{W_j}{2}, & a_2=W_{ij}+\frac{W_i}{2}-\frac{W_j}{2}\\
a_3=W_{ij}+\frac{W_i}{2}+\frac{W_j}{2}, & a_4=W_{ij}-\frac{W_i}{2}+\frac{W_j}{2}\\
b_1=L_{ij}-\frac{L_i}{2}-\frac{L_j}{2}, & b_2=L_{ij}+\frac{L_i}{2}-\frac{L_j}{2}\\
b_3=L_{ij}+\frac{L_i}{2}+\frac{L_j}{2}, & b_4=L_{ij}-\frac{L_i}{2}+\frac{L_j}{2}
\end{array}
\qquad (2.85)
$$

and C is the distance between the two planes containing surface cell i and j.

Mutual and self partial inductance of 1D rectangular cells In the case of structures where two dimensions are much smaller than the third, volumetric cells can be approximated as filaments. In this assumption, a closed formula for mutual partial inductance between parallel filaments with equal length is derived.
The mutual inductance $L_{p_{i,j}}$ between two parallel filaments of length L and separated by a distance D can be calculated using the following formula

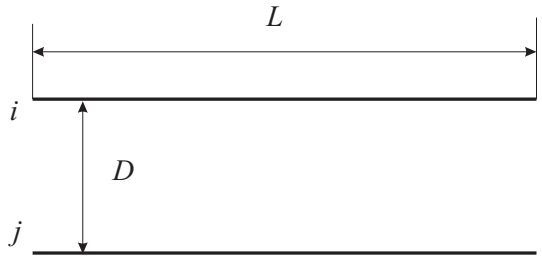


Figure 2.7: Two parallel filaments.

$$L_{p_{i,j}} = \frac{\mu_0}{2\pi} L \left[\log \left(\frac{L}{D} + \sqrt{\left(\frac{L}{D}\right)^2 + 1} \right) + \frac{D}{L} - \sqrt{\left(\frac{D}{L}\right)^2 + 1} \right], \tag{2.86}$$

where

- L is the length of the filaments,
- D is the distance between the filaments,
- μ_0 is the permeability of free space.

This formula provides an analytical expression for the mutual partial inductance in the case of two parallel filaments, which is often used for simplifications in modeling certain types of structures where the geometry is elongated in one dimension compared to the other two. A good approximation of the self-partial inductance can be obtained by substituting d with the radius r of conductors

$$L_{p_{i,i}} = \frac{\mu_0}{2\pi} L \left[\log \left(\frac{L}{r} + \sqrt{\left(\frac{L}{r}\right)^2 + 1} \right) + \frac{r}{L} - \sqrt{\left(\frac{r}{L}\right)^2 + 1} \right]. \tag{2.87}$$

2.3.2 Computation of coefficients of potential

The evaluation of coefficients of potential involves evaluating double surface integrals, as expressed in equation (2.43):

$$P_{\ell,m}(s) = \frac{1}{4\pi\varepsilon_0} \frac{1}{S_\ell S_m} \int_{S_\ell} \int_{S_m} \frac{e^{-s\tau}}{|\boldsymbol{r}_\ell - \boldsymbol{r}_m|} dS_m dS_\ell. \tag{2.88}$$

If the discretization satisfy the $\lambda_{min}/20$ rule, a center to center approximation can be applied. In this case, the coefficient of potential can be calculated as

$$P_{\ell,m}(s) = \frac{1}{4\pi\varepsilon_0} \frac{e^{-s\tau^{cc}_{\ell m}}}{S_\ell S_m} \int_{S_\ell} \int_{S_m} \frac{1}{|\boldsymbol{r}_\ell - \boldsymbol{r}_m|} dS_m dS_\ell = P^{st}_{\ell,m} e^{-s\tau^{cc}_{\ell m}} \tag{2.89}$$

where $\tau_{\ell m}^{cc}$ trepresents he center to center distance between surface cells ℓ and m. No closed-form expressions exist for computing such integrals in arbitrary geometries, necessitating numerical integration techniques. However, closed-form solutions can be utilized for the quasi-static case and specific geometries. To ensure both high accuracy and efficient computation of the partial coefficients of potential, basic geometries, referred to as building blocks, have been defined. A formulation for evaluating the partial coefficient of potential is given for each basic geometry. The most important basic geometry is the *rectangular surface cell* depicted in Fig. 2.8. The interested reader may refer to [5, 59] for a complete overview of coefficients of potential computation.

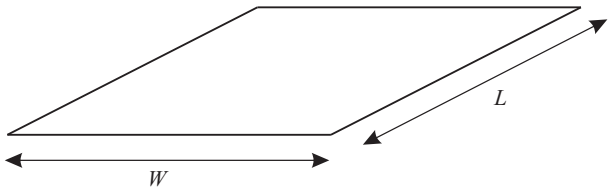


Figure 2.8: Rectangular conductor geometry for the evaluation of the self coefficient of potential.

Partial Self Coefficient of Potential The formula for evaluating the partial self-coefficient of potential for a general rectangular conductor, given in equation (2.90), is a modified version from [4], which was initially used for evaluating the partial self-inductance of thin conductors. The expression is:

$$\begin{aligned} P_{i,i} &= \frac{1}{4\pi\varepsilon_0 L}\,\frac{2}{3}\Big\{\,3\,\log\Big[u+(u^2+1)^{\frac{1}{2}}\Big]+u^2+\frac{1}{u}+ \\ &+ \;3\,u\,\log\left[\frac{1}{u}+(\frac{1}{u^2}+1)^{\frac{1}{2}}\right]-\left[u^{\frac{4}{3}}+(\frac{1}{u})^{\frac{2}{3}}\right]^{\frac{3}{2}}\Big\} \end{aligned} \tag{2.90}$$

where $u = L/W$ using the definitions from Fig. 2.8. This formula involves logarithmic and power terms that account for the conductor's geometry, offering an accurate analytical method for self-coefficient computation in rectangular conductors. Modifications were made to the original inductance formula to evaluate electrostatic coupling.

Partial Mutual Coefficients of Potential Efficient calculation methods for partial mutual coefficients of potential are more critical than those for partial self-coefficients of potential. This is due to the mutual capacitive or electric field coupling

between all surface cells in a discretized model. To achieve both computational efficiency and accuracy in partial element calculations, two fundamental geometries have been defined for mutual coefficients of potential. The most significant one involves the mutual coupling between two rectangular surface cells, as shown in Fig. 2.6.

The formula for calculating the partial mutual coefficient of potential for the general conductor configuration shown in Fig. 2.6 is defined by a modified version of the (2.84) originally developed for partial mutual inductances in zero-thickness conductors. Using the notations defined in Fig. 2.6, the equation is expressed as

$$\begin{aligned} P_{i,j} &= \frac{1}{4\pi\varepsilon_0}\frac{1}{W_i L_i W_j L_j}\sum_{k=1}^{4}\sum_{m=1}^{4}(-1)^{m+k}\left[\frac{b_m^2-C^2}{2}a_k\,\log(a_k+\rho)+\right. \\ &+ \left.\frac{a_k^2-C^2}{2}b_m\,\log(b_m+\rho)-\frac{1}{6}(b_m^2-2C^2+a_k^2)\rho-b_m\,C\,a_k\arctan\left(\frac{a_k\,b_m}{\rho\,C}\right)\right] \end{aligned} \tag{2.91}$$

where

$$\begin{array}{ll} \rho=\sqrt{a_k^2+b_m^2+C^2}, & \\ a_1=W_{ij}-\frac{W_i}{2}-\frac{W_j}{2}, & a_2=W_{ij}+\frac{W_i}{2}-\frac{W_j}{2} \\ a_3=W_{ij}+\frac{W_i}{2}+\frac{W_j}{2}, & a_4=W_{ij}-\frac{W_i}{2}+\frac{W_j}{2} \\ b_1=L_{ij}-\frac{L_i}{2}-\frac{L_j}{2}, & b_2=L_{ij}+\frac{L_i}{2}-\frac{L_j}{2} \\ b_3=L_{ij}+\frac{L_i}{2}+\frac{L_j}{2}, & b_4=L_{ij}-\frac{L_i}{2}+\frac{L_j}{2} \end{array} \tag{2.92}$$

Here C represents the distance between the two planes containing surface cell i and j.

The second fundamental geometry examined involves two cells placed perpendicularly to each other, as shown in Fig. 2.9.

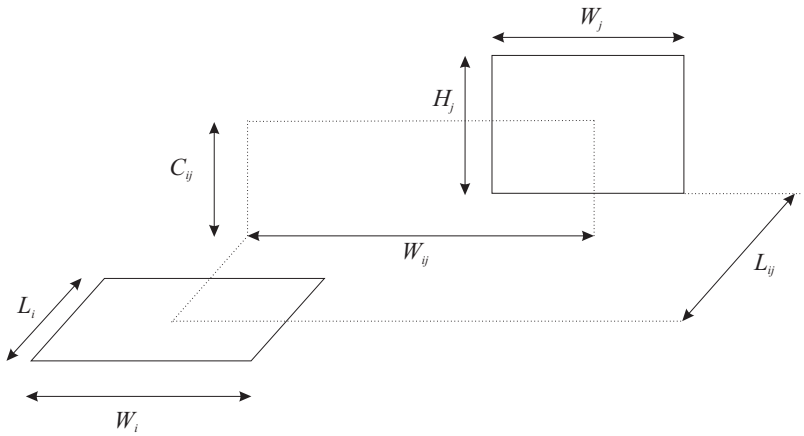


Figure 2.9: Orthogonal Rectangular surface conductor geometry for the evaluation of the partial mutual coefficient of potential.

The evaluation of the perpendicular surface cell partial mutual coefficient of potential in Eq. (16) in [5] is given by.

$$\begin{aligned} P_{i,j} &= \frac{1}{4\pi\varepsilon_0}\frac{1}{W_i L_i W_j H_j}\sum_{k=1}^{4}\sum_{m=1}^{2}\sum_{\ell=1}^{2}(-1)^{\ell+m+k+1}\cdot\left[\left(\frac{a_k^2}{2}-\frac{c_\ell^2}{6}\right)c_\ell\log\left(b_m+\rho\right)+\right. \\ &+ \cdots+\left(\frac{a_k^2}{2}-\frac{b_m^2}{6}\right)b_m\log\left(c_\ell+\rho\right)+a_k b_m c_\ell\log\left(a_k+\rho\right)+ \\ &- \left.\frac{b_m c_\ell}{3}\rho-\frac{a_k^3}{6}\arctan\left(\frac{b_m c_\ell}{a_k\rho}\right)-\frac{b_m^2 a_k}{6}\arctan\left(\frac{a_k c_\ell}{b_m\rho}\right)-\frac{a_k c_\ell^2}{2}\arctan\left(\frac{a_k b_m}{c_\ell\rho}\right)\right], \end{aligned} \tag{2.93}$$

where

$$\begin{aligned} &\rho=\sqrt{a_k^2+b_m^2+C^2}, \\ &a_1=W_{ij}-\tfrac{W_i}{2}-\tfrac{W_j}{2}, \quad a_2=W_{ij}+\tfrac{W_i}{2}-\tfrac{W_j}{2} \\ &a_3=W_{ij}+\tfrac{W_i}{2}+\tfrac{W_j}{2}, \quad a_4=W_{ij}-\tfrac{W_i}{2}+\tfrac{W_j}{2} \\ &b_1=L_{ij}+\tfrac{L_i}{2}, \quad b_2=L_{ij}-\tfrac{L_i}{2} \\ &c_1=C_{ij}+\tfrac{H_j}{2}, \quad c_2=C_{ij}-\tfrac{H_j}{2}. \end{aligned} \tag{2.94}$$

Computation of resistances

In a PEEC model, partial resistances are computed based on the discretization of the volume cells, using the resistance formula provided in (2.51)

$$R_\gamma=\frac{\ell_\gamma}{a_\gamma\sigma_\gamma} \tag{2.95}$$

where ℓ_γ represents the length of the volume cell along the direction of the current, a_γ is the cross-section normal to the current direction, and σ_γ denotes the conductivity of the volume cell material.
In PEEC models, resistance accounts for conductor losses. A more comprehensive approach for calculating partial elements in non-orthogonal geometries can be found in [25, 60].

2.4 Dielectrics modeling

The basic concept of modeling dielectrics is to demonstrate the displacement current resulting from bound charges in materials with a relative permittivity $\varepsilon_r > 1$ separately from the conducting currents due to the free charges. Maxwell's equation for the displacement current is expressed as

$$\nabla \cdot \boldsymbol{E} = \frac{q^F + q^B}{\varepsilon_0}, \tag{2.96}$$

where q^F represents the free charge, and q^B represents the bound charge due to the dielectric regions. Thus, the global charge is $q^T = q^F + q^B$.
The dielectric volumes can be incorporated into the analysis by considering the polarization current density associated with their presence. This can be achieved by adding and subtracting the displacement current in the background medium $\varepsilon_0\varepsilon_r \frac{\partial \boldsymbol{E}(\boldsymbol{r},t)}{\partial t}$ in the Maxwell equation for $\boldsymbol{H}$ [7]. This method ensures that the impact of the dielectric polarization is incorporated into the model.

$$\begin{aligned} \nabla \times \boldsymbol{H}(\boldsymbol{r},t) &= \boldsymbol{J}^C(\boldsymbol{r},t) + \varepsilon_0\varepsilon_r \frac{\partial \boldsymbol{E}(\boldsymbol{r},t)}{\partial t} = \\ &= \boldsymbol{J}^C(\boldsymbol{r},t) + \varepsilon_0(\varepsilon_r - 1)\frac{\partial \boldsymbol{E}(\boldsymbol{r},t)}{\partial t} + \varepsilon_0 \frac{\partial \boldsymbol{E}(\boldsymbol{r},t)}{\partial t}. \end{aligned} \tag{2.97}$$

Thus, the total current in equation (2.97) accounts for both the electric current arising from the conductivity of the medium and the polarization current induced by the presence of dielectrics. This comprehensive formulation ensures that the contributions of both free and bound charges are considered in the electromagnetic analysis.

$$\boldsymbol{J}^T(\boldsymbol{r},t) = \boldsymbol{J}^C(\boldsymbol{r},t) + \varepsilon_0(\varepsilon_r - 1)\frac{\partial \boldsymbol{E}(\boldsymbol{r},t)}{\partial t} = \boldsymbol{J}^C(\boldsymbol{r},t) + \boldsymbol{J}^D(\boldsymbol{r},t). \tag{2.98}$$

Thus, the magnetic vector potential at point $\boldsymbol{r}$, as expressed in (2.15) is given by

$$\boldsymbol{A}(\boldsymbol{r},t) = \frac{\mu_0}{4\pi}\int_{V'} \frac{\boldsymbol{J}^T(\boldsymbol{r}',t')}{|\boldsymbol{r}-\boldsymbol{r}'|} dV'. \tag{2.99}$$

For a point located in a conductor (2.24) becomes

$$\begin{aligned} \boldsymbol{E}_0(\boldsymbol{r},t) &= \frac{\boldsymbol{J}^C(\boldsymbol{r},t)}{\sigma} + \frac{\partial}{\partial t}\frac{\mu_0}{4\pi}\int_{V'} \frac{\boldsymbol{J}^C(\boldsymbol{r}',t')}{|\boldsymbol{r}-\boldsymbol{r}'|} dV' + \\ &+ \varepsilon_0(\varepsilon_r - 1)\frac{\mu_0}{4\pi}\int_{V'} \frac{1}{|\boldsymbol{r}-\boldsymbol{r}'|}\frac{\partial^2 \boldsymbol{E}(\boldsymbol{r}',t')}{\partial t^2} dV' + \nabla\Phi(\boldsymbol{r},t). \end{aligned} \tag{2.100}$$

At a point $\boldsymbol{r}$ within a dielectric region with relative permittivity ε_r (2.24) becomes

$$\begin{aligned} \boldsymbol{E}_0(\boldsymbol{r},t) &= \boldsymbol{E}(\boldsymbol{r},t) + \frac{\partial}{\partial t}\frac{\mu_0}{4\pi}\int_{V'}\frac{\boldsymbol{J}^T(\boldsymbol{r}',t')}{|\boldsymbol{r}-\boldsymbol{r}'|}dV' + \\ &+ \varepsilon_0(\varepsilon_r-1)\frac{\mu_0}{4\pi}\int_{V'}\frac{1}{|\boldsymbol{r}-\boldsymbol{r}'|}\frac{\partial^2\boldsymbol{E}(\boldsymbol{r}',t')}{\partial t^2}dV' + \nabla\Phi(\boldsymbol{r},t) \end{aligned} \tag{2.101}$$

Here, $\Phi(\boldsymbol{r},t)$ is expressed as

$$\Phi(\boldsymbol{r},t) = \frac{1}{4\pi\varepsilon_0}\int_{S'}\frac{q^T(\boldsymbol{r}',t')}{|\boldsymbol{r}-\boldsymbol{r}'|}dS' \qquad \boldsymbol{r}\in S'. \tag{2.102}$$

Hence, it can be seen that the electric field at a point $\boldsymbol{r}$, $\boldsymbol{E}(\boldsymbol{r})$, is determined by the first time derivative of the current density distribution $\boldsymbol{J}^T(\boldsymbol{r},t)$, the gradient of the electric scalar potential $\nabla\Phi(\boldsymbol{r},t)$ and also by the second derivative of the electric field itself $\partial^2\boldsymbol{E}(\boldsymbol{r}',t')/\partial t^2$.
As mentioned earlier, the charges, q^F, q^B, and q^T, reside on the surface of the conductors and dielectrics while the currents flow through volumes. Therefore, the continuity equation cannot be applied in the same manner as in moment type solutions [18] is expressed as

$$\nabla\cdot\boldsymbol{J}^T + \frac{\partial q^T}{\partial t} = 0 \tag{2.103}$$

is not directly enforced. Instead, it is implemented as Kirchhoff's current law at each node. Thus, within each conductor and each homogeneous dielectric block, it reads

$$\nabla\cdot\boldsymbol{J}^C(\boldsymbol{r}) = 0 \tag{2.104}$$

$$\nabla\cdot\boldsymbol{J}^D(\boldsymbol{r}) = 0. \tag{2.105}$$

Additionally, the current normal to the surface on each conductor and dielectric causes accumulation of surface charge, leading to

$$\hat{\boldsymbol{n}}\cdot\boldsymbol{J}^C(\boldsymbol{r}) = sq^F(\boldsymbol{r}) \tag{2.106}$$

$$\hat{\boldsymbol{n}}\cdot\boldsymbol{J}^D(\boldsymbol{r}) = sq^B(\boldsymbol{r}). \tag{2.107}$$

On the surface between touching conductor and dielectric blocks, equation (2.106) becomes

$$\hat{\boldsymbol{n}}\cdot\boldsymbol{J}^T(\boldsymbol{r}) = sq^T(\boldsymbol{r}). \tag{2.108}$$

Let's refer to Fig. 2.10, the conductors and dielectrics can be divided into blocks where the conduction or displacement currents are assumed to be uniform. Additionally, the surfaces of conductors and dielectrics are discretized into panels that represent free and bound charges.

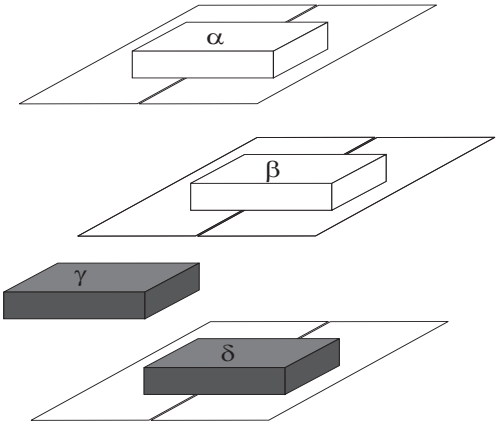


Figure 2.10: Cell structure for finite conductors and dielectrics.

Cells α and β represent conductors with free charge q^F located on their surfaces. Dielectric cell γ is an internal cell with no outside surface, meaning there is no charge on its surface. Finally, dielectric cell δ is on the surface of the dielectric body and presents bound charge q^B on its surface. In the following, it will be referred to the total charge q^T to be general.
The vector quantities can be represented in terms of the Cartesian coordinates. In this case, the vector quantities are $\boldsymbol{J} = J_x\hat{\boldsymbol{x}} + J_y\hat{\boldsymbol{y}} + J_z\hat{\boldsymbol{z}}$ and $\boldsymbol{E} = E_x\hat{\boldsymbol{x}} + E_y\hat{\boldsymbol{y}} + E_z\hat{\boldsymbol{z}}$. The three integral equations are structurally identical except for the space directions x, y, and z. Therefore, it is possible to consider cells in the y-direction only, without loss of generality Equations (2.100), (2.101) represent a system of three coupled integral equations. The vectors $\boldsymbol{r}$ and $\boldsymbol{r}'$ denote where the electric field is evaluated and where the source, current, or charge is located, respectively.
Two distinct cases need to be considered based on the position of the field point $\boldsymbol{r}$. In the first case, the field point $\boldsymbol{r}$ is located within a conductor, while in the second case, the field point is within a dielectric block.
Assume that $\boldsymbol{r}$ is located within a conductor cell and no external field $\boldsymbol{E}_0$ exists, applying equation (2.100) applied to the conductor cell α is

$$\begin{aligned}
&\frac{J_y^C(\boldsymbol{r},t)}{\sigma_\alpha} + \frac{\partial}{\partial t}\frac{\mu_0}{4\pi}\int_{V_{\alpha'}} \frac{J^C(\boldsymbol{r}',t')}{|\boldsymbol{r}-\boldsymbol{r}'|}dV'_\alpha + \frac{\partial}{\partial t}\frac{\mu_0}{4\pi}\int_{V'_\beta} \frac{J^C(\boldsymbol{r}',t')}{|\boldsymbol{r}-\boldsymbol{r}'|}dV'_\beta + \\
+ \;& \varepsilon_0(\varepsilon_\gamma - 1)\frac{\mu_0}{4\pi}\int_{V'_\gamma} \frac{1}{|\boldsymbol{r}-\boldsymbol{r}'|}\frac{\partial^2 E_y(\boldsymbol{r}',t')}{\partial t^2}dV'_\gamma + \qquad (2.109)\\
+ \;& \varepsilon_0(\varepsilon_\delta - 1)\frac{\mu_0}{4\pi}\int_{V'_\delta} \frac{1}{|\boldsymbol{r}-\boldsymbol{r}'|}\frac{\partial^2 E_y(\boldsymbol{r}',t')}{\partial t^2}dV'_\delta + \frac{1}{4\pi\epsilon_0}\int_{S'_\alpha} \frac{\partial}{\partial y}\frac{1}{|\boldsymbol{r}-\boldsymbol{r}'|}q^T(\boldsymbol{r}',t')dS'_\alpha + \\
+ \;& \frac{1}{4\pi\epsilon_0}\int_{S'_\beta} \frac{\partial}{\partial y}\frac{1}{|\boldsymbol{r}-\boldsymbol{r}'|}q^T(\boldsymbol{r}',t')dS'_\beta + \frac{1}{4\pi\epsilon_0}\int_{S'_\delta} \frac{\partial}{\partial y}\frac{1}{|\boldsymbol{r}-\boldsymbol{r}'|}q^T(\boldsymbol{r}',t')dS'_\delta = 0
\end{aligned}$$

where σ_α is the electrical conductivity of cell α.
We apply the Galerkin solution by interpreting each single term of (2.109) in terms of circuit representation. For simplicity, we assume that the density current J_y^C is uniform across the cross-section of cell α and the quasi-static assumption holds e.g. $t = t'$, thus the delay due to the speed of light in the background medium is neglected.
The first term of (2.109) represents the voltage drop across the resistance of the cell α

$$\frac{1}{a_\alpha}\int_{V_\alpha}\frac{J_y^C(\boldsymbol{r}_\alpha,t)}{\sigma_\alpha}dV_\alpha = \frac{1}{a_\alpha}\int_{a_\alpha}\int_{l_\alpha}\frac{J_y^C(\boldsymbol{r}_\alpha,t)}{\sigma_\alpha}da_\alpha dl_\alpha = \rho_\alpha\frac{l_\alpha}{a_\alpha}(a_\alpha J_y^C) = R_\alpha I_y^C \quad (2.110)$$

where a_α is the cross-sectional area, l_α is the length of the conductor cell α, ρ_α is the resistivity of the cell, and I_y^C is the current through the conductor cell.
The second term represents the voltage drop across the self-inductance of the cell α

$$\left(\frac{\mu_0}{4\pi a_\alpha a_\alpha}\int_{V'_\alpha}\int_{V_\alpha}\frac{1}{|\boldsymbol{r}_\alpha-\boldsymbol{r}'_\alpha|}dV'_\alpha dV_\alpha\right)\frac{d}{dt}(a_\alpha J_y^C) = L_{p_{\alpha,\alpha}}\frac{dI_y^C}{dt}. \quad (2.111)$$

This expression allows us to identify the self-partial inductance of cell α as

$$L_{p_{\alpha,\alpha}} = \frac{\mu_0}{4\pi a_\alpha a_\alpha}\int_{V'_\alpha}\int_{V_\alpha}\frac{1}{|\boldsymbol{r}_\alpha-\boldsymbol{r}'_\alpha|}dV'_\alpha dV_\alpha. \quad (2.112)$$

Using the same approach, we can identify the mutual partial inductance between the conductor cells α and β in the third term of the equation of (2.109)

$$L_{p_{\alpha,\beta}} = \frac{\mu_0}{4\pi a_\alpha a_\beta}\int_{V_\alpha}\int_{V_\beta}\frac{1}{|\boldsymbol{r}_\alpha-\boldsymbol{r}_\beta|}dV_\alpha dV_\beta. \quad (2.113)$$

The fourth and fifth terms represent the coupling between the conductor cell α and dielectric cells γ and δ.Despite the differing material properties, these terms still exhibit an inductive coupling, as shown below

$$\varepsilon_0(\varepsilon_\gamma-1)\frac{\mu_0}{4\pi a_\alpha}\int_{V_\alpha}\int_{V'_\gamma}\frac{1}{|\boldsymbol{r}_\alpha-\boldsymbol{r}'_\gamma|}\frac{\partial^2 E_y(\boldsymbol{r}'_\gamma,t_d)}{\partial t^2}dV'_\gamma dV_\alpha = \quad (2.114)$$

$$= \left(\frac{\mu_0}{4\pi a_\alpha}\int_{V_\alpha}\int_{V_\gamma}\frac{1}{|\boldsymbol{r}_\alpha-\boldsymbol{r}'_\gamma|}dV'_\gamma dV_\alpha\right)\frac{d}{dt}\left(a_\gamma\varepsilon_0(\varepsilon_\gamma-1)\frac{dE_y}{dt}\right) = L_{p_{\alpha,\gamma}}\frac{dI_y^P}{dt}$$

where the polarization I_y^P current appears. The mutual partial inductance between cells α and γ can be determined using the same formula (2.113). The same consideration applies to the fifth term.
The last three terms of (2.109) represent the electric field produced in cell α due to the charge located on the surface of cells α, β and δ. It is important to note that the

coefficients of potential describing such couplings are the same as in the free space. Let's consider point $\boldsymbol{r}$ is located in the dielectric cell γ; equation (2.101) becomes

$$\begin{aligned} E_y(\boldsymbol{r},t) &+ \frac{\mu_0}{4\pi}\int_{V'_\alpha} K(\boldsymbol{r},\boldsymbol{r}')\frac{\partial J_y^C(\boldsymbol{r}',t_d)}{\partial t}dV'_\alpha + \frac{\mu_0}{4\pi}\int_{V'_\beta} K(\boldsymbol{r},\boldsymbol{r}')\frac{\partial J_y^C(\boldsymbol{r}',t_d)}{\partial t}dV'_\beta \\ &+ \varepsilon_0(\varepsilon_\gamma-1)\frac{\mu_0}{4\pi}\int_{V'_\gamma} K(\boldsymbol{r},\boldsymbol{r}')\frac{\partial^2 E_y(\boldsymbol{r}',t_d)}{\partial t^2}dV'_\gamma + \\ &+ \varepsilon_0(\varepsilon_\delta-1)\frac{\mu_0}{4\pi}\int_{V'_\delta} K(\boldsymbol{r},\boldsymbol{r}')\frac{\partial^2 E_y(\boldsymbol{r}',t_d)}{\partial t^2}dV'_\delta + \\ &+ \frac{1}{4\pi\varepsilon_0}\int_{S'_\alpha}\frac{\partial K(\boldsymbol{r},\boldsymbol{r}')}{\partial y}q^T(\boldsymbol{r}',t)dS'_\alpha + \frac{1}{4\pi\varepsilon_0}\int_{S'_\beta}\frac{\partial K(\boldsymbol{r},\boldsymbol{r}')}{\partial y}q^T(\boldsymbol{r}',t)dS'_\beta + \\ &+ \frac{1}{4\pi\varepsilon_0}\int_{S'_\delta}\frac{\partial K(\boldsymbol{r},\boldsymbol{r}')}{\partial y}q^T(\boldsymbol{r}',t)dS'_\delta = 0. \end{aligned} \tag{2.115}$$

The Galerkin's testing procedure is applied, which leads to the derivation of the corresponding equivalent circuits. By integrating the first term in (2.115), the voltage drop across a dielectric volume cell is defined as

$$\frac{1}{a_\gamma}\int_{a_\gamma}\int_{\ell_\gamma} E_y(\boldsymbol{r},t)d\ell_\gamma da_\gamma = \frac{1}{a_\gamma}a_\gamma\ell_\gamma E_y(t) = v_{c_\gamma}. \tag{2.116}$$

A polarization current flows through the dielectric cell γ

$$\begin{aligned} I_y^{POL} &= J_y^{POL}a_\gamma = \left(\varepsilon_0(\varepsilon_\gamma-1)\frac{dE_\gamma}{dt}\right)a_\gamma = \left(\varepsilon_0(\varepsilon_\gamma-1)\frac{dE_\gamma}{dt}\right)\frac{\ell_\gamma}{\ell_\gamma}a_\gamma = \\ &= \frac{d}{dt}\left[\left(\frac{\varepsilon_0(\varepsilon_\gamma-1)a_\gamma}{\ell_\gamma}\right)(\ell_\gamma E_y)\right] = C_e\frac{dv_{c_\gamma}}{dt}, \end{aligned} \tag{2.117}$$

where capacitance C_e is named *excess capacitance* and defined as

$$C_e = \frac{\varepsilon_0(\varepsilon_\gamma-1)a_\gamma}{\ell_\gamma}. \tag{2.118}$$

The second and third terms in (2.115) represent inductive coupling. The fourth term helps in defining the partial self-inductance of the dielectric cell γ

$$\varepsilon_0(\varepsilon_\gamma-1)\frac{\mu_0}{4\pi}\frac{1}{a_\gamma}\int_{V_\gamma}\int_{V'_\gamma} K(\boldsymbol{r}_\gamma,\boldsymbol{r}'_\gamma)\frac{\partial^2 E_y(\boldsymbol{r}_\gamma,t_d)}{\partial t^2}dV'_\gamma dV_\gamma = \tag{2.119}$$

$$= \left(\frac{\mu_0}{4\pi}\frac{1}{a_\gamma a_\gamma}\int_{V_\gamma}\int_{V'_\gamma} K(\boldsymbol{r}_\gamma,\boldsymbol{r}'_\gamma)dV'_\gamma dV_\gamma\right)\frac{d}{dt}\left(a_\gamma\varepsilon_0(\varepsilon_\gamma-1)\frac{dE_y}{dt}\right) = L_{p_{\gamma,\gamma}}\frac{dI_y^{POL}}{dt}.$$

The final term allows to compute the mutual partial inductance between dielectric cells γ and δ

$$L_{p_{\gamma,\delta}} = \frac{\mu_0}{4\pi a_\gamma a_\delta} \int_{V_\gamma} \int_{V'_\delta} \frac{1}{\boldsymbol{r}_\gamma - \boldsymbol{r}'_\delta} dV'_\delta dV_\gamma. \tag{2.120}$$

Again, the last three terms are similar to those computed in free space. To summarize, ideal (lossless) dielectrics are represented by volume cells characterized by excess capacitance, which is in series with the equivalent circuit for inductive coupling, described in terms of self and partial inductances, all computed in free space. Figure 2.11 shows the PEEC equivalent circuit of a dielectric bar, assuming $N_v = 2$, $N_s = N = 3$.

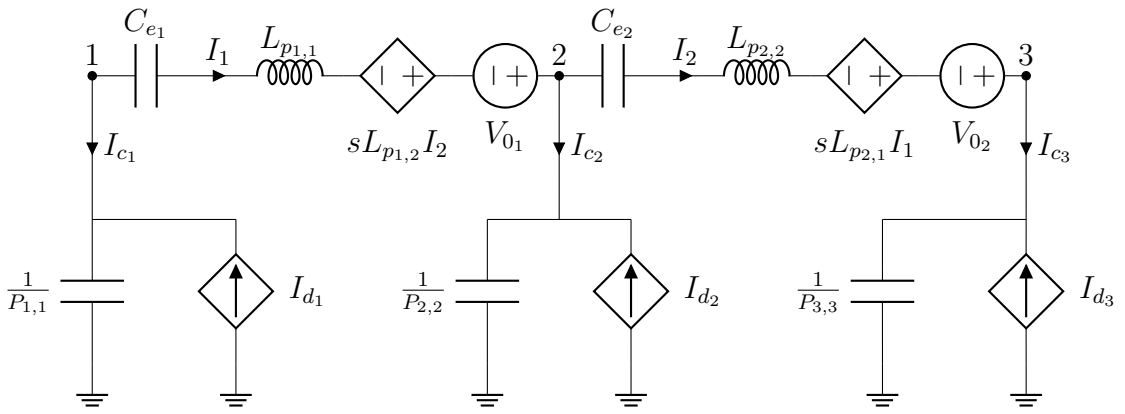


Figure 2.11: PEEC equivalent circuit for dielectrics.

More recently, PEEC models of dispersive and lossy dielectrics have been proposed [61–63].

2.4.1 External incident electric fields

When analyzing EMC problems, the excitation can be represented by currents, voltage-sources and external electric fields. The inclusion of incident fields in the PEEC method is explained in [64], where a source equivalence, denoted as V_0, is derived from the left-hand side in (2.24). The equivalent voltage source, V_0, is then connected in series with each inductive volume cell equivalent circuit. For a specific volume m, the voltage source is calculated using the following expression

$$V_{0_m}(t) = \frac{1}{a_m} \int_{a_m} \int_{\ell_m} \boldsymbol{E}^i(\boldsymbol{r}, t) da\ dl \tag{2.121}$$

where

$$\boldsymbol{E}^i(\boldsymbol{r}, t) = E^i_x(\boldsymbol{r}, t)\hat{x} + E^i_y(\boldsymbol{r}, t)\hat{y} + E^i_z(\boldsymbol{r}, t)\hat{z}. \tag{2.122}$$

2.5 Analysis of PEEC models

The analysis of PEEC models can be carried out in both the frequency and time domain using the same circuit.

2.5.1 Frequency domain solver

A PEEC solver in the frequency domain can be derived by combining equations (2.76) and (2.77), with the frequency dependence omitted for simplicity

$$\begin{bmatrix} -\mathbf{A} & -(\mathbf{R}+s\mathbf{L}_p) \\ s\mathbf{P}^{-1} & -\mathbf{A}^T \end{bmatrix} \cdot \begin{bmatrix} \mathbf{\Phi} \\ \mathbf{I} \end{bmatrix} = \begin{bmatrix} \mathbf{V}_0 \\ \mathbf{I}_s \end{bmatrix}. \tag{2.123}$$

Solution of dense linear systems

An efficient and accurate solution to the linear system (2.123) is crucial for the performance of the PEEC solver. The LU decomposition is a commonly used method for solving linear systems [65]. However, despite its elegance, this approach is not practical for solving large, dense linear systems due to its complexity of $O(n^3)$, where n is the number of unknowns. A more efficient alternative is to use Krylov subspace iterative methods [65]. Several variations of these methods are available, with GMRES [66] being one of the most popular. GMRES has a complexity of $O(n^2)$ as it requires matrix-vector products and converges quickly with the use of an efficient *preconditioner*. Additionally, matrix-vector products can be further accelerated using fast multipole techniques [67–70] or precorrected-FFT methods [71], which can reduce the overall complexity to $O(n\log(n))$.

2.5.2 Time domain solver

Developing a time-domain PEEC solver must account for the delays in the coupling terms. In this context, it is assumed that the partial inductances and potential coefficients are evaluated as static values, using a center-to-center approximation as given in (2.81) and (2.89).
The coupling inductance $L_{p_{m,n}}$ between the partial inductances $L_{p_{m,m}}$ and $L_{p_{n,n}}$ introduces the neutral delay term which is related to the physical distance between the inductive cells m and n as shown

$$t'_{m,n} = t - \frac{|\boldsymbol{r}_m - \boldsymbol{r}_n|}{c} = t - \tau. \tag{2.124}$$

Thus, the coupled inductive voltage is given by

$$v_{m,n} = L_{p_{m,n}} \frac{di_n(t'_{m,n})}{dt}. \tag{2.125}$$

Similarly, the capacitive coupling with delays must be incorporated. The general form of the capacitive term is $\mathbf{\Phi}(s) = \mathbf{PQ}(s)$ where $\mathbf{P}(s)$ represents the coefficient of potential matrix. The corresponding time-domain implementation can be derived from (2.70)

$$i_{c_k}(t) = \frac{1}{P_{k,k}} \frac{\partial \Phi_k}{\partial t} - \sum_{\substack{m=1 \\ m \neq k}}^{N_s} \frac{P_{k,m}}{P_{k,k}} i_{c_m}(t'_{k,m}), \tag{2.126}$$

where i_{c_k} represents the total capacitive current for cell k. It is possible to assign multiple delays for each cell pair, which results in potentially multiple distances $R_{k,m}$ between points on two cells k and m.
The above formulation for a linear PEEC circuit consisting of PEEC models and utilizing the Modified Nodal Analysis (MNA) technique [72], can be written as the following NDDE

$$\mathbf{C_0}\,\dot{\mathbf{x}} + \mathbf{G_0}\mathbf{x} = \sum_i \mathbf{G_i}\,\mathbf{x}(t-\tau_i) + \sum_i \boldsymbol{C_i}\,\dot{\mathbf{x}}(t-\tau_i) + \sum_i \mathbf{B}\mathbf{u_i}(t-\tau_i). \tag{2.127}$$

In this equation, $\mathbf{C_0}$ and $\mathbf{G_0}$ represent the time-dependent and the static portion of the non-delayed part, respectively, while $\mathbf{C_i}$ and $\mathbf{G_i}$ correspond to the elements that include a delay τ_i.The matrix $\mathbf{B}$ represents the input matrix, and $\mathbf{u}$ represents the inputs or forcing voltages and currents. The size of this combined electromagnetic and circuit (EM/Ckt) problem can become extremely large, with $\mathbf{L}_p$ and $\mathbf{P}$ coupling coefficients matrices being dense and very large.
As seen in Eq. (2.127), the solution of the left-hand side is significantly very sparse since it only consists of the non-retarded part or the slightly retarded part of the matrix, depending on the time step h. In a time-domain solver, the couplings must be evaluated by retrieving past values, which are delayed by the appropriate τ for the time domain from stored waveforms. As a result, the couplings are pre-determined and incorporated directly into the known right-hand side of the system rather than the MNA circuit coefficient matrix. Therefore, the basic solution complexity is $O(n^2)$, where n is the system size.
One of the key challenges that currently limits the general applicability of the time-domain approach is ensuring the long-term stability of the solution. Over the past three decades, numerous researchers have contributed to improving the stability of these methods [73]. In [74], the general stability issue with full-wave time-domain integral equation solution is discussed. Since then, significant advancements have been made on the stability issue. For instance, the effect of the delay points on the conductors was analyzed in [75], and the introduction of more delay points or cell subdivisions of the conductors on the stability issue was considered for PEEC models in [76]. A strategy for refining delay assignments was proposed in [77], and more recently, the stability of quasi-static PEEC models has been studied in [78].

The selection of the numerical integration method plays a very important role in various aspects of the solution. Early approaches to solving time-domain electromagnetic integral equation solvers relied on explicit methods [74]. However, it became evident that explicit methods, such as forward Euler, could only produce stable solutions in special cases and for extremely small time steps. As a result, several researchers began to adopt implicit methods for the time domain PEEC methods, which are particularly effective for this type of problem, *e.g.*, [79,80]. A key factor in choosing an appropriate method is the behavior of the stability function $R(z)$ where $z = \lambda h$, λ represents the eigenvalue, and h denotes the time step [81]. The stability functions must decay with $z \to \infty$. This is evident from the last section since various mechanisms in the model ensure that the amplitude decays above f_M, preventing strong feedback without affecting the solution behavior below f_M. Three methods that are well suited for this purpose are the backward Euler method, the θ method for $\theta > 0.5$, and the Lobatto III-C method. In fact, the Lobatto III-C method decays as $1/(z^2)$, which is very desirable. However, as shown below, the size of the system matrix is a factor 2 larger than for the θ or the BE methods. The commonly used trapezoidal rule has been shown to be one of the least effective methods for these systems [80]. The stability function of the BE method decays asymptotically as $1/(z)$, which is also desirable. The NDDE equations can be solved by adapting Runge-Kutta methods for ordinary differential equations (ODEs), as demonstrated in [82].
Finally, it is important to note that the solution of (2.127) can be sped up using techniques, i.e., fast multipole method and multi-function techniques [33, 70, 83].

Chapter 3

The concept of model order reduction

Model order reduction (MOR) is a powerful mathematical tool used to reduce the complexity of large-scale dynamical systems while preserving their essential characteristics. In the context of computational electromagnetics, MOR is particularly useful for accelerating simulations of PEEC models, which can become computationally expensive due to the large number of unknowns.
This chapter provides a comprehensive overview of MOR techniques. It begins with an introduction to proper orthogonal decomposition (POD), a widely used method for identifying dominant modes in complex systems. The mathematical formulation of POD is presented, along with its implementation in frequency-domain and time-domain analyses.
Next, the chapter explores moment-matching techniques, including Padé and Padé-type approximations, which are widely employed in circuit simulation. Krylov subspace methods, such as the Iterative Rational Krylov Algorithm (IRKA), are also discussed as effective techniques for generating reduced-order models while maintaining accuracy in key frequency ranges.
A significant portion of the chapter is dedicated to the Loewner framework, a data-driven approach to MOR that constructs reduced models from frequency-domain measurements. The advantages of using the Loewner framework, particularly for systems where explicit mathematical formulations are unavailable, are highlighted.
The chapter concludes with a discussion on the trade-offs involved in different MOR techniques, including computational complexity, accuracy, and applicability to different types of complex dynamical systems. These insights set the stage for the application of MOR to delayed PEEC models in subsequent chapters.

3.1 Formulation of reduced order model

With the emergence of computers and processors, modeling and simulation have shown outstanding development in various fields. This approach is essential in areas such as computational fluid dynamics (CFD), electromagnetic systems, control systems, numerical analysis, the semiconductor industry, computational physics, and more. Today, it is widely recognized as part of computational science and engineering.

Numerous physical, chemical, and other processes are now routinely simulated using computers, with specific platforms facilitating these efforts. These platforms enable designers to develop new products more quickly and with greater reliability. However, there are complex dynamical models that consider various parameters to be a realistic replica of the physical system. Such models are very complex and require high computational resources to be simulated. The MOR concept has been defined to overcome such issues.

MOR, in general, is a set of techniques used to reduce the computational complexity of large mathematical models. At the start, MOR was applied to the field of control systems. But later on, it expanded into CFD, mechanical systems, electromagnetic models, etc. The idea of MOR is to build a smaller model, also known as the reduced order model (ROM), which exhibits all the required features of the full order model (FOM) with a small error. In comparison to FOM, ROM simulates faster due to less complexity. Generally, MOR gives you a trade-off between the size and accuracy of the model.

MOR is widely divided into three categories. The first is based on the singular value decomposition (SVD) scheme [84]. Proper orthogonal decomposition [85] and balanced truncation [86] use the SVD method to build ROM in which the model is redesigned into such realizations where one can keep the larger singular values which carry more information and neglect the smaller singular values which carry very little information. The second set of methods is based on moment matching. In such techniques, moments are matched either explicitly, such as Pade approximation [87] or Pade type approximation [88] or implicitly, such as Krylov subspace, which iteratively approximates the system's behavior and matches moments implicitly. The implicit moment matching techniques are very helpful in such cases where the evaluation of moments directly is not computationally efficient.

The third category is represented by data-driven MOR approaches, which are particularly useful in scenarios where obtaining a complete mathematical model is challenging or infeasible. Dynamic mode decomposition [89] and Loewner framework [90] serve the purpose.

Apartheid from this, MOR techniques can be categorized as linear and non-linear MOR, structure-preserving MOR, parametric and non-parametric MOR, etc. We explain some of the basic techniques in this chapter. Let us consider a simple linear

time-invariant (LTI) system, which can be represented in the set of equations as given in Eq.(3.1) and Eq. (3.2)

$$\mathbf{C}\,(t)\,\frac{d\mathbf{x}(t)}{dt} = -\mathbf{G}\,(t)\,\mathbf{x}(t) + \mathbf{B}\mathbf{u}(t), \tag{3.1}$$

$$\mathbf{y}(t) = \mathbf{L}^T\mathbf{x}(t), \tag{3.2}$$

where

- $\mathbf{x}(t)$: State vector of the system, representing the internal state at time t $\in \mathbb{R}^{n\times 1}$.
- $\frac{d\mathbf{x}(t)}{dt}$: Derivative of the state vector with respect to time $\in \mathbb{R}^{n\times 1}$.
- $\mathbf{C}(t)$: Control matrix that scales the derivative of the state vector $\in \mathbb{R}^{n\times n}$.
- $\mathbf{G}(t)$: System matrix that defines the dynamics of the system $\in \mathbb{R}^{n\times n}$.
- $\mathbf{B}$: Input matrix that maps the control input $\mathbf{u}(t)$ into the state space $\in \mathbb{R}^{n\times m}$, where m is the number of inputs.
- $\mathbf{u}(t)$: Input vector (control inputs) to the system at time $t \in \mathbb{R}^{m\times 1}$.
- $\mathbf{y}(t)$: Output vector of the system, representing the measurable outputs at time $t \in \mathbb{R}^{p\times 1}$, where p is the number of outputs.
- $\mathbf{L}^T$: Output matrix that relates the state vector to the output $\in \mathbb{R}^{p\times n}$.

Next, we approximate the unknown state variables by projecting the model in (3.1) into an appropriately lower dimension. For this purpose, we choose the set of basis vectors represented by $\mathbf{V}$ of size $\mathbb{R}^{n\times r}$ where $r << n$. We define $\mathbf{x}(t) \approx \mathbf{V}\mathbf{x}_r(t)$ [91]. Applying Galerkin's projection [92] gives us

$$\mathbf{V}^T(\mathbf{C}(t)\mathbf{V}\dot{\mathbf{x}}_r(t) + \mathbf{G}(t)\mathbf{V}\mathbf{x}_r(t) - \mathbf{B}\mathbf{u}(t)) = 0, \tag{3.3}$$

which gives us ROM represented as

$$\mathbf{C}_r\,(t)\,\frac{d\mathbf{x}_r(t)}{dt} = -\mathbf{G}_r\,(t)\,\mathbf{x}_r(t) + \mathbf{B}_r\mathbf{u}(t) \tag{3.4}$$

$$\mathbf{y}_r(t) = \mathbf{L}_r^T\mathbf{x}_r(t), \tag{3.5}$$

with the reduced matrices defined as

$$\mathbf{C}_r = \mathbf{V}^T\mathbf{C}\mathbf{V},\ \mathbf{G}_r = \mathbf{V}^T\mathbf{G}\mathbf{V},\ \mathbf{B}_r = \mathbf{V}^T\mathbf{B}, \mathbf{L}_r = \mathbf{V}^T\mathbf{L}, \tag{3.6}$$

where

- $\mathbf{x}_r(t)$: Reduced state vector representing the approximation of the full state in a lower-dimensional subspace, $\mathbf{x}_r(t) \in \mathbb{R}^{r\times 1}$.
- $\frac{d\mathbf{x}_r(t)}{dt}$: Derivative of the reduced state vector with respect to time, $\frac{d\mathbf{x}_r(t)}{dt} \in \mathbb{R}^{r\times 1}$.
- $\mathbf{C}_r(t)$: Reduced control matrix, $\mathbf{C}_r(t) \in \mathbb{R}^{r\times r}$.
- $\mathbf{G}_r(t)$: Reduced system matrix, $\mathbf{G}_r(t) \in \mathbb{R}^{r\times r}$.
- $\mathbf{B}_r$: Reduced input matrix, $\mathbf{B}_r \in \mathbb{R}^{r\times m}$.
- $\mathbf{u}(t)$: Input vector remains the same as in the full model, $\mathbf{u}(t) \in \mathbb{R}^{m\times 1}$.
- $\mathbf{y}_r(t)$: Reduced output vector representing the approximation of the output, $\mathbf{y}_r(t) \in \mathbb{R}^{p\times 1}$.
- $\mathbf{L}_r^T$: Reduced output matrix, $\mathbf{L}_r \in \mathbb{R}^{r\times p}$.

In some settings, we use the $\mathbf{W}$ as well, which is referred to as the left projection matrix, while $\mathbf{V}$ is the basis for the reduced subspace. The reduced matrices are then constructed as

$$\mathbf{C}_r = \mathbf{W}^T\mathbf{C}\mathbf{V},\ \mathbf{G}_r = \mathbf{W}^T\mathbf{G}\mathbf{V},\ \mathbf{B}_r = \mathbf{W}^T\mathbf{B}, \mathbf{L}_r = \mathbf{V}^T\mathbf{L}. \tag{3.7}$$

We can represent our system in the frequency domain through the transfer function. For this, let's take the Laplace transform of the Eq. (3.1) and Eq. (3.2), we have

$$s\mathbf{C}\mathbf{X}(s) = -\mathbf{G}\mathbf{X}(s) + \mathbf{B}\mathbf{U}(s), \tag{3.8}$$

$$\mathbf{Y}(s) = \mathbf{L}^T\mathbf{X}(s). \tag{3.9}$$

Re-arranging the terms in Eq. (3.8), it becomes

$$\mathbf{X}(s) = (s\mathbf{C} + \mathbf{G})^{-1}\mathbf{B}\mathbf{U}(s). \tag{3.10}$$

Substituting $\mathbf{X}(s)$ into the output equation, we get the transfer function in the Eq. (3.11)

$$\mathbf{H}(s) = \mathbf{L}^T(s\mathbf{C} + \mathbf{G})^{-1}\mathbf{B}, \tag{3.11}$$

where $s = j\omega$. Similarly, the transfer function of ROM is represented as

$$\mathbf{H}_r(s) = \mathbf{L}_r^T(s\mathbf{C}_r + \mathbf{G}_r)^{-1}\mathbf{B}_r. \tag{3.12}$$

3.2 Proper orthogonal decomposition

Lumley first introduced proper orthogonal decomposition (POD) in 1967 [93]. He used POD to decompose the random vector field of turbulent fluid motion into a set of deterministic functions. But POD was tried earlier by some other researchers independently [94–96]. POD works efficiently for linear systems and has been extended to non-linear systems [97]. POD basis vectors are used to project the FOM into lower dimensions, which makes it easy to solve and simulate.
Let us consider a system in (3.1) and (3.2); we find snapshots of the output $\mathbf{y}(t)$ at the q different instants of the input $\mathbf{u}(t)$ i.e. $\mathbf{u}_1, \mathbf{u}_2, \ldots, \mathbf{u}_q$. These snapshots are represented as $\mathbf{Y} = [\mathbf{y}_1, \mathbf{y}_2, \ldots \mathbf{y}_q]$. Next, we apply the SVD to the snapshots matrix $\mathbf{Y}$

$$[\mathbf{V}, \mathbf{\Sigma}, \mathbf{U}] = SVD(\mathbf{Y}), \tag{3.13}$$

where $\mathbf{V} \in \mathbb{R}^{n\times n}$ represents the left singular vectors, $\mathbf{\Sigma} \in \mathbb{R}^{n\times n}$ represents the singular values over the diagonal i.e. $diag(\sigma_1, \sigma_2, \ldots, \sigma_n)$ and $\mathbf{U} \in \mathbb{R}^{n\times n}$ represents the right singular vectors. These singular values are in descending order such as $\sigma_1 \geq \sigma_2 \geq \sigma_3, \ldots, \sigma_{n_s}, \ldots, \geq 0$. We select r number of singular values to construct the basis matrices. Next, we check how much model information can be lost while considering the number of singular values neglected.

$$\min_{\mathbf{V}\in\mathbb{R}^{n\times r}} \left\|\mathbf{Y} - \mathbf{V}\mathbf{V}^T\mathbf{Y}\right\|_F^2 = \min_{\mathbf{V}\in\mathbb{R}^{n\times r}} \sum_{i=1}^{n_s} \left\|\mathbf{y}_i - \mathbf{V}\mathbf{V}^T\mathbf{y}_i\right\|_2^2 = \sum_{i=r+1}^{n_s} \sigma_i^2. \tag{3.14}$$

From (3.14), the sum of the squares of the singular values associated with the left singular vectors excluded from the POD basis gives us the square of the error in the snapshot representation. Therefore, the singular values are used to determine the POD basis's size. A common strategy is to select the number of r singular values in such a way that

$$\frac{\sum_{i=1}^{r}}{\sum_{i=1}^{n_s}} \geq tol, \tag{3.15}$$

where tol represents the tolerance, which can be defined depending on the nature of the model.
The basis vector constructed using POD does not have the idea of the original model, therefore POD can be applied to linear, non linear and parameterized models. In [98], we see that the optimality of the POD basis is limited to minimizing the reconstruction error of the snapshots and does not take care of the error in the solution of the POD-based reduced model. The accuracy of ROM built using POD also depends on the optimal choice of the snapshots [99]. An optimal choice of snapshots can be interpreted using the reachability Gramians of the balanced

truncation technique. [100]. Sometimes, the snapshots are chosen within the known range where accurate ROM is generated. There are also adaptive schemes that can be used for the selection of the optimal snapshots [101–107].

3.3 Moment matching based MOR

Moment matching-based MOR techniques approximate high-dimensional linear dynamical systems with a lower-dimensional ROM, which maps the input-output behavior of the original system. In fields such as circuit simulation, control systems, and mechanical engineering, moment matching provides accurate ROM, which can be used for control, simulation, and design purposes.
The basic idea of moment matching is to match specific "moments" of the transfer function of the original system with those of the ROM. The "moments" are coefficients in the Taylor series expansion of the transfer function around a specific frequency point. The i^{th} moment of the transfer function also represents the i^{th} derivative of the transfer function. Therefore, if we match more moments, we will get a better approximated ROM [108, 109]. We re-write the transfer function $\mathbf{H}(s)$ in Eq. (3.11) as an expansion of Taylor series around an expansion point s_0 provided that $s_0\mathbf{C} + \mathbf{G}$ is a nonsingular matrix, then we have:

$$\begin{aligned} H(s) &= \mathbf{L}^T \left[(s - s_0 + s_0)\mathbf{C} + \mathbf{G}\right]^{-1} \mathbf{B} \\ &= \mathbf{L}^T \left[(s - s_0)\mathbf{C} + (s_0\mathbf{C} + \mathbf{G})\right]^{-1} \mathbf{B} \\ &= \mathbf{L}^T \left[\mathbf{I} + (s_0\mathbf{C} + \mathbf{G})^{-1}\mathbf{C}(s - s_0)\right]^{-1} (s_0\mathbf{C} + \mathbf{G})^{-1}\mathbf{B} \\ &= \sum_{i=0}^{\infty} \mathbf{L}^T \left[-(s_0\mathbf{C} + \mathbf{G})^{-1}\mathbf{C}\right]^i (s_0\mathbf{C} + \mathbf{G})^{-1}\mathbf{B}(s - s_0)^i, \end{aligned} \tag{3.16}$$

where

$$\underbrace{\mathbf{L}^T \left[-(s_0\mathbf{C} + \mathbf{G})^{-1}\mathbf{C}\right]^i (s_0\mathbf{C} + \mathbf{G})^{-1}\mathbf{B}(s - s_0)^i}_{=:\mathbf{m}_i(s_0)},$$

denotes the ith moment $\mathbf{m}_i(s_0)$ of the transfer function $\mathbf{H}(s)$ at the expansion point s_0. In the case of a Single input single output (SISO) system, the terms $\mathbf{m}_i(s_0)$ for $i = 0, 1, 2, \ldots$ are known as the moments of the transfer function $\mathbf{H}(s)$. For multiple input multiple output (MIMO) system, these moments $\mathbf{m}_i(s_0)$ are matrices and are referred to as block moments [110].
For the model in Eq. (3.11), we use the moment matching technique to construct $\mathbf{H}_r(s)$ of (3.12) so that it interpolates the $\mathbf{H}(s)$ at given interpolation points. Using Hermite interpolation ensures the following conditions fulfilled

$$\mathbf{H}_r(\sigma_k) = \mathbf{H}(\sigma_k) \quad \text{and} \quad \mathbf{H}_r'(\sigma_k) = \mathbf{H}'(\sigma_k) \quad \text{for} \quad k = 1, \ldots, r \tag{3.17}$$

If we define

$$Ran(\mathbf{V}) = span\{(\sigma_1\mathbf{C}+\mathbf{G})^{-1}\mathbf{B}, \ldots, (\sigma_r\mathbf{C}+\mathbf{G})^{-1}\mathbf{B}\} \tag{3.18}$$

$$Ran(\mathbf{W}) = span\{(\sigma_1\mathbf{C}+\mathbf{G})^{-1}\mathbf{L}, \ldots, (\sigma_r\mathbf{C}+\mathbf{G})^{-1}\mathbf{L}\}. \tag{3.19}$$

Consider $\mathbf{V}$ and $\mathbf{W}$ as the real matrices, then at each frequency point, the first two moments of $\mathbf{H}(s)$ match. The mathematical proof is provided in the work of C. Beattie et al. [111].
Moment matching offers computational efficiency that scales the system size [109]. Some techniques based on moment matching are proper where frequency-domain accuracy is required [112]. However, Moment matching for the ill-conditioned matrices can be numerically unstable [109]. The accuracy of ROM remains challenging despite the error estimation [108].

3.3.1 Padé and Padé-type approximation

The Padé approximation is a technique for approximating a transfer function in (3.11) as $f(x)$ using a rational expression, which is the ratio of two polynomials:

$$R_{m,n}(x) = \frac{P_m(x)}{Q_n(x)} = \frac{a_0 + a_1x + a_2x^2 + \cdots + a_mx^m}{1 + b_1x + b_2x^2 + \cdots + b_nx^n}. \tag{3.20}$$

In this representation, $P_m(x)$ represents a polynomial of degree m, and $Q_n(x)$ represents a polynomial of degree n, with the constant term of $Q_n(x)$ normalized to 1. The coefficients of $P_m(x)$ and $Q_n(x)$ are chosen so that the Taylor series of $R_{m,n}(x)$ matches as many terms as possible from the Taylor series of $f(x)$. Given that $f(x)$ can be written as a Taylor series

$$f(x) = \sum_{k=0}^{\infty} c_k x^k,$$

the Padé approximation satisfies the relationship

$$f(x) - R_{m,n}(x) = O(x^{m+n+1}), \tag{3.21}$$

ensuring that the series agrees to the term x^{m+n}. By expanding the relation $R_{m,n}(x) \cdot Q_n(x) = P_m(x)$ and comparing it to the Taylor series of $f(x)$, a system of linear equations is derived to compute the coefficients a_i and b_i [113].
The Padé approximation has significant advantages over the Taylor series. While the Taylor series effectively captures local behavior, their convergence may degrade for functions with singularities or complex behavior. In contrast, Padé approximations, due to their rational form, can represent such functions more accurately and

often converge faster over a broader range [87, 114]. Padé approximations find extensive applications in numerical methods, including solving differential equations, approximating transcendental functions, and improving the convergence of series solutions.
In addition to the standard Padé approximation, another method known as the Padé-type approximation is widely used in various fields where the polynomials in the numerator and denominator may be chosen based on behavior at different points or asymptotic properties. The Padé-type approximation is used to solve differential equations to improve the convergence of solutions and accurately represent functions with singularities or other complex features. The Padé-type approximations can enhance performance and accuracy in many numerical applications.
While Padé and Padé-type approximations are powerful methods for model order reduction, they also come with challenges. The issues such as numerical instability, computational complexity, and the potential for non-physical solutions make them less suitable for certain applications.

3.3.2 Krylov subspace and IRKA

Krylov subspace methods, i.e., the Arnoldi and Lanczos algorithms, are commonly used for efficient moment matching in complex dynamical systems. These methods construct a basis for the ROM within a Krylov subspace, which guarantees multiple moments matching implicitly [109]. Block Arnoldi variants also exist for multi-input multi-output (MIMO) systems, making these methods highly versatile [115].
To select the optimal interpolation points, we explain the iterative rational Krylov algorithm (IRKA) here. Let's consider a system $\mathbf{H}_r(s)$ as given in Eq. (3.12) be the local minimizer of the given state space model $\mathbf{H}(s)$ in Eq. (3.11), then as per the proposition (3.3) in [116], $\mathbf{H}_r(s)$ interpolates $\mathbf{H}(s)$ and its first derivative as shown in (3.17) at $-\lambda_i$ where $i = 1, \ldots, r$,
The proof of the proposition is provided in the [116]. The IRKA has been well explained in Algorithm 3.1
The IRKA approach extends the standard Krylov approach by matching moments at multiple frequency points. This capability is especially valuable in applications requiring accuracy across a range of frequencies, balancing the trade-off between accuracy and computational cost [112, 117].

3.3.3 Tangential interpolation based MOR

In Eq. (3.18), we discussed the projection matrices for the single-input, single-output (SISO) systems. In the case of MIMO systems, we use the tangential interpolation [118, 119]. Tangential interpolation is specially used for multi-input multi-output

Algorithm 3.1: IRKA algorithm

Data: $\mathbf{C}$, $\mathbf{G}$, $\mathbf{B}$, $\mathbf{L}$
Result: $\mathbf{C}_r$, $\mathbf{G}_r$, $\mathbf{B}_r$, $\mathbf{L}_r$
Initialization: Make an initial guess for interpolation points σ_i for $i = 1, \ldots, r$;
Choose $\mathbf{V}$ and $\mathbf{W}$ using (3.18) ;
while *change in* $\sigma_i \geq tol$ **do**
    Construct $\mathbf{C}_r$, $\mathbf{G}_r$, $\mathbf{B}_r$, $\mathbf{L}_r$;
    Assign $\sigma_i \leftarrow -\lambda_i(\mathbf{G}_r)$;
    Update $\mathbf{V}$ and $\mathbf{W}$ using (3.18) ;
    Reconstruct $\mathbf{C}_r$, $\mathbf{G}_r$, $\mathbf{B}_r$, $\mathbf{L}_r$ using updated $\mathbf{V}$ and $\mathbf{W}$ such that $\mathbf{W}^T\mathbf{V} = \mathbf{I}$;

(MIMO) systems. The idea is to build an ROM that tangentially interpolates the original model. The projection matrices $\mathbf{V}$ and $\mathbf{W}$ are chosen as

$$Ran(\mathbf{V}) = span\{(\sigma_1\mathbf{C} + \mathbf{G})^{-1}\mathbf{B}\mathbf{b}_1, \ldots, (\sigma_r\mathbf{C} + \mathbf{G})^{-1}\mathbf{B}\mathbf{b}_r\} \tag{3.22}$$
$$Ran(\mathbf{W}) = span\{(\sigma_1\mathbf{C} + \mathbf{G})^{-1}\mathbf{L}\mathbf{l}_1, \ldots, (\sigma_r\mathbf{C} + \mathbf{G})^{-1}\mathbf{L}\mathbf{l}_r\} \tag{3.23}$$

where $\mathbf{b}_i$ and l_i for $i = 1, \ldots, r$ are the tangential directions $\mathbb{R}^{m\times 1}$ and $\mathbb{R}^{p\times 1}$ Tangential interpolation offers an efficient approach to matching moments for MIMO systems. This approach reduces the computational burden while retaining key dynamic properties and is helpful for complex MIMO systems [119, 120].

3.4 Balanced truncation

Balanced truncation is a prominent MOR technique that preserves the input-output behavior of linear time-invariant (LTI) systems while significantly reducing their order [86]. Several other researchers have explored this concept [86, 108, 121–123] The method based on the controllability and observability Gramians of a system, which is crucial in determining the most significant states that should be retained in the ROM. Balanced truncation is a reliable MOR technique due to its stability preservation, error bounds, and adaptability to large-scale systems. With ongoing advancements, particularly in the computational efficiency of Gramian approximations, balanced truncation continues to be a foundational tool for simplifying complex systems in engineering and scientific applications.

For the Eq. (3.1) and Eq. (3.2), the controllability Gramian $\mathbf{W}_c$ is given by

$$\mathbf{W}_c = \int_0^\infty e^{\mathbf{A}t}\mathbf{B}\mathbf{B}^T e^{\mathbf{A}^T t} dt, \tag{3.24}$$

where $\mathbf{A} = -\mathbf{G} \cdot \mathbf{C}^{-1}$. Thus, substituting for $\mathbf{A}$:

$$\mathbf{W}_c = \int_0^\infty e^{-\mathbf{G}t}\mathbf{B}\mathbf{B}^T e^{-\mathbf{G}^T t} dt. \tag{3.25}$$

Similarly, the observability Gramian $\mathbf{W}_o$ is defined as

$$\mathbf{W}_o = \int_0^\infty e^{\mathbf{A}^T t}\mathbf{L}\mathbf{L}^T e^{\mathbf{A}t} dt. \tag{3.26}$$

Substituting for $\mathbf{A}$ yields:

$$\mathbf{W}_o = \int_0^\infty e^{-\mathbf{G}^T t}\mathbf{L}\mathbf{L}^T e^{-\mathbf{G}t} dt. \tag{3.27}$$

Suppose we have a stable LTI system in Eq. (3.1) and (3.2), then the associated Lyapunov equations are represented as:

$$\begin{aligned} (-\mathbf{G})\mathbf{W}_c\mathbf{C}^T + \mathbf{C}\mathbf{W}_c(-\mathbf{G}^T) + \mathbf{B}\mathbf{B}^T = 0, \\ (-\mathbf{G}^T)\mathbf{W}_o\mathbf{C} + \mathbf{C}^T\mathbf{W}_o(-\mathbf{G}) + \mathbf{L}\mathbf{L}^T = 0. \end{aligned} \tag{3.28}$$

In practice, we use the Lyapunov equations to avoid the infinite integral in Eq. (3.25) and Eq. (3.27). Furthermore, we use factorization rather than forming the full Gramians [124, 125], i.e., $\mathbf{W}_c = \mathbf{S}\mathbf{S}^T$ and $\mathbf{W}_o = \mathbf{R}\mathbf{R}^T$. We choose the factorization in such a manner that $\mathbf{R}^T E\mathbf{S} = svd(\mathbf{Z}\mathbf{\Sigma}_n\mathbf{Y}^T)$ where $\mathbf{\Sigma}_n$ has n singular values over the diagonal. In the balance truncation technique, the basis matrices are chosen using

$$\mathbf{V} = \mathbf{S}\mathbf{Z}_r\mathbf{\Sigma}_r^{-1/2}, \mathbf{W} = \mathbf{R}\mathbf{Y}_r\mathbf{\Sigma}_r^{-1/2}, \tag{3.29}$$

where the $\mathbf{\Sigma}_r$ represents the truncated $\mathbf{\Sigma}_n$ with corresponding left singular vectors $\mathbf{Z}_r$ and right singular vectors $\mathbf{Z}_r$. The balancing transformation is achieved through a transformation matrix T that diagonalizes the product of the controllability and observability Gramians which leads to a balanced realization where the states have equal controllability and observability, i.e., $\mathbf{W}_c = \mathbf{W}_o = \mathbf{\Sigma}_n$. The less controllable or observable states can be truncated without significantly affecting the system's behavior. The balance truncation works well for models having a degree of freedom of a few thousand because the solution of the Lyapunov equations for large complex systems becomes very expensive. The balance truncation also does not preserve the passivity of the original model.

3.5 Loewner framework

The Loewner framework was first introduced by Antoulas and Beattie in 2003 as a method to approximate a system's input-output behavior [126]. Constructing a reduced-order model (ROM) using frequency response data is the primary idea. This data is used to formulate the Loewner matrix, which captures the system's input-output behavior and facilitates moment matching between the ROM and the original model. A key advantage of this method is that a ROM can be constructed without complete knowledge of the original model [90].
The Loewner framework involves several steps, beginning with collecting input-output data from the system. This data is then used to define the Loewner matrix, denoted as:

$$\mathbb{L} = \begin{bmatrix} \mathbf{H}(s_1) & \mathbf{H}(s_2) & \cdots & \mathbf{H}(s_m) \end{bmatrix} \tag{3.30}$$

where $\mathbf{H}(s)$ represents the associated outputs at different complex frequencies s_i. The next step is to apply techniques such as interpolation and projection to extract a reduced-order model from the Loewner matrix.
One of the strengths of the Loewner framework is its flexibility in dealing with parameterized systems and uncertain models. This adaptability is achieved through interpolation methods that can accommodate variations in system parameters, making it suitable for applications where system dynamics are subject to change [127]. The Loewner framework has been utilized to create ROMs that accurately capture the dynamic behavior of electronic circuits [108].
In addition to circuit simulation, the Loewner framework has been extended to the reduction of systems with nonlinear dynamics and complex boundary conditions. Recent research has focused on integrating the Loewner framework with other MOR techniques to enhance its applicability and performance in real-time applications [128]. For instance, combining the Loewner framework with moment-matching techniques can lead to more accurate reduced models that maintain the essential characteristics of the original system while still reducing the order significantly. Another advantage of the Loewner framework is its error analysis capabilities [128].

Chapter 4

Reduced order modeling of the delayed PEEC models

Computational electromagnetic (EM) methods [3, 129–132] are widely used to analyze the electromagnetic behavior of complex EM systems. Among these methods, the partial element equivalent circuit (PEEC) method is particularly significant for electromagnetic compatibility (EMC) analysis, interconnect modeling, and antenna design [2, 14, 16]. The PEEC method discretizes dielectric and conductive areas of a system, representing them through a set of partial elements that form an equivalent circuit capturing the EM system's behavior.

The quasi-static PEEC models can be expressed using a series of ordinary differential equations (ODEs) [133]. However, delayed PEEC models have proven to be more effective in accurately representing electrically long structures where propagation delays play a crucial role. These models are formulated using a series of neutral delayed differential equations (NDDEs) [133], which introduce additional computational challenges due to their inherent delay structure. This chapter focuses on the formulation of delayed PEEC models and their representation in state-space form, which serves as a foundation for applying model order reduction (MOR) techniques.

The first part of this chapter presents a brief formulation of delayed PEEC models, starting from Maxwell's equations and their circuit-based representation. The inclusion of delays due to signal propagation effects is discussed, leading to the derivation of state-space equations that incorporate these delay terms. The state-space representation provides a structured mathematical form that facilitates both numerical simulations and the application of MOR techniques.

The second part of the chapter explores MOR techniques, with a specific focus on multipoint moment matching, which has been widely used in the literature to reduce delayed PEEC models efficiently. MOR techniques [134] provide a means to reduce the complexity of large dynamical models while preserving their input-output

behavior, particularly their transfer function characteristics. These techniques significantly reduce computational costs, enabling more efficient resolution of complex EMC problems while ensuring precise results. Although MOR techniques for standard (non-delayed) differential equations [134–139] are well-established, the study of MOR for delayed differential equations, particularly in the context of delayed PEEC models, remains an active area of research [140–145].
A well-known MOR technique for delayed systems is multipoint moment matching, which has been explored in the literature as an efficient approach for reducing delayed PEEC models. In [141], a moment-matching MOR technique was developed explicitly for delayed PEEC models. This method computes system moments using additional state variables while expanding the exponential delay terms $e^{-s\tau_k}$ using a Taylor series. Another approach introduced in [142] employed a multi-order Arnoldi algorithm, which performs moment matching without requiring extra state variables, leading to a more computationally efficient reduction process. Both techniques ensure that the reduced PEEC models retain their NDDE structure, preserving the fundamental delay dynamics. A detailed discussion of multipoint moment matching and its application to delayed PEEC models is provided in this chapter.
The remainder of this chapter is organized as follows: Section 3.1 provides a brief formulation of delayed PEEC models and their transformation into state-space form. Section 3.2 introduces the concept of multipoint moment matching, explaining its theoretical background and how it has been applied to delayed PEEC models in literature, setting the stage for advanced reduction methods in the following chapters.

4.1 MOR of full-wave PEEC models

By employing the center-to-center approximation to compute the partial elements, the MNA form of PEEC models can be derived in a matrix form, and it reads

$$\mathbf{C}(t)\frac{d\mathbf{x}(t)}{dt} = -\mathbf{G}(t)\mathbf{x}(t) + \mathbf{B}\mathbf{u}(t), \tag{4.1a}$$

$$\mathbf{y}(t) = \mathbf{L}^T\mathbf{x}(t), \tag{4.1b}$$

where the vector of the unknowns $\mathbf{x}(t) \in \Re^{n_u \times 1}$ is given as

$$\mathbf{x}(t) = \left[\mathbf{i}(t) \quad \boldsymbol{\phi}_{sr}(t) \quad \boldsymbol{\phi}_i(t) \quad \mathbf{v}_d(t) \quad \mathbf{q}_s(t)\right]^T, \tag{4.2}$$

where $\mathbf{i}(t)$ are the branch currents, $\boldsymbol{\phi}_{sr}(t)$ are the scalar potentials for surface nodes, $\boldsymbol{\phi}_i(t)$ are the scalar potentials for internal nodes, $\mathbf{v}_d(t)$ are the excess capacitance voltages for dielectric branches, and $\mathbf{q}_s(t)$ represent the surface charges. Further-

more, the state space matrices $\mathbf{C}(t)$, $\mathbf{G}(t)$ and $\mathbf{B}$ are:

$$\mathbf{C}(t) = \begin{bmatrix} \underset{n_b\times n_b}{\mathbf{L}_p(t)*} & \underset{n_b\times n_{ns}}{\mathbf{0}} & \underset{n_b\times n_{ni}}{\mathbf{0}} & \underset{n_b\times n_{bd}}{\mathbf{0}} & \underset{n_b\times n_p}{\mathbf{0}} \\ \underset{n_{ns}\times n_b}{\mathbf{0}} & \underset{n_{ns}\times n_{ns}}{\mathbf{0}} & \underset{n_{ns}\times n_{ni}}{\mathbf{0}} & \underset{n_{ns}\times n_{bd}}{\mathbf{0}} & \underset{n_{ns}\times n_p}{\mathbf{M}^T} \\ \underset{n_{ni}\times n_b}{\mathbf{0}} & \underset{n_{ni}\times n_{ns}}{\mathbf{0}} & \underset{n_{ni}\times n_{ni}}{\mathbf{0}} & \underset{n_{ni}\times n_{bd}}{\mathbf{0}} & \underset{n_{ni}\times n_p}{\mathbf{0}} \\ \underset{n_{bd}\times n_b}{\mathbf{0}} & \underset{n_{bd}\times n_{ns}}{\mathbf{0}} & \underset{n_{bd}\times n_{ni}}{\mathbf{0}} & \underset{n_{bd}\times n_{bd}}{\mathbf{C}_d} & \underset{n_{bd}\times n_p}{\mathbf{0}} \\ \underset{n_p\times n_b}{\mathbf{0}} & \underset{n_p\times n_{ns}}{\mathbf{0}} & \underset{n_p\times n_{ni}}{\mathbf{0}} & \underset{n_p\times n_{bd}}{\mathbf{0}} & \underset{n_p\times n_p}{\mathbf{0}} \end{bmatrix}, \tag{4.3}$$

$$\mathbf{G}(t) = \begin{bmatrix} \underset{n_b\times n_b}{\mathbf{R}} & \underset{n_b\times n_{ns}}{\mathbf{A}_s} & \underset{n_b\times n_{ni}}{\mathbf{A}_i} & \underset{n_b\times n_{bd}}{\mathbf{\Gamma}} & \underset{n_b\times n_p}{\mathbf{0}} \\ \underset{n_{ns}\times n_b}{-\mathbf{A}_s^T} & \underset{n_{ns}\times n_{ns}}{\mathbf{0}} & \underset{n_{ns}\times n_{ni}}{\mathbf{0}} & \underset{n_{ns}\times n_{bd}}{\mathbf{0}} & \underset{n_{ns}\times n_p}{\mathbf{0}} \\ \underset{n_{ni}\times n_b}{-\mathbf{A}_i^T} & \underset{n_{ni}\times n_{ns}}{\mathbf{0}} & \underset{n_{ni}\times n_{ni}}{\mathbf{0}} & \underset{n_{ni}\times n_{bd}}{\mathbf{0}} & \underset{n_{ni}\times n_p}{\mathbf{0}} \\ \underset{n_{bd}\times n_b}{-\mathbf{\Gamma}^T} & \underset{n_{bd}\times n_{ns}}{\mathbf{0}} & \underset{n_{bd}\times n_{ni}}{\mathbf{0}} & \underset{n_{bd}\times n_{bd}}{\mathbf{0}} & \underset{n_{bd}\times n_p}{\mathbf{0}} \\ \underset{n_p\times n_b}{\mathbf{0}} & \underset{n_p\times n_{ns}}{-\mathbf{M}} & \underset{n_p\times n_{ni}}{\mathbf{0}} & \underset{n_p\times n_{bd}}{\mathbf{0}} & \underset{n_p\times n_p}{\mathbf{P}(t)*} \end{bmatrix}, \tag{4.4}$$

$$\mathbf{B} = \begin{bmatrix} \underset{n_b\times n_b}{\mathcal{I}} & \underset{n_b\times n_{ns}}{\mathbf{0}} \\ \underset{n_{ns}\times n_b}{\mathbf{0}} & \underset{n_{ns}\times n_{ns}}{\mathcal{I}} \\ \underset{n_{ni}\times n_b}{\mathbf{0}} & \underset{n_{ni}\times n_{ns}}{\mathbf{0}} \\ \underset{n_{bd}\times n_b}{\mathbf{0}} & \underset{n_{bd}\times n_{ns}}{\mathbf{0}} \\ \underset{n_p\times n_b}{\mathbf{0}} & \underset{n_p\times n_{ns}}{\mathbf{0}} \end{bmatrix}, \tag{4.5}$$

where $*$ represents the convolution operator, and n_b, n_{ns}, n_{ni}, n_{bd} and n_p represent the cardinality of branches, surface nodes, internal nodes, dielectric cells and surface cells, respectively. Moreover, $\mathbf{C}_d$ is the excess capacitance matrix [146], $\mathbf{R}$ is the branches resistance matrix, $\mathbf{A}_s$ is the incidence matrix for the surface nodes, $\mathbf{A}_i$ is the incidence matrix for the internal nodes, $\mathbf{\Gamma}$ is the dielectric region selection matrix, and $\mathbf{M}$ is the surface-to-node reduction matrix.
The time-dependent partial inductance matrix $\mathbf{L}_p(t)$ and the coefficient of potential matrix $\mathbf{P}(t)$ are derived from (2.52) and (2.43) and read

$$\mathbf{L}_p(t) = \mathbf{L}_{p,0}\delta(t) + \sum_{k=1}^{n_{\tau_L}} \mathbf{L}_{p,k}\delta(t-\tau_{L,k}), \tag{4.6a}$$

$$\mathbf{P}(t) = \mathbf{P}_0\delta(t) + \sum_{q=1}^{n_{\tau_P}} \mathbf{P}_k\delta(t-\tau_{P,q}), \tag{4.6b}$$

where the matrices $\mathbf{L}_{p,0}$ and $\mathbf{P}_0$ account for the delayless magnetic and electric couplings while $\mathbf{L}_{p,k}, k = 1, \cdots, n_{\tau_L}$, and $\mathbf{P}_k, k = 1, \cdots, n_{\tau_P}$ take the propagation

delay into account;n_{τ_L} is the number of significant delays between elementary volumes while n_{τ_P} is the number of significant delays between elementary surfaces; $\tau_{L,i} = R_{cc,i}/c_0, i = 1, \cdots, n_{\tau_L}$ and $\tau_{P,q} = R_{cc,q}/c_0, q = 1, \cdots, n_{\tau_P}$ denote the delays between the centers, identified by $R_{cc,i}$ and $R_{cc,q}$ respectively, of the spatial supports of the basis functions of currents and charges; c_0 is the speed of the light in the background medium.
Finally, the source vector $\mathbf{u}(t)$ is given as

$$\mathbf{u} = \begin{bmatrix} \mathbf{v}_s(t) \\ \mathbf{i}_s(t) \end{bmatrix}, \tag{4.7}$$

where $\mathbf{v}_s(t)$ and $\mathbf{i}_s(t)$ are the voltage and current sources applied to branches and nodes, respectively. It is also worth observing that the proposed PEEC formulation, based on charge and current basis functions, is more robust towards the so-called low-frequency breakdown, as confirmed in [147, 148], resulting in a full spectrum methodology.
Equations (4.1) form a system of delayed differential equations of the neutral type (NDDEs), where the delays exist not only in the state vector $\mathbf{x}(t)$ but also in its time derivative $d\mathbf{x}(t)/dt$. Each delayed component in the matrices $\mathbf{C}(\boldsymbol{\tau})$ and $\mathbf{G}(\boldsymbol{\tau})$ acts as a delay operator for the corresponding component in the vector $\mathbf{x}(t)$. Therefore, (4.1a) can be reformulated in the Laplace domain as:

$$\begin{aligned}
s\mathbf{C}(s)\mathbf{X}(s) &= -\mathbf{G}(s)\mathbf{X}(s) + \mathbf{B}\mathbf{U}(s), && \text{(4.8a)}\\
\mathbf{Y}(s) &= \mathbf{B}^T\mathbf{X}(s), && \text{(4.8b)}\\
\mathbf{C}(s) &= \mathbf{C}_0 + \sum_{k=1}^{n_{\tau_{L_p}}} \mathbf{C}_k e^{-s\tau_{L,k}}, && \text{(4.8c)}\\
\mathbf{G}(s) &= \mathbf{G}_0 + \sum_{k=1}^{n_{\tau_P}} \mathbf{G}_k e^{-s\tau_{P,k}}. && \text{(4.8d)}
\end{aligned}$$

A reduced-order model can be written as

$$\begin{aligned}
s\mathbf{C}_r(s)\mathbf{X}_r(s) &= -\mathbf{G}_r(s)\mathbf{X}_r(s) + \mathbf{B}_r\mathbf{U}(s), && \text{(4.9a)}\\
\mathbf{Y}(s) &= \mathbf{B}_r^T\mathbf{X}_r(s), && \text{(4.9b)}\\
\mathbf{C}_r(s) &= \mathbf{C}_{r,0} + \sum_{k=1}^{n_{\tau_L}} \mathbf{C}_{r,k} e^{-s\tau_{L,k}}, && \text{(4.9c)}\\
\mathbf{G}_r(s) &= \mathbf{G}_{r,0} + \sum_{k=1}^{n_{\tau_P}} \mathbf{G}_{r,k} e^{-s\tau_{P,k}}. && \text{(4.9d)}
\end{aligned}$$

where the following congruence transformations based on the orthogonal matrix $\mathbf{K} \in \Re^{n_u \times n_r}$ are employed

$$\begin{aligned}
\mathbf{C}_{r,i} &= \mathbf{K}^T \mathbf{C}_i \mathbf{K}, \qquad i = 0, \ldots, n_{\tau_{L_p}}, && (4.10a)\\
\mathbf{G}_{r,i} &= \mathbf{K}^T \mathbf{G}_i \mathbf{K}, \qquad i = 0, \ldots, n_{\tau_P}, && (4.10b)\\
\mathbf{B}_r &= \mathbf{K}^T \mathbf{B}, && (4.10c)\\
\mathbf{L}_r &= \mathbf{K}^T \mathbf{L}. && (4.10d)
\end{aligned}$$

The same reduced order model in the time domain can be written as

$$\begin{aligned}
\mathbf{C}_{r,0}\left(t\right)\frac{d\mathbf{x}_r(t)}{dt} &= -\mathbf{G}_{r,0}\left(t\right)\mathbf{x}_r(t) - \sum_{k=1}^{n_{\tau_L}} \mathbf{C}_{r,k}\frac{dx_r}{dt}(t-\tau_k)\\
&- \sum_{k=1}^{n_{\tau_P}} \mathbf{G}_{r,k} x_r(t-\tau_k) + \mathbf{B}_r\mathbf{u}(t), && (4.11a)\\
\mathbf{y}(t) &= \mathbf{L}_r^T \mathbf{x}_r(t), && (4.11b)
\end{aligned}$$

where the vector $\mathbf{x}_r(t)$ represents the reduced state variables. NDDEs (4.11) can be rewritten in a more compact form as:

$$\mathbf{C}_{r,0}\frac{d\mathbf{x}_r(t)}{dt} + \mathbf{G}_{r,0}\mathbf{x}_r(t) = \mathbf{T} + \mathbf{B}_r\mathbf{u}(t), \tag{4.12}$$

where

$$\mathbf{T} = -\sum_{k=1}^{n_{\tau_L}} \mathbf{C}_{r,k}\frac{dx_r}{dt}(t-\tau_k) - \sum_{k=1}^{n_{\tau_P}} \mathbf{G}_{r,k} x_r(t-\tau_k). \tag{4.13}$$

Concerning time-domain simulations of delayed PEEC models, assuming a uniform time step, NDDEs (4.11a) can be integrated using one or two-step integration methods. The general form of the solution using two-step methods reads:

$$\alpha\frac{d\mathbf{x}(t)}{dt} = \mu_p\mathbf{x}_p + \mu_{p-1}\mathbf{x}_{p-1} + \mu_{p-2}\mathbf{x}_{p-2} - \beta\frac{d\mathbf{x}_{p-1}(t)}{dt}, \tag{4.14}$$

where the subscript p identifies the time step and homogeneous initial conditions are set for $\mathbf{x}_{p-1}$, $\mathbf{x}_{p-2}$, and $\frac{d\mathbf{x}_{p-1}(t)}{dt}$. The coefficients for each method are given in Table 4.1.
Applying the scheme (4.14) to (4.12), we obtain

$$\begin{aligned}
&\frac{\mu_p}{\alpha}\mathbf{C}_{r,0}\mathbf{x}_p + \mathbf{G}_{r,0}\mathbf{x}_p = \mathbf{B}\mathbf{u}_p + \mathbf{T}_p\\
&\quad - \mathbf{C}_{r,0}\left(\frac{\mu_{p-1}}{\alpha}\mathbf{x}_{p-1} + \frac{\mu_{p-2}}{\alpha}\mathbf{x}_{p-2} - \frac{\beta}{\alpha}\frac{d\mathbf{x}_{p-1}(t)}{dt}\right),
\end{aligned} \tag{4.15}$$

Table 4.1: Time integration methods.

Integration method	$\mu_{\mathbf{p}}$	$\mu_{\mathbf{p-1}}$	$\mu_{\mathbf{p-2}}$	α	β
BE (Backward Euler)	$1/h$	$-1/h$	0	1	0
BD2 (Gear)	$1.5/h$	$-2/h$	$1/(2h)$	1	0
Trapezoidal	$1/h$	$-1/h$	0	0.5	0.5
Theta θ	$1/h$	$-1/h$	0	θ	$1-\theta$

where $\mathbf{T}_p$ is the time discrete counterpart of $\mathbf{T}$ in (4.12). The same time-domain simulation approach can be used for original and reduced-order PEEC models. The numerical results show that time-domain simulations of the POD-based reduced order models will be much faster than the original delayed PEEC models while preserving high accuracy. A two-step time-domain integration method was used to obtain time-domain results, as shown in the numerical examples.

4.2 Mutlipoint moment matching technique for delayed PEEC model

The multiorder Arnoldi algorithm is designed to construct a reduced-order model for systems requiring accurate representation over multiple frequencies, particularly for delayed PEEC models where retardation effects are significant [132, 139, 145]. The procedure builds a reduced system that approximates the original model's behavior over a range of selected frequencies by creating a combined Krylov subspace that spans these points.

The technique involves multipoint moment matching to develop a ROM for PEEC models incorporating delay effects [14, 15]. This method optimizes the computational efficiency of PEEC models, which are often used in analyzing electromagnetic problems but can be computationally intense due to their high dimensionality, especially when delays are considered. Multipoint moment matching enables the MOR to capture key dynamics effectively across multiple frequency points, thereby ensuring accuracy in the presence of delays.

Let's explain Arnoldi's algorithm for the delayed PEEC models [142]. The idea is to expand the exponential of the Eq. (4.8c) and (4.8d) using the polynomial series as shown in Eq. (4.16)

$$e^{-t_d s} \approx e^{-t_d s_0} \left(\sum_{i=0}^{M} \frac{(-t_d)^i}{i!} (s - s_0)^i \right), \tag{4.16}$$

where M represents the order, and s_0 is the expansion point of the polynomial.

$$\left(\sum_{i=0}^{M} \mathbf{\Phi}_i \left(s - s_0\right)^i\right) \mathbf{X}(s) = \mathbf{B}\mathbf{u}(s),$$

where

$$\mathbf{\Phi_i} = \begin{cases} \mathbf{G}_0 + s_0\mathbf{C}_0 + \sum_{k=1}^{n_r} \left(s_0\mathbf{C}_k + \mathbf{G}_k\right) e^{-s_0 t_{dk}}, & i = 0 \\ \mathbf{C}_0 + \sum_{k=1}^{n_r} \mathbf{C}_k e^{-s_0 t_{dk}} + \sum_{k=1}^{n_r} \left(s_0\mathbf{C}_k + \mathbf{G}_k\right) e^{-s_0 t_{dk}} \left(-t_{dk}\right), & i = 1 \\ \sum_{k=1}^{n_r} \mathbf{C}_k e^{-s_0 t_{dk}} \frac{(-t_{dk})^{i-1}}{(i-1)!} + \sum_{k=1}^{n_r} \left(s_0\mathbf{C}_k + \mathbf{G}_k\right) e^{-s_0 t_{dk}} \frac{(-t_{dk})^{i}}{i!}, & i \geq 2 \end{cases} . \tag{4.17}$$

We represent our model using a polynomial series [142, 149–151] as

$$\left(\tilde{\mathbf{G}} + \left(s - s_0\right)\tilde{\mathbf{C}}\right)\tilde{\mathbf{X}} = \tilde{\mathbf{B}}\mathbf{u} \tag{4.18}$$

If the identity matrix is represented by $\mathbf{I}$, then the matrices are given as:

$$\tilde{\mathbf{G}} = \begin{bmatrix} \mathbf{\Phi_0} & \mathbf{0} & \mathbf{0} & \mathbf{0} & \dots & \mathbf{0} \\ \mathbf{0} & \mathbf{I} & \mathbf{0} & \mathbf{0} & \dots & \mathbf{0} \\ \mathbf{0} & \mathbf{0} & \mathbf{I} & \mathbf{0} & \dots & \mathbf{0} \\ \vdots & & & & & \\ \vdots & & & & & \\ \mathbf{0} & \mathbf{0} & & & & \mathbf{I} \end{bmatrix}$$

$$\tilde{\mathbf{C}} = \begin{bmatrix} \mathbf{\Phi_1} & \mathbf{\Phi_2} & \mathbf{\Phi}_3 & \mathbf{\Phi}_4 & \dots & \mathbf{\Phi_M} \\ \mathbf{-I} & \mathbf{0} & \mathbf{0} & \mathbf{0} & \dots & \mathbf{0} \\ \mathbf{0} & \mathbf{-I} & 0 & 0 & \dots & 0 \\ \vdots & & & & & \\ \vdots & & & & & \\ \mathbf{0} & 0 & & & & 0 \end{bmatrix} \tag{4.19}$$

$$\tilde{\mathbf{X}} = \begin{bmatrix} \mathbf{X} \\ \mathbf{Z_2} \\ \mathbf{Z_3} \\ \vdots \\ \vdots \\ \mathbf{Z_M} \end{bmatrix} \quad \tilde{\mathbf{B}} = \begin{bmatrix} \mathbf{B} \\ \mathbf{0} \\ \mathbf{0} \\ \vdots \\ \vdots \\ \mathbf{0} \end{bmatrix}$$

Next, we use the multi-order Arnoldi algorithm [152–156] to evaluate the moments of the original PEEC model. We expand the $\mathbf{X}(s)$ as a power series i.e. $\mathbf{X}(s) =$

$\left(\sum_{i=0}^{n} \mathbf{M}_i \left(s - s_0\right)^i\right)$. Let's define $\mathbf{R} = \mathbf{\Phi}_0^{-1}\mathbf{B}$ and $\mathbf{A}_i = \mathbf{\Phi}_0^{-1}\mathbf{\Phi}_i$ for $i = 1, 2, \ldots, n$, we get the recursive relationship as

$$\begin{aligned} \mathbf{M}_0 &= \mathbf{R} \\ \mathbf{M}_1 &= \mathbf{A}_1 + \mathbf{M}_0 \\ &\ldots \\ \mathbf{M}_n &= \left(\sum_{i=1} \mathbf{A}_i \mathbf{M}_{n-i}\right). \end{aligned} \tag{4.20}$$

Since the higher-order moments converge to the largest eigenvalue of the model, Rasekh and Dounavis proposed the multi-order Arnoldi algorithm in [142] for PEEC models, which is presented here as Algorithm 4.1.

Algorithm 4.1: Multiorder Arnoldi algorithm for the delayed PEEC model

Data: $\mathbf{B}$, $\mathbf{\Phi}_0$, $\mathbf{\Phi}_i$, q, p, M
Result: $\mathbf{Q}$

Solve $\mathbf{\Phi}_0\mathbf{R} = \mathbf{B}$ for $\mathbf{R}$;
$(\mathbf{q}_0, \mathbf{K}) = \mathrm{qr}(\mathbf{R})$; QR factorization of $\mathbf{R}$;
Set $p =$ number of ports ;
Set $M =$ order of polynomials in (4.16) ;
Set $n = \mathrm{int}(q/p) + 1$;
for $k = 1, 2, \ldots, n-1$ **do**
    Solve $\mathbf{\Phi}_0\mathbf{A}_k = -\mathbf{\Phi}_i$ for $\mathbf{A}_k$;
    Set $m = \min\{k, M\}$;
    $\mathbf{q}_k^{(0)} = \sum_{j=1}^{m} \mathbf{A}_j \mathbf{q}_{k-j}$;
    for $j = 1, \ldots, k$ **do**
        $\mathbf{H} = \mathbf{q}_{k-j}^T \mathbf{q}_k^{(j-1)}$;
        $\mathbf{q}_k^{(j)} = \mathbf{q}_k^{(j-1)} - \mathbf{q}_{k-j}\mathbf{H}$;
    $(\mathbf{q}_k, \mathbf{K}) = \mathrm{qr}\left(\mathbf{q}_k^{(k)}\right)$; QR factorization of $\mathbf{q}_k^{(k)}$;
Set $\mathbf{Q} = [\mathbf{q}_0, \mathbf{q}_1, \ldots, \mathbf{q}_{n-1}]$ and truncate $\mathbf{Q}$ so that it has q columns only.

Chapter 5

MOR of delayed PEEC models using POD techniques

This chapter is based on author's published work[1].

Proper orthogonal decomposition (POD) is a widely used technique for model order reduction (MOR), particularly in large-scale computational electromagnetics. However, traditional POD methods often involve computationally expensive singular value decomposition (SVD) operations, making them inefficient for large systems. This chapter presents an advanced model reduction method based on incremental POD, specifically designed to enhance computational efficiency in the frequency domain as well as time domain.

MOR based on POD is extensively utilized in diverse fields, including fluid dynamics [157], inverse problems [158], optimization problems constrained by partial differential equations [159], and electromagnetics [160, 161]. This approach entails collecting a series of state vector solutions (snapshots) [162] and then constructing the **K** matrix. In the present study, these snapshots are obtained in the frequency domain.

The chapter begins by explaining the concept of snapshot collection in POD-based MOR and how an incremental approach improves efficiency by avoiding the need for a single large SVD operation. Instead, multiple smaller SVDs are performed iteratively, reducing memory requirements and computational costs.

The methodology for implementing incremental POD is described in detail, includ-

[1]M. A. Khattak, D. Romano, G. Antonini, and F. Ferranti, "Proper Orthogonal Decomposition-Based Model Order Reduction of Delayed PEEC Models," 2023 International Conference on Electromagnetics in Advanced Applications (ICEAA), Venice, Italy, 2023, pp. 554-558.

M. A. Khattak, D. Romano, G. Antonini, and F. Ferranti, "Efficient Frequency and Time-Domain Simulations of Delayed PEEC Models With Proper Orthogonal Decomposition Techniques," IEEE Access, vol. 12, pp. 168-178, Dec. 2023.

ing rank truncation and maintaining accuracy in the reduced-order model. Several numerical case studies are presented to validate the effectiveness of incremental POD, demonstrating its ability to significantly accelerate the simulation of delayed PEEC models while preserving high accuracy.
The chapter concludes with a discussion on potential limitations and future improvements, particularly in integrating incremental POD with other MOR techniques for hybrid reduction strategies.

5.1 Frequency domain proper orthogonal decomposition

In a frequency-domain POD approach, we consider a snapshot matrix as $\mathbf{X}_{snapshot} = (\mathbf{X}_1, \ldots, \mathbf{X}_l)$ with l snapshots (samples) in the frequency-domain. From Eq. (4.8b), we consider the snapshots related to

$$\mathcal{H}(s) = (s\mathbf{C}(s) + \mathbf{G}(s))^{-1}\mathbf{B}. \tag{5.1}$$

where $s = jw$. The snapshots are collected for a certain set of frequencies. We use the Algorithm 5.1 to generate the orthonormal basis $\mathbf{K} \in \Re^{n_u \times n_r}$ needed to generate

Algorithm 5.1: FD-POD for delayed PEEC models

Data: $\mathbf{C}$, $\mathbf{G}$, $\mathbf{B}$, n_p (number of ports)
Result: $\mathbf{K}$

Initialization: Set $i = 1$, $\mathbf{V} = []$, and let q be the number of singular vectors to be chosen. ;
while $i \leq n_p$ **do**
    Consider $s = s_1, s_2, \ldots, s_q$ on the imaginary axis and construct snapshot matrix $\mathcal{H}_i(s)$. ;
    Compute POD vectors: $\mathbf{V}_i = [\Re(\mathcal{H}_i(s)), \Im(\mathcal{H}_i(s))]$. ;
    Increment index: $i = i + 1$. ;
Compute singular value decomposition ;

$$\mathbf{K}\mathbf{\Sigma}\mathbf{U}^T = \mathrm{SVD}(\mathbf{V}_1, \mathbf{V}_2, \ldots, \mathbf{V}_{n_p})$$

Perform possible column size reduction for $\mathbf{K}$ based on singular value analysis.

the reduced order model in Eq. (4.12) by final congruence transformations.

5.2 Incremental POD in frequency domain

Constructing the orthogonal basis $\mathbf{K}$ is crucial in obtaining a compact and accurate reduced-order model across a wide frequency range. Although MOR techniques for systems described by (non-delayed) differential equations [134–138] are well-established, the focus on MOR techniques for delayed differential equations and delayed PEEC models is a relatively recent research area [140–144]. In [141, 142], moment-matching MOR techniques were proposed for PEEC models described by NDDEs. Calculating moments for the MOR step can lead to a significant computational cost to generate the orthogonal matrix needed to compute the reduced order matrices. Also, it requires to store in memory the full original matrices that can be very large. POD-based MOR is a solution to these issues of the moment matching MOR.
POD-based MOR is commonly used in various problems ranging from fluid dynamics [157] to inverse problems [158] and partial differential equations (PDEs) constrained optimization problems [159]. Time-domain or frequency-domain simulations of the original system can be the source of information needed to extract the POD basis vectors [163–169]. In this work, we consider snapshots in the frequency-domain. Considering a set of q frequencies $s \in \{s_1, s_2, \ldots, s_q\}$ ($s = j\omega$), then the corresponding snapshots at this given set of frequencies are represented as

$$\mathbf{X}_{\text{ss}} = [\Re(\mathcal{H}(s_1)), \Im(\mathcal{H}(s_1)), \ldots, \Re(\mathcal{H}(s_q)), \Im(\mathcal{H}(s_q))], \tag{5.2}$$

where $\mathbf{X}_{\text{ss}} \in \Re^{n_u \times q}$ represents the snapshot matrix and

$$\mathcal{H}(s) = (s\mathbf{C}(s) + \mathbf{G}(s))^{-1}\mathbf{B}. \tag{5.3}$$

Applying singular value decomposition (SVD) to the snapshot matrix

$$\mathbf{X_{ss}} = \mathbf{U}\mathbf{\Sigma}\mathbf{V}^T, \tag{5.4}$$

where $\mathbf{U} = [\mathbf{u}_1, \mathbf{u}_2, \ldots, \mathbf{u}_q] \in \Re^{n \times q}$ and $\mathbf{V} = [\mathbf{v}_1, \mathbf{v}_2, \ldots, \mathbf{v}_q] \in \Re^{n \times q}$ are orthogonal matrices $\Sigma \in \Re^{q \times q}$ represents the singular values of $\mathbf{X_{ss}}$ at diagonals i.e. $diag(\sigma_1, \sigma_2, \ldots, \sigma_q)$. A truncation on the maximum number of singular values can be used to decide the reduced order n_r. The $\mathbf{V}$ matrix is used as the orthogonal matrix $\mathbf{K}$ needed to generate the reduced order matrices by congruence transformations.
In a traditional POD approach, a one-shot traditional SVD decomposition is applied to the snapshot matrix $\mathbf{X_{ss}}$ to extract an orthogonal matrix needed for the congruence transformations. In addition to this traditional SVD decomposition, in this work, we also explore the concept of incrementally computed singular value decomposition (INCR-SVD) in which the SVD of the whole matrix is not evaluated. Still, the singular vectors are constructed incrementally [170–172]. This can provide computational advantages and flexibility in adding snapshots incrementally. The main

idea behind this is to use subsequent additive modifications of the snapshot matrix where new snapshots are incrementally added. The reader can refer to [170–172] for extensive details on implementing the incremental SVD. We report the main notions related to the incremental SVD. It allows flexibility at multiple levels, from avoiding the need to have all snapshots together as in a one-shot SVD to being able to add snapshots, if needed, incrementally. To formulate the incrementally computed SVD, we have the following steps:

1. Let us consider the snapshot matrix $\mathbf{X}_{ss}$ defined in Eq. (5.4), then we define

$$\mathbf{A}_1 = \mathbf{X}_{ss}(:, 1:m), \tag{5.5}$$
$$\mathbf{A}_2 = \mathbf{X}_{ss}(:, m+1:q). \tag{5.6}$$

   where $\mathbf{A}_1 \in \mathbb{R}^{n_u \times m}$, $\mathbf{A}_2 \in \mathbb{R}^{n_u \times q-m}$ and m is the number of snapshots that formed the initial snapshot matrix of which an SVD is performed.

2. We apply a standard SVD to $\mathbf{A}_1$ as

$$\mathbf{A}_1 = \mathbf{U}_1 \mathbf{\Sigma}_1 \mathbf{V}_1^T. \tag{5.7}$$

   Next, we assume to update the initial SVD of $\mathbf{A}_1$ by considering a block of k columns of $\mathbf{A}_2$ inside a loop till all columns of $\mathbf{A}_2$ are considered as better clarified in what follows.

3. For each block of k columns of $\mathbf{A}_2$, we define

$$\mathbf{M} = \mathbf{U}_1^\top \mathbf{A}_2(:, k*(i-1)+1 : k*i)), \tag{5.8}$$
$$\mathbf{P} = \mathbf{A}_2(:, k*(i-1)+1 : k*i)) - \mathbf{U}_1\mathbf{M}. \tag{5.9}$$

4. We evaluate the QR factorization of $\mathbf{P}$

$$[\mathbf{Q}_P \quad \mathbf{R}_P] \ = qr(\mathbf{P}). \tag{5.10}$$

   When k is small, this algorithm is invoked frequently, and algebraic subspace rotations involved possibly do not preserve orthogonality. Hence, a numerically induced loss of orthogonality of the matrix $\left[\begin{array}{cc} \mathbf{U}_1 & \mathbf{Q}_P \end{array}\right]$ may occur. Therefore, we apply the QR decomposition to it as shown in Eq. (5.11)

$$[\mathbf{Q}_Q \quad \mathbf{R}_Q] \ = qr(\left[\begin{array}{cc} \mathbf{U}_1 & \mathbf{Q}_P \end{array}\right]) \tag{5.11}$$

5. We then evaluate the SVD decomposition $\mathbf{U}_P\,\mathbf{\Sigma}_P, \mathbf{V}_P$ of $\mathbf{D}$ which is defined as

$$\mathbf{D} = \mathbf{R}_Q \left[\begin{array}{cc} \mathbf{\Sigma}_1 & \mathbf{M} \\ 0 & \mathbf{R}_P \end{array}\right] \tag{5.12}$$

We evaluate the incrementally updated SVD as follows

$$\widetilde{\mathbf{\Sigma}}_P = \mathbf{\Sigma}_P(1:t, 1:t) \tag{5.13}$$

$$\widetilde{\mathbf{V}}_P = \begin{bmatrix} \mathbf{V} & 0 \\ 0 & \mathbf{I} \end{bmatrix} \mathbf{V}_P(1:t, 1:t) \tag{5.14}$$

$$\widetilde{\mathbf{U}}_P = \mathbf{Q}_Q \mathbf{U}_P(1:t, 1:t) \tag{5.15}$$

where t can be used as a rank truncation threshold. If no truncation is performed, then t is the total number of columns of $\mathbf{U}_1$ and $\mathbf{P}$.

6. Finally, we update

$$\mathbf{\Sigma}_1 = \widetilde{\mathbf{\Sigma}}_P, \mathbf{V}_1 = \widetilde{\mathbf{V}}_P, \mathbf{U}_1 = \widetilde{\mathbf{U}}_P \tag{5.16}$$

Steps 3-6 are repeated for the different blocks of columns of $\mathbf{A}_2$ till all columns of $\mathbf{A}_2$ are considered.

Low-rank truncation and parallelization strategies can be essential to enhance the computational efficiency of the incremental SVD. For example, the QR factorization can be implemented efficiently using parallelism approaches [173]. The incremental SVD can work by adding a column vector at a time or a matrix with a certain number of columns at a time to an original SVD decomposition. The steps of the incremental SVD-based POD MOR technique we propose for delayed PEEC models are described in Algorithm 5.2. It is worth noticing that if new snapshot information needs to be added and a standard one-shot SVD approach is used, a new one-shot SVD needs to be performed of the previous snapshot matrix augmented by the new snapshot vectors.
This algorithm is used to generate the orthonormal basis $\mathbf{K} \in \Re^{n_u \times n_r}$ required to build the reduced order model in Eq. (4.11) through subsequent congruence transformations.
In the case of a one-shot SVD, the operation mentioned as $INCR - SVD$ in Algorithm 5.2 is replaced by a standard SVD. The operation $INCR - SVD$ in Algorithm 5.2 could also be combined with an adaptive selection of the snapshot samples, but this is beyond the scope of this work and an objective for future work.

5.3 Numerical results

To test our methodology, we consider two different examples of MOR of delayed PEEC models. We denote the full original model as FOM, while the model constructed using Algorithm 5.2 is denoted by INCR-FDPOD, and the standard POD with a one-shot SVD is denoted as FD-POD. FD stands for frequency domain since we use snapshots in the frequency domain to build the reduced-order models. We also compare the results with the multipoint expansion moment matching

Algorithm 5.2: INCR-FDPOD for delayed PEEC models

Data: $\mathbf{C}$, $\mathbf{G}$, $\mathbf{B}$, n_p = number of ports, k = columns of $\mathbf{A}_1$, m = columns of $\mathbf{X}_{ss}$
Result: $\mathbf{K}$
Initialization: Set $i = 1$, $\mathbf{X} = []$, q = number of singular vectors to be chosen, n_r = order of the reduced order model ;
Consider $s = s_1, s_2, \ldots, s_q$ on the imaginary axis and construct snapshot matrix as $\mathcal{H}_{1,\ldots,n_p}(s)$;
while $i \leq n_p$ **do**
    Get snapshot vectors: $\mathbf{X}_i = [\Re(\mathcal{H}_i(s)), \Im(\mathcal{H}_i(s))]$;
    $i = i + 1$;
Construct $\mathbf{A}_1$ and $\mathbf{A}_2$; % Eq. (5.5) and Eq. (5.6) ;
Compute $\mathbf{U}_1, \mathbf{\Sigma}_1, \mathbf{V}_1$ by a standard SVD ;
for $i = 1$ *to* $\lceil((q-m)/k)\rceil$ **do**
    Define $\mathbf{M}$ and $\mathbf{P}$; % Eq. (5.8) and Eq. (5.9) ;
    Find $\mathbf{Q}_P$ and $\mathbf{R}_P$; % Eq. (5.10) ;
    Find $\mathbf{Q}_Q$ and $\mathbf{R}_Q$; % Eq. (5.11) ;
    Evaluate the updated SVD % Eq. (5.13) to Eq. (5.15) ;
    Update $\mathbf{\Sigma}_1 = \widetilde{\mathbf{\Sigma}}_P$, $\mathbf{V}_1 = \widetilde{\mathbf{V}}_P$, $\mathbf{U}_1 = \widetilde{\mathbf{U}}_P$;
Choose $\mathbf{K} = \mathbf{U}_1$.

method [174] denoted as MM-mp. We computed the scattering parameters for both examples to verify the reduced order model (ROM) accuracy compared to the full order model (FOM). We analyze the error in the frequency and time domains to check the proposed technique's accuracy. We denote the original model as *FOM*. All the tests were performed with the MATLAB R2021a [175] on a Windows 10 pro platform having Intel(R) Xeon(R) CPU X5677 @ 3.47GHz 3.46 GHz (2 processors) and 176 GB RAM.

5.3.1 L-shaped conductor over a ground plane

The proposed MOR approach has been tested on the L-shaped conductor over a ground plane sketched in Fig. 5.1. The conductors are assumed to be copper.

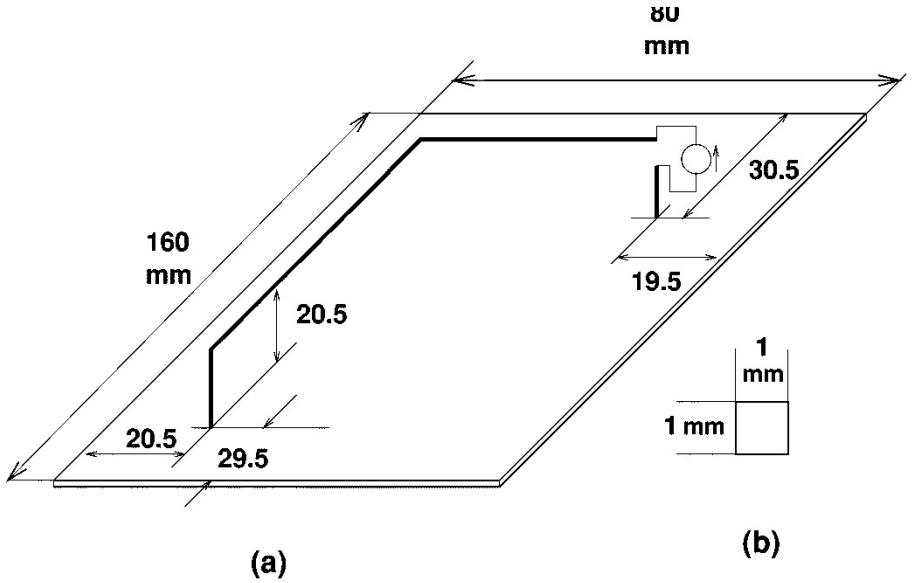


Figure 5.1: Geometry of the L-shaped conductor over a ground plane.

The original model entails $n_u = 9707$ degrees of freedom with $n_I = 2$ inputs and $n_O = 2$ outputs. There are $n_{\tau_L} = 294$ and $n_{\tau_P} = 297$ delays for the magnetic and electric field couplings, respectively. Using Algorithm 5.2, we obtain a POD-based reduced order model of size $n_r = 48$ utilizing 12 snapshots uniformly distributed in the frequency range [1 MHz, 2 GHz]. The computation of the $\mathbf{K}$ matrix of the INCR-FDPOD and FD-POD methods has been done using the INCR-SVD and one-shot standard SVD methods, respectively. In the case of $MM - mp$, we use three expansion points [10 Hz, 1 GHz, 2 GHz] and obtain a reduced-order model of the

same size. The CPU time required to construct the INCR-FDPOD and FD-POD model equals 3464 s and 3403 s, while that of the MM-mp model is 7269 s. A CPU time comparison related to the construction of the different reduced order models and the size of each reduced model is shown in Table 5.1.

Model	Size	Construction Time (s)
FOM-dir	9707	-
INCR-FDPOD	48	3464
FD-POD	48	3403
MM-mp	48	7269

Table 5.1: Construction time and size of the reduced order models for the L-shaped conductor over a ground plane example.

We also analyze the CPU time needed to evaluate the scattering parameters for a frequency sample by the different models, and we illustrate it in Table 5.2.

Model	Evaluation Time (s)
FOM	344
INCR-FDPOD	$1.185 \cdot 10^{-2}$
FD-POD	$1.161 \cdot 10^{-2}$
MM-mp	$1.543 \cdot 10^{-2}$

Table 5.2: CPU time comparison for a single frequency sample evaluation of the scattering parameters for the L-shaped conductor over a ground plane example.

To assess the accuracy of the reduced order models compared to the FOM, we generate a plot illustrating the magnitude spectra of the scattering parameters. Figs. 5.2-5.3 show the magnitude spectra of the S_{11} and S_{21} parameters, respectively, as obtained by the FOM and the reduced order models.

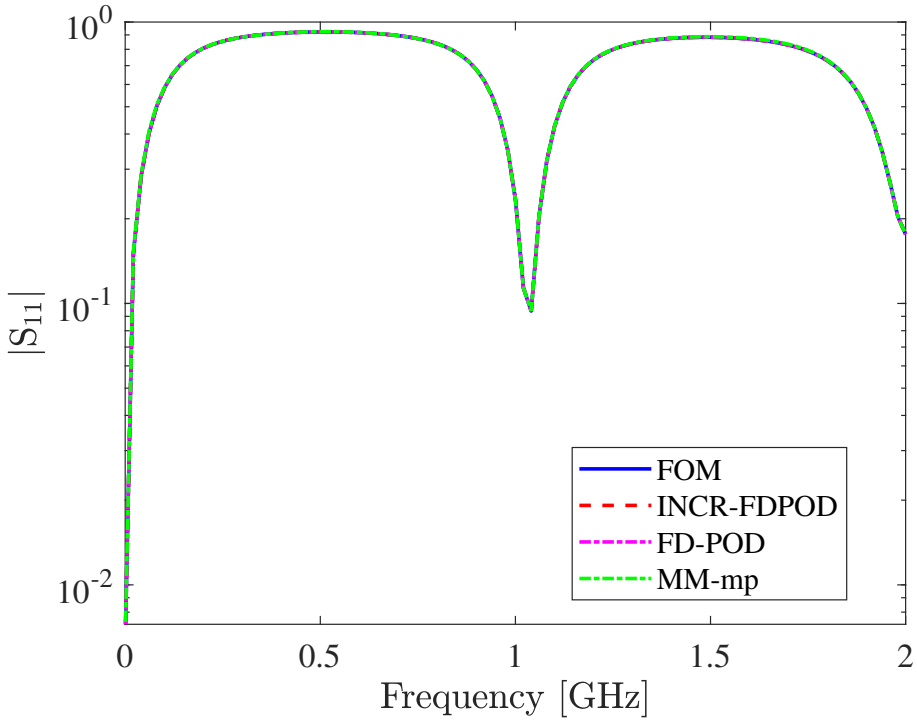


Figure 5.2: Magnitude of S_{11} for the L-shaped conductor over the ground plane example.

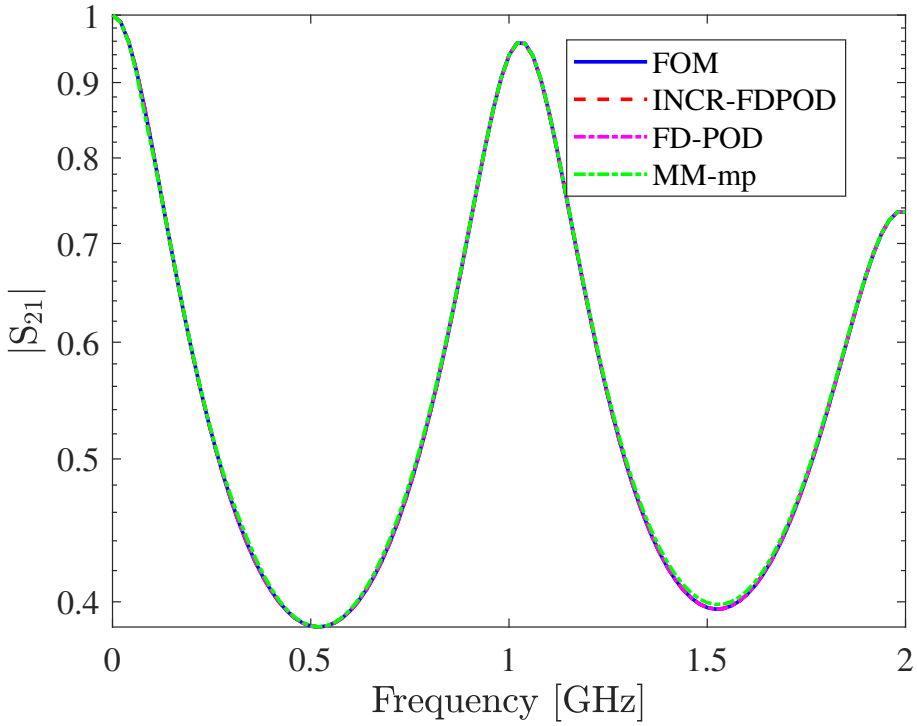


Figure 5.3: Magnitude of S_{21} for the L-shaped conductor over the ground plane example.

To assess the accuracy of both reduced order models, we compare the error of S_{11} and S_{21} for all the ROMs shown in Figs. 5.4-5.5

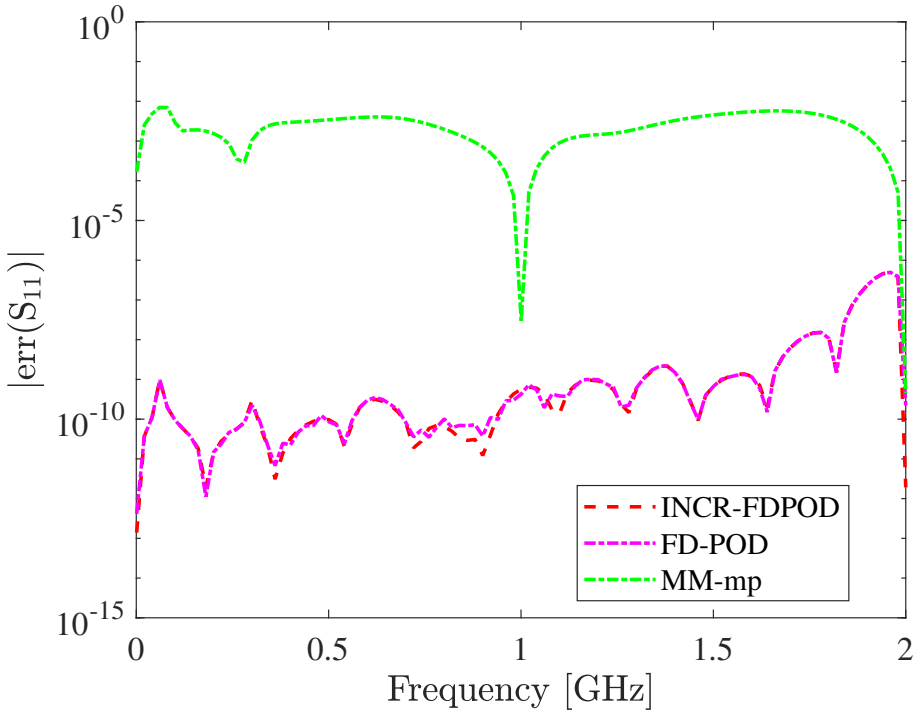


Figure 5.4: Reduced order models error comparison for S_{11} for the L-shaped conductor over the ground plane example.

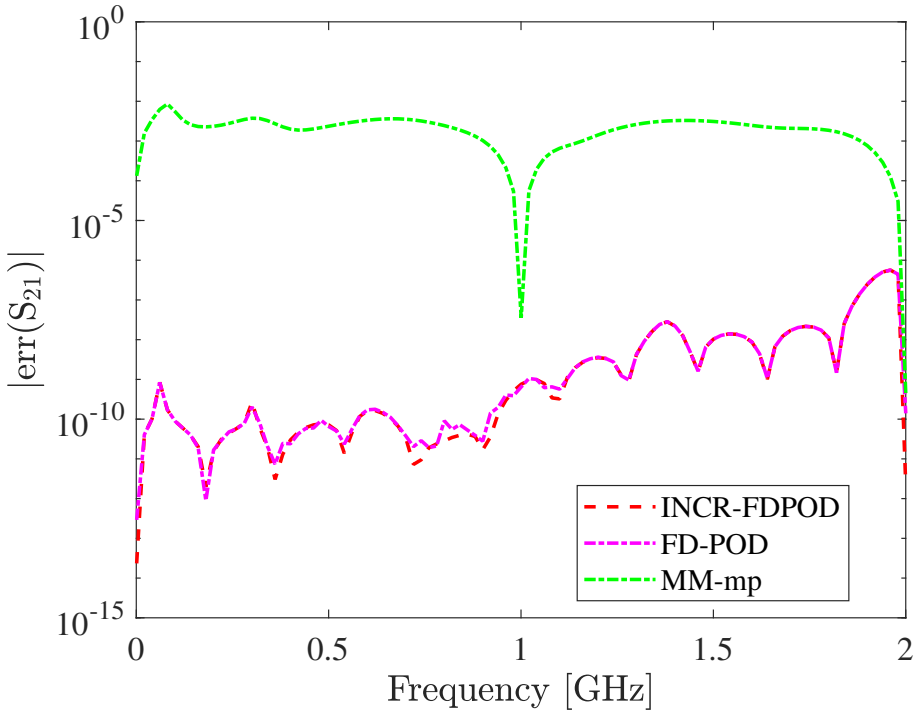


Figure 5.5: Reduced order models error comparison for S_{21} for the L-shaped conductor over the ground plane example.

The errors show that INCR-FDPOD and FD-POD perform better than MM-mp in terms of accuracy. Next, we analyze some time-domain results by exciting the first input with a pseudorandom binary sequence (PRBS) voltage source and comparing the port voltages. The voltage on the first port is depicted in Fig. 5.6.

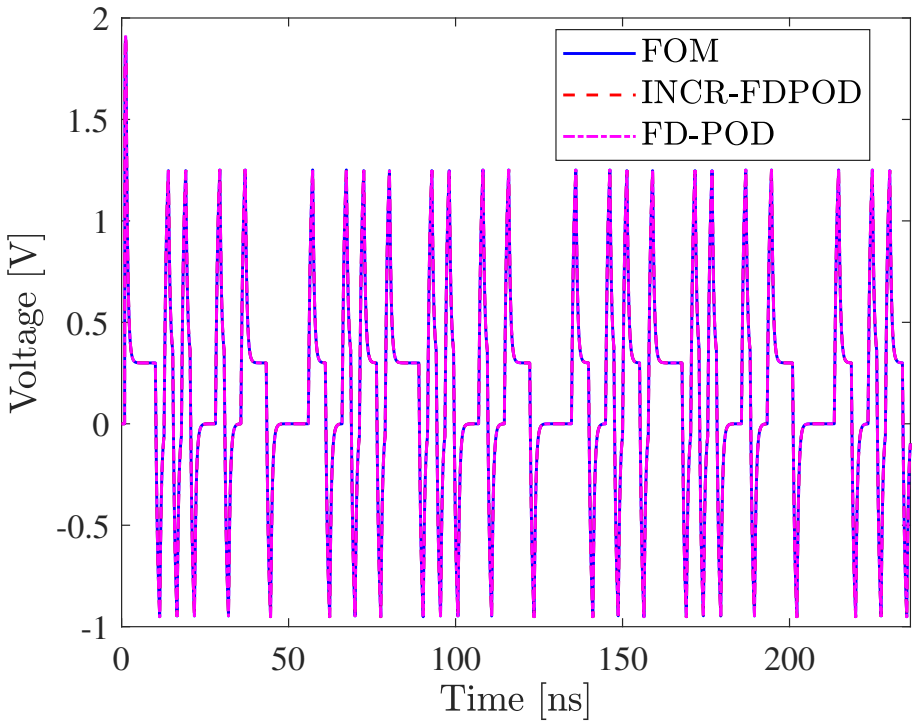


Figure 5.6: Comparison of the first port voltage for the L-shaped conductor over the ground plane example.

Similarly, the voltage of the second port is shown in Fig. 5.7.

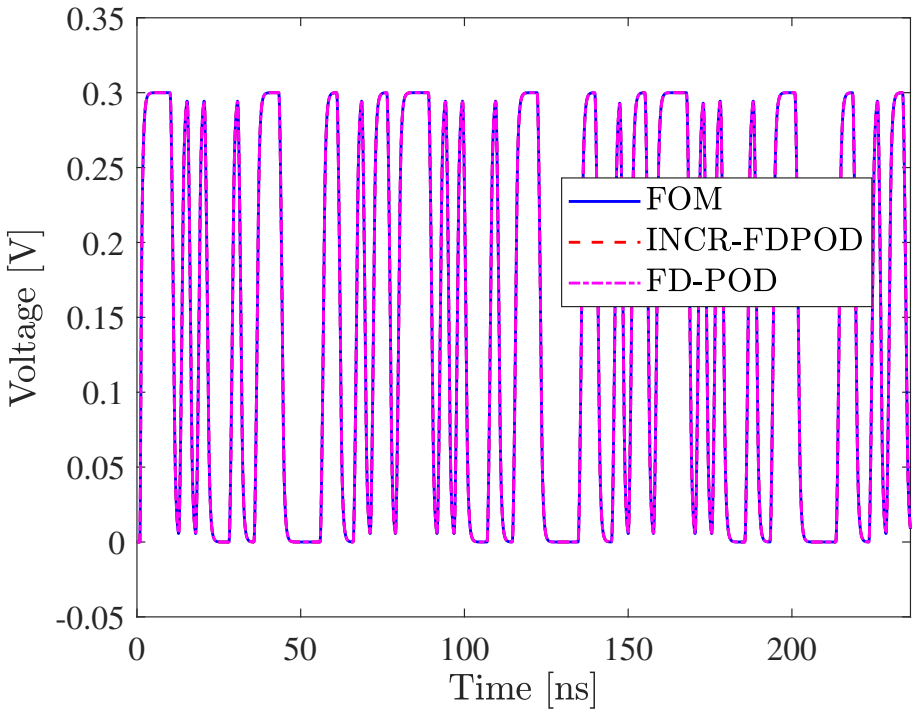


Figure 5.7: Comparison of the second port voltage for the L-shaped conductor over the ground plane example.

It required 2755 s to obtain time-domain results with the FOM, whereas the INCR-FDPOD and FD-POD models achieved this in just 9 s and 8 s, respectively. Notably, the reduced-order models generated using the INCR-FDPOD and FD-POD methods consistently produce accurate and stable time-domain results, unlike the MM-mp-generated model that exhibits instability in the time domain.

5.3.2 Two coplanar microstrips

In this example, the original PEEC model has an order $n = 20080$ with $n_I = 4$ inputs and $n_O = 4$ outputs. There are $n_{\tau_L} = 17$ and $n_{\tau_P} = 17$ delays. The geometry of the system is shown in Fig. 5.8

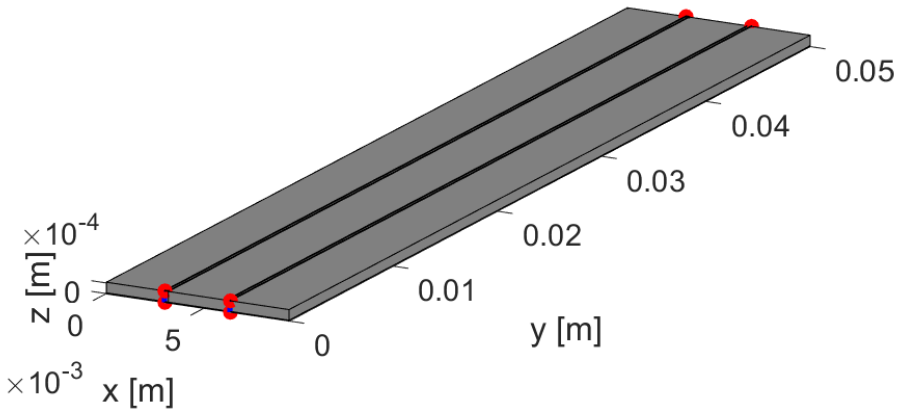


Figure 5.8: Two microstrip interconnection.

Using Algorithm 5.2, we get a POD-based reduced order model of size $r_u = 120$. We use 12 snapshots uniformly distributed in the frequency range [1 MHz, 3 GHz]. The **K** matrix for the INCR-FDPOD method was computed using the INCR-SVD technique, while the FD-POD method utilized the standard one-shot SVD method for this computation. We choose three expansion points for $MM-mp$ [10 Hz, 1 GHz, 3 GHz]. The INCR-FDPOD and FD-POD reduced order models were constructed in 1720 s and 1632 s, respectively, while the construction of the MM-mp reduced order model took 19090 s. As in the previous example, the CPU time comparison related to the construction of the different reduced order models and the size of each reduced model is shown in Table 5.3.

Model	Size	Construction Time (s)
FOM	20080	-
INCR-FDPOD	120	1720
FD-POD	120	1632
MM-mp	120	19090

Table 5.3: Construction time and size of the reduced order models for the two microstrip interconnection example.

Also, we analyze the CPU time needed to evaluate the scattering parameters for a frequency sample by the different models, and we illustrate it in Table 5.4.

Model	Evaluation Time (s)
FOM	104
INCR-FDPOD	$4.497 \cdot 10^{-3}$
FD-POD	$5.764 \cdot 10^{-3}$
MM-mp	$4.457 \cdot 10^{-3}$

Table 5.4: CPU time comparison for a single frequency sample evaluation of the scattering parameters for the two microstrip interconnection example.

To check the precision of the reduced-order models, we examine the responses of the scattering parameters. The magnitude of the scattering parameters S_{11} and S_{21} of the reduced-order models is depicted in Figure 5.9, and this data is compared to the corresponding parameters of the original PEEC model.

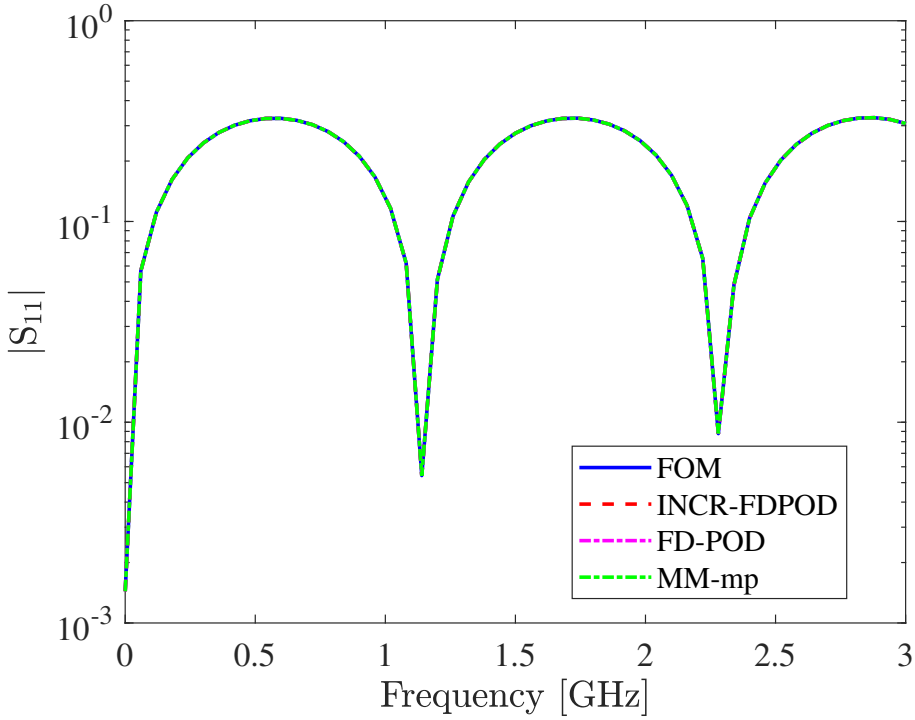


Figure 5.9: Magnitude of S_{11} for the two microstrip interconnection example.

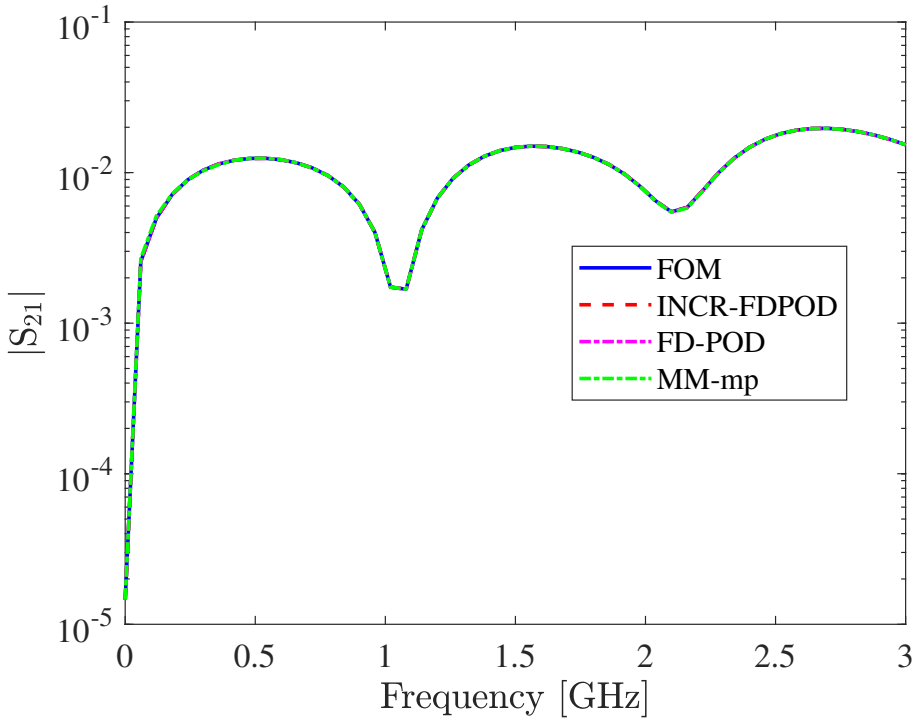


Figure 5.10: Magnitude of S_{21} for the two microstrip interconnection example.

Next, we analyze the magnitude of scattering parameters S_{31} and S_{41} of the original PEEC model and reduced order models, shown in Figs. 5.11-5.12, respectively.

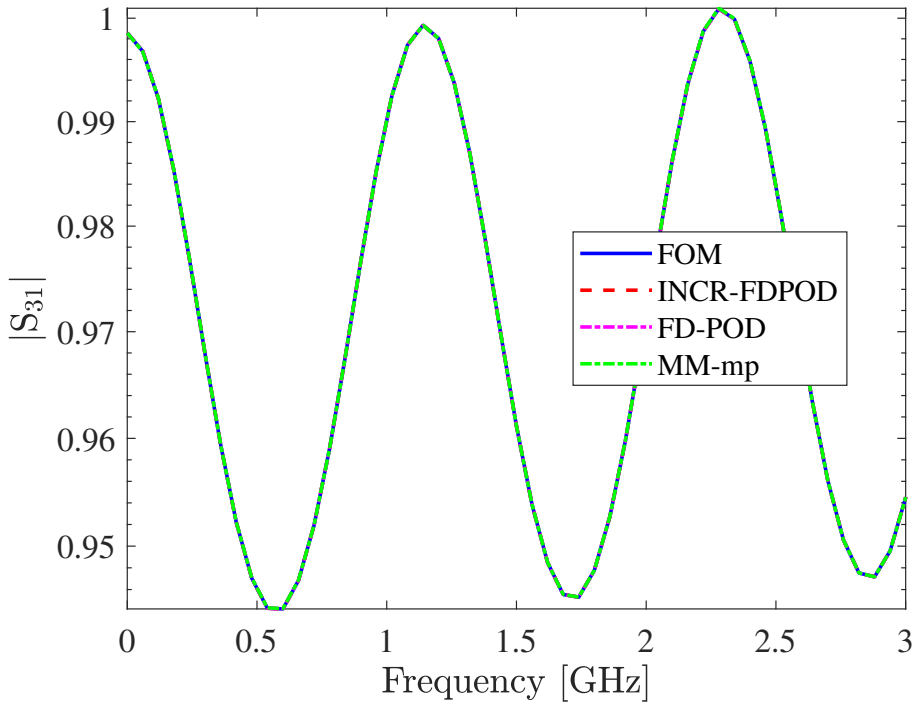


Figure 5.11: Magnitude of S_{31} for the two microstrip interconnection example.

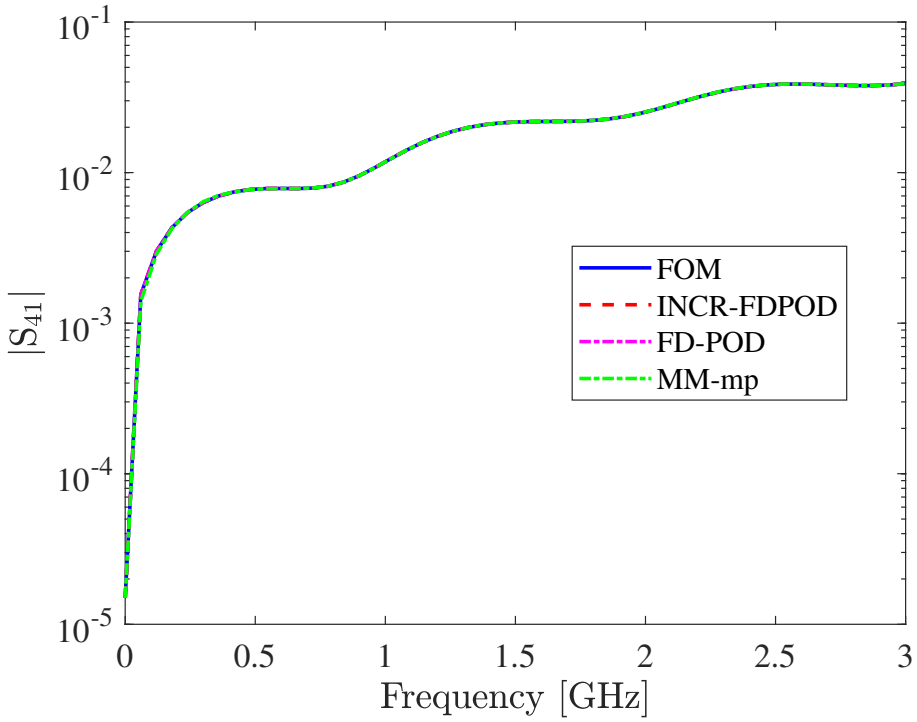


Figure 5.12: Magnitude of S_{41} for the two microstrip interconnection example.

To check the accuracy of both reduced order models, the error analysis for these scattering parameters is plotted in Figs. 5.13-5.16.

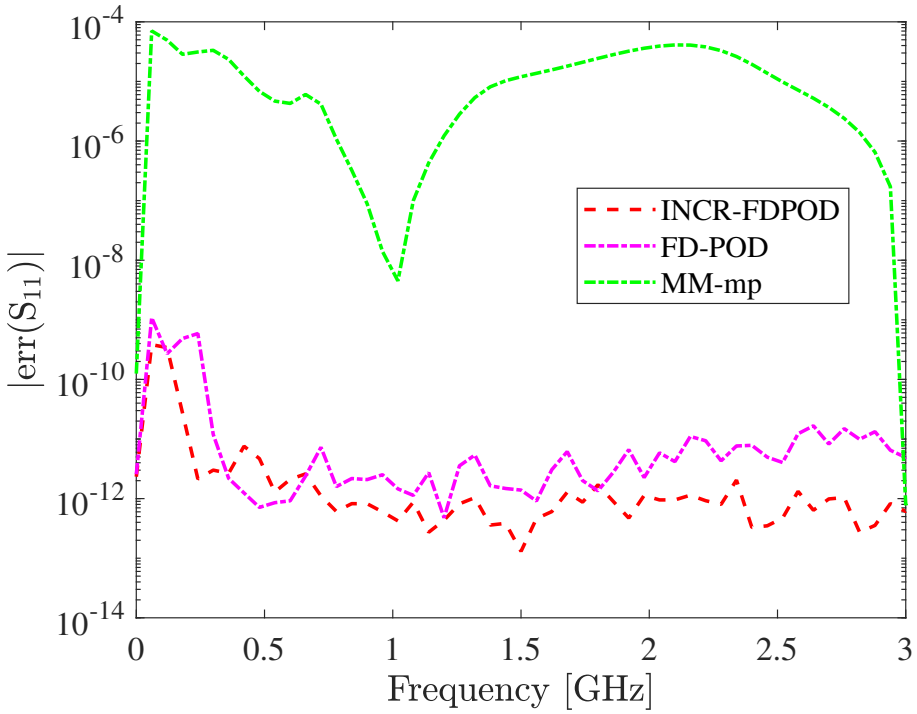


Figure 5.13: Reduced order models error comparison for S_{11} for the two microstrip interconnection example.

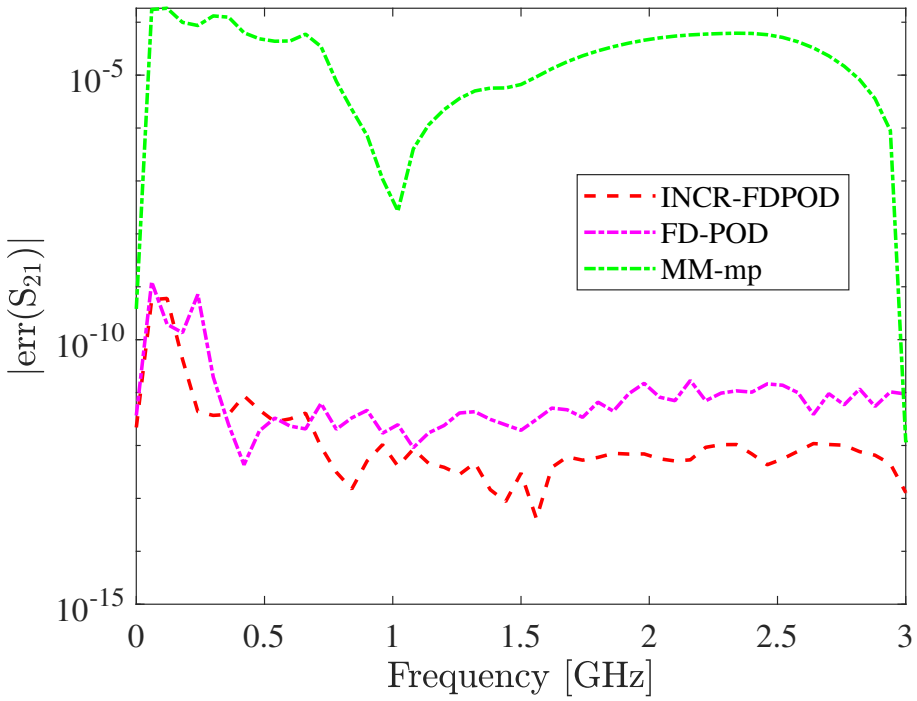


Figure 5.14: Reduced order models error comparison for S_{21} for the two microstrip interconnection example.

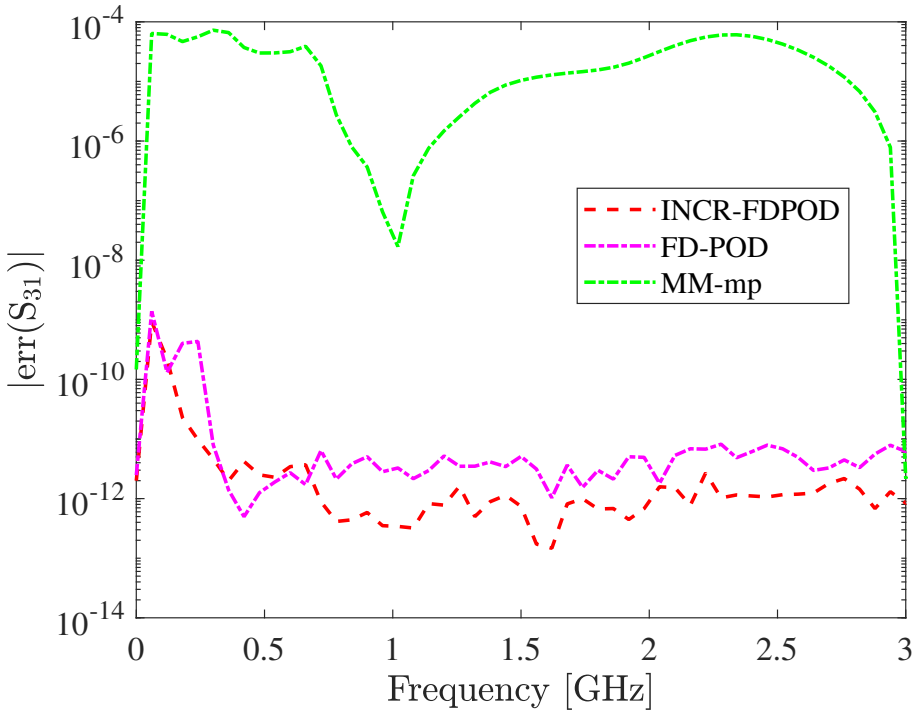


Figure 5.15: Reduced order models error comparison for S_{31} for the two microstrip interconnection example.

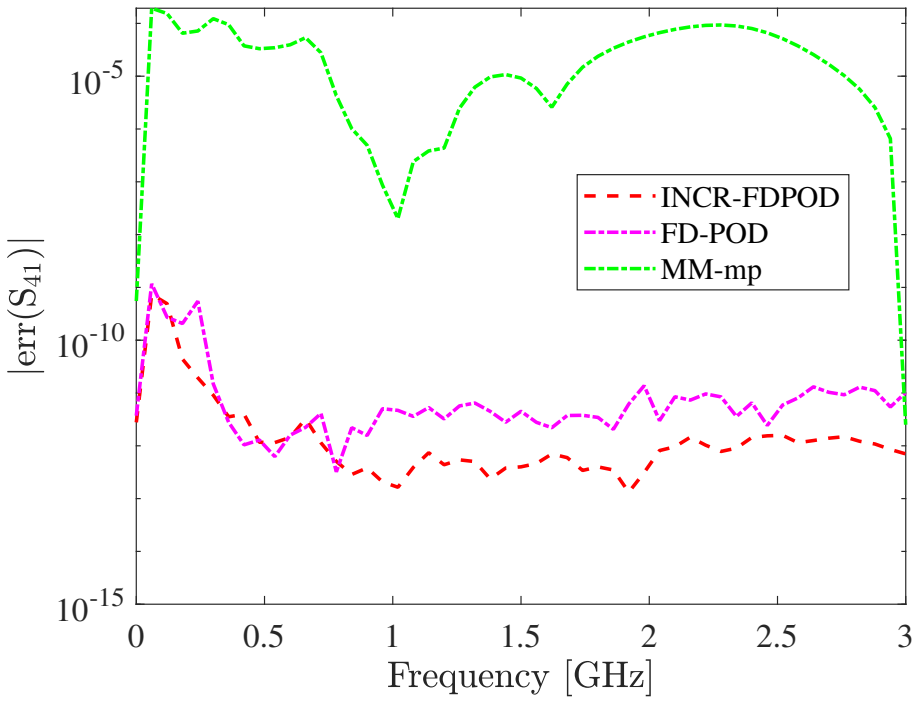


Figure 5.16: Reduced order models error comparison for S_{41} for the two microstrip interconnection example.

INCR-FDPOD and FD-POD outperform MM-mp in terms of accuracy for the same reduced order. Subsequently, we examine the results in the time domain by exciting the first input with a PRBS voltage source. The voltage on the first port is depicted in Fig. 5.17.

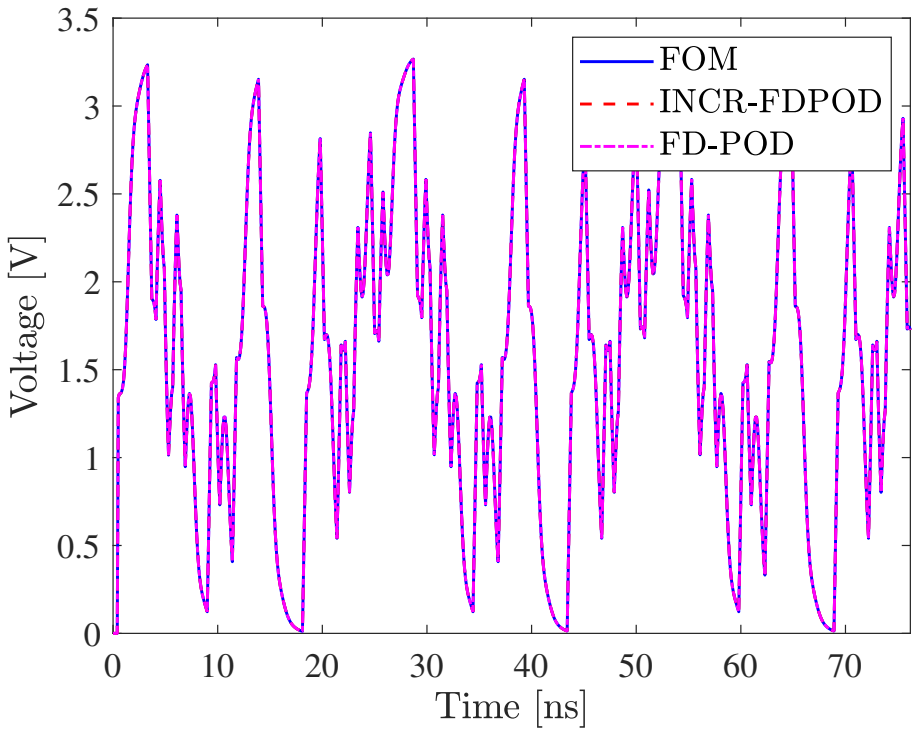


Figure 5.17: Comparison of the input port voltage of the driven line for the two microstrip interconnection example.

The output port voltage of the driven line is shown in Fig. 5.18.

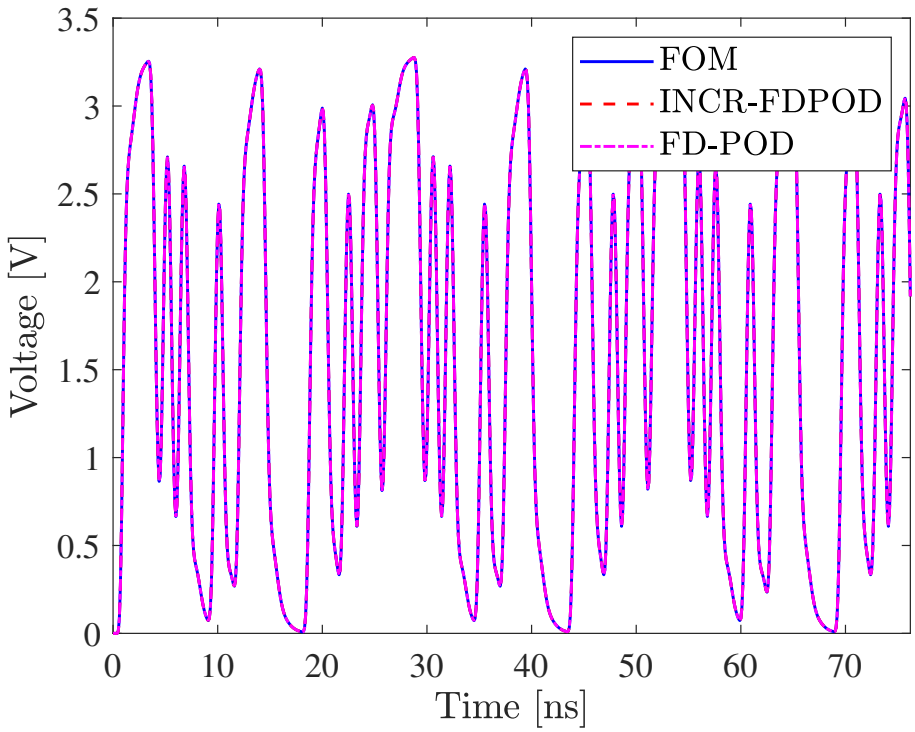


Figure 5.18: Comparison of the output port voltage of the driven line for the two microstrip interconnection example.

The input and output port voltages of the victim line are shown in Figs. 5.19-5.20.

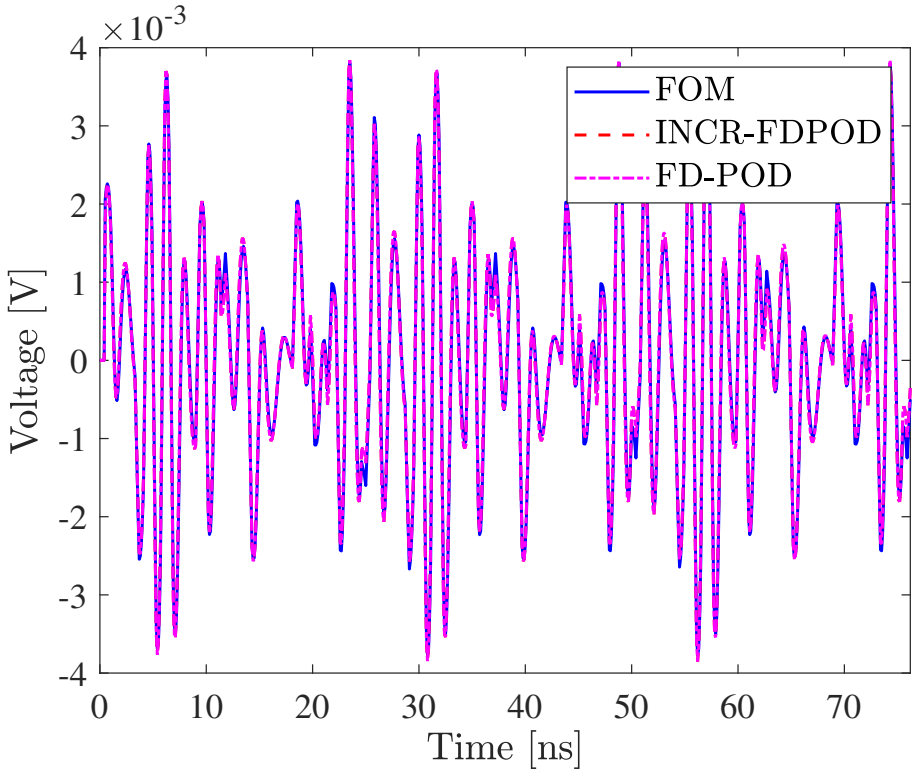


Figure 5.19: Comparison of the input port voltage of the victim line for the two microstrip interconnection example.

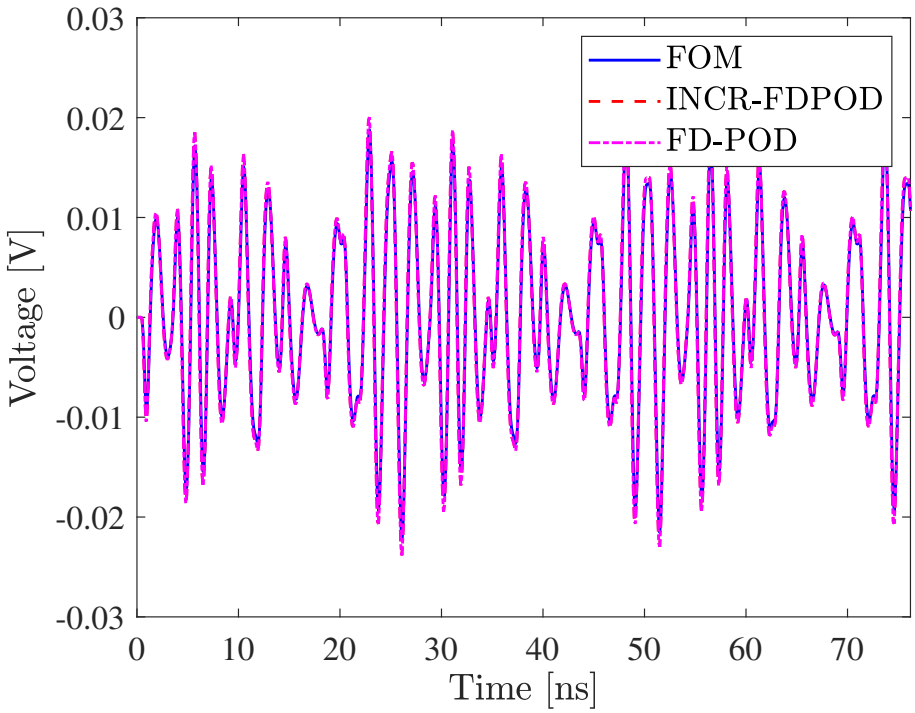


Figure 5.20: Comparison of the output port voltage of the victim line for the two microstrip interconnection example.

The results indicate that INCR-FDPOD and FD-POD exhibit better performance in terms of accuracy. While the time-domain simulations of the FOM require 4092 s, both INCR-FDPOD and FD-POD complete the simulation in only 0.9 s. Furthermore, the MM-mp results in the time domain are unstable.

Chapter 6

Derivatives-enhanced POD-based MOR for delayed PEEC models

This chapter is based on author's published work[1].

Building upon the incremental POD method introduced in the chapter 4, this chapter presents an enhancement that incorporates frequency-domain derivatives into the snapshot collection process. This approach aims to improve the accuracy of reduced-order models while maintaining computational efficiency.
The chapter explains the mathematical foundation of frequency-domain derivatives and how they can be used to refine the snapshot matrix in POD-based MOR. By including derivative information, the resolution of the reduced model is improved, leading to better approximations of the system's frequency response.
A systematic procedure for implementing derivatives-enhanced POD is outlined, including strategy for computing derivatives, integrating them into the snapshot matrix and optimizing computational performance. Numerical case studies are presented to demonstrate the advantages of this approach, showing how it reduces the number of required snapshots while maintaining or even improving model accuracy. The chapter concludes with an analysis of the practical implications of derivatives-enhanced POD and discusses its potential applications for delayed PEEC models.

[1]M. A. Khattak, D. Romano, M. Bandinelli, A. Mori, M. Bercigli, G. Antonini, and F. Ferranti, "Proper Orthogonal Decomposition with Derivatives for Delayed PEEC Models," 4th URSI Atlantic Radio Science Conference (AT-RASC), May 2024.

M. A. Khattak, D. Romano, G. Antonini, and F. Ferranti, "Derivatives-Enhanced Proper Orthogonal Decomposition for PEEC Models With Delays," IEEE Microwave and Wireless Technology Letters, vol. 34, no. 10, pp. 1135-1138, Oct. 2024.

6.1 Proper orthogonal decomposition and frequency-domain derivatives

The representation of the state vector for a delayed PEEC model in the frequency domain is as follows:

$$\mathbf{H}(s) = (s\mathbf{C}(s) + \mathbf{G}(s))^{-1}\mathbf{B}. \tag{6.1}$$

For simplicity, we define $\mathbf{T}(\mathbf{s}) = s\mathbf{C}(s) + \mathbf{G}(s)$ and then we have:

$$\mathbf{H}(s) = \mathbf{T}(s)^{-1}\mathbf{B}. \tag{6.2}$$

To compute the derivative of (6.2) with respect to s, we apply the product rule for matrix derivatives, and we obtain:

$$\frac{\partial \mathbf{H}(s)}{\partial s} = \frac{\partial}{\partial s}\mathbf{T}(s)^{-1} \cdot \mathbf{B} + \mathbf{T}(s)^{-1}\frac{\partial}{\partial s}\mathbf{B}, \tag{6.3}$$

$$= \frac{\partial}{\partial s}\mathbf{T}(s)^{-1} \cdot \mathbf{B}. \tag{6.4}$$

Using the following property [176]

$$\frac{\partial}{\partial s}\mathbf{T}(s)^{-1} = -\mathbf{T}(s)^{-1}\frac{\partial \mathbf{T}(s)}{\partial s}\mathbf{T}(s)^{-1}, \tag{6.5}$$

First, We find the derivative of the $\mathbf{T}(s)$ using

$$\frac{\partial}{\partial s}\mathbf{T}(s) = \frac{\partial}{\partial (s)}[s\mathbf{C}(s) + \mathbf{G}(s)],$$

which becomes

$$\frac{\partial}{\partial s}\mathbf{T}(s) = \frac{\partial}{\partial s}s \cdot \mathbf{C}(s) + \frac{\partial}{\partial s}\mathbf{G}(s).$$

Now, the derivative of the $\mathbf{T}(s)$ is represented as

$$\frac{\partial}{\partial s}\mathbf{T}(s) = \mathbf{C}(s) + s\sum_{k=1}^{n_{\tau_L}}(-\tau_k)\mathbf{C}_k e^{-s\tau_k} + \sum_{k=1}^{n_{\tau_P}}(-\tau_k)\mathbf{G}_k e^{-s\tau_k} \tag{6.6}$$

the derivative of the $\mathbf{H}(s)$ can be expressed as

$$\begin{aligned}\frac{\partial \mathbf{H}(s)}{\partial s} = -\mathbf{T}(s)^{-1}[\mathbf{C}(s) + s\sum_{k=1}^{n_{\tau_L}}(-\tau_k)\mathbf{C}_k e^{-s\tau_k} \\ + \sum_{k=1}^{n_{\tau_P}}(-\tau_k)\mathbf{G}_k e^{-s\tau_k}]\mathbf{T}(s)^{-1} \cdot \mathbf{B}\end{aligned} \tag{6.7}$$

In this chapter, we incorporate the snapshots obtained through Eq. (6.1) and also include the snapshots of the derivatives obtained from Eq. (6.7) which has been published in [177, 178], These snapshots are gathered across a range of frequencies, and the matrices representing the snapshots can be formulated as

$$\mathbf{X}_i = [\Re(\mathbf{H}(s_i)), \Im(\mathbf{H}(s_i))]\,, \tag{6.8}$$

$$\mathbf{XD}_i = \left[\Re(\frac{\partial \mathbf{H}(s_i)}{\partial s}), \Im(\frac{\partial \mathbf{H}(s_i)}{\partial s})\right]. \tag{6.9}$$

We employ Algorithm 6.1 for the construction of the orthonormal basis $\mathbf{K} \in \Re^{n_u \times n_r}$ which is essential for building the reduced-order model in Eq. (4.11). This algorithm

Algorithm 6.1: POD-Based MOR technique

Data: $\mathbf{C}$, $\mathbf{G}$, $\mathbf{B}$
Result: $\mathbf{K}$
Initialization: Set $i = 1$, $\mathbf{X} = []$, r = number of snapshots ;
while $i \leq r$ **do**
    Consider the frequency sample s_i ;
    Collect snapshots $\mathbf{X}_{ss} = [\mathbf{X}_i, \mathbf{XD}_i]$ % use Eq. (6.8) & Eq. (6.9) ;
    Concatenate all the snapshots: $\mathbf{X} = [\mathbf{X}, \mathbf{X}_{ss}]$;
    $i = i + 1$;
Compute Singular Value Decomposition (SVD): $\mathbf{KSU}^T = \text{SVD}(\mathbf{X})$;
Choose $\mathbf{K} = \mathbf{U}$.

is used to obtain the orthonormal basis for generating the reduced-order model described in (4.11). Concerning time-domain simulations of delayed PEEC models, assuming a uniform time step, NDDEs in Eq. (4.11) can be integrated using one or two-step integration methods [160, 161].

6.2 Numerical results

All the tests were performed with MATLAB R2023b [179] on a Microsoft Windows Server 2019 platform having Intel (R) Xeon (R) W-1290 CPU @ 3.20GHz, 3192 MHz, 10 core(s), 20 logical processors and 128 GB RAM.

6.2.1 L-shaped conductor example

The proposed MOR approach has been tested on the L-shaped conductor over a ground plane illustrated in Fig. 6.1. The conductors are assumed to be copper.

The original model has $n_u = 9707$ degrees of freedom, $n_I = 2$ inputs and $n_O = 2$ outputs. We apply Algorithm 6.1 and obtain a reduced-order model with a size of $n_r = 96$. A set of 12 response snapshots evenly distributed across the frequency range of [1 MHz, 2 GHz] and the corresponding derivatives snapshots have been used. We build a reduced order model (called FD-POD) using only the response snapshots and a reduced order model (called FDPOD-D) using the response and derivatives snapshots. There are $n_{\tau_L} = 294$ and $n_{\tau_P} = 297$ delays for the magnetic and electric field couplings, respectively.

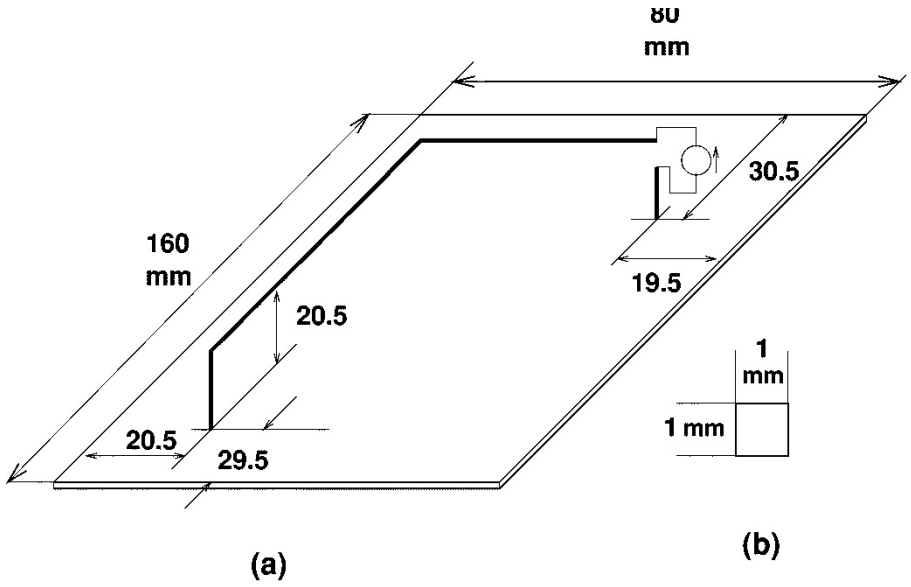


Figure 6.1: Geometry of the L-shaped conductor over a ground plane.

We first analyze the magnitude of the S_{21} scattering parameter as shown in Fig. 6.2.

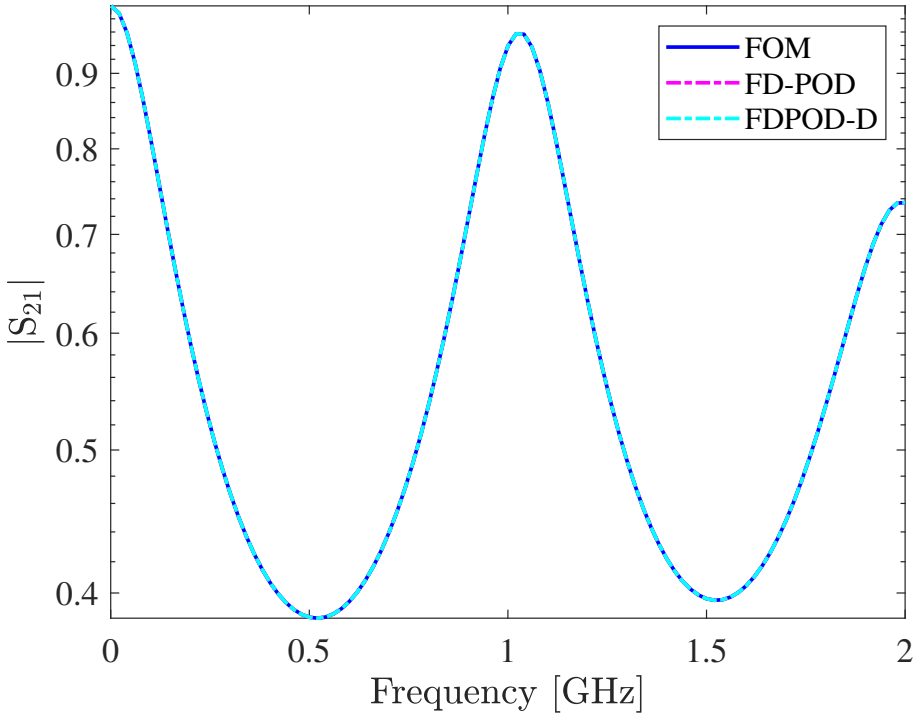


Figure 6.2: Magnitude of S_{21} for the L-shaped conductor over the ground plane.

Next, we check the error to assess the accuracy of the reduced models. The absolute errors are shown in Fig. 6.3.

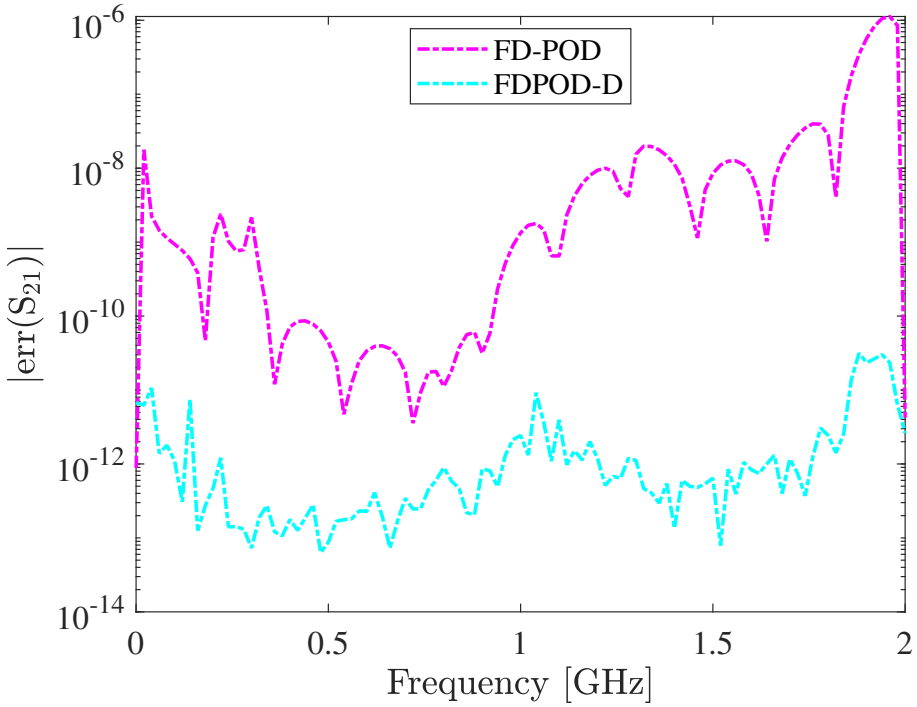


Figure 6.3: Absolute error for S_{21} for the L-shaped conductor over the ground plane.

Similar results can be obtained for S_{11}. We also check the efficiency of the proposed methodology by comparing the CPU time taken to construct the reduced order models, shown in Table 6.1.

Table 6.1: Reduced order model construction time.

Model	Size	Construction Time (s)
FOM	9707	-
FD-POD	48	567
FDPOD-D	96	679

A higher accuracy can be achieved without additional frequency-domain response snapshots by using the derivatives snapshots. Since the snapshots of derivatives are less computationally expensive than the response-based ones, a computational gain is achieved regarding the computational cost to generate a reduced-order model.

6.2.2 Two microstrip interconnection

The MOR methods were applied to a two-microstrip interconnection, as shown in Fig. 6.4.

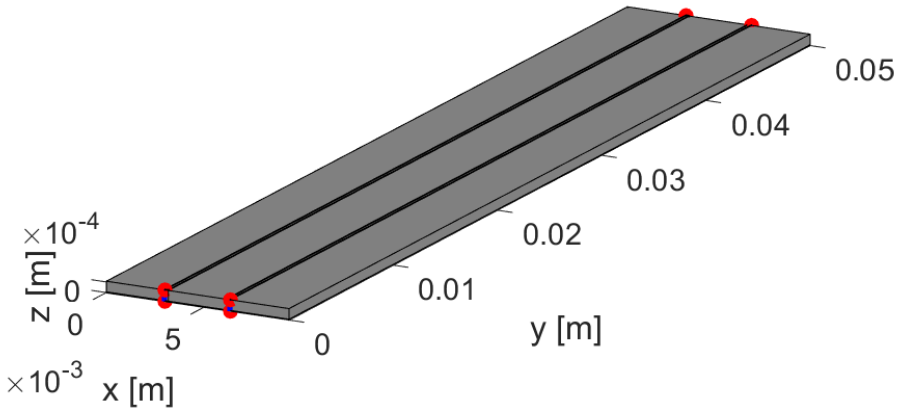


Figure 6.4: Geometry of the two microstrip interconnection.

The original model has $n_u = 20080$ state variables, $n_I = 4$ inputs, and $n_O = 4$ outputs. Utilizing Algorithm 6.1 produces a reduced-order model with $n_r = 96$. 6 frequency-domain response snapshots, evenly distributed from 1 MHz to 2 GHz, and their corresponding derivatives were used to construct the $\mathbf{K}$ matrix. Two reduced-order models were developed: FD-POD, using only response snapshots, and FDPOD-D, incorporating both response and derivative snapshots. The delay numbers are $n_{\tau_L} = 17$ and $n_{\tau_P} = 17$.
First, we show the model results and errors related to the magnitude of the S_{11} scattering parameter. Fig. 6.5 illustrates the models' prediction and the absolute errors.

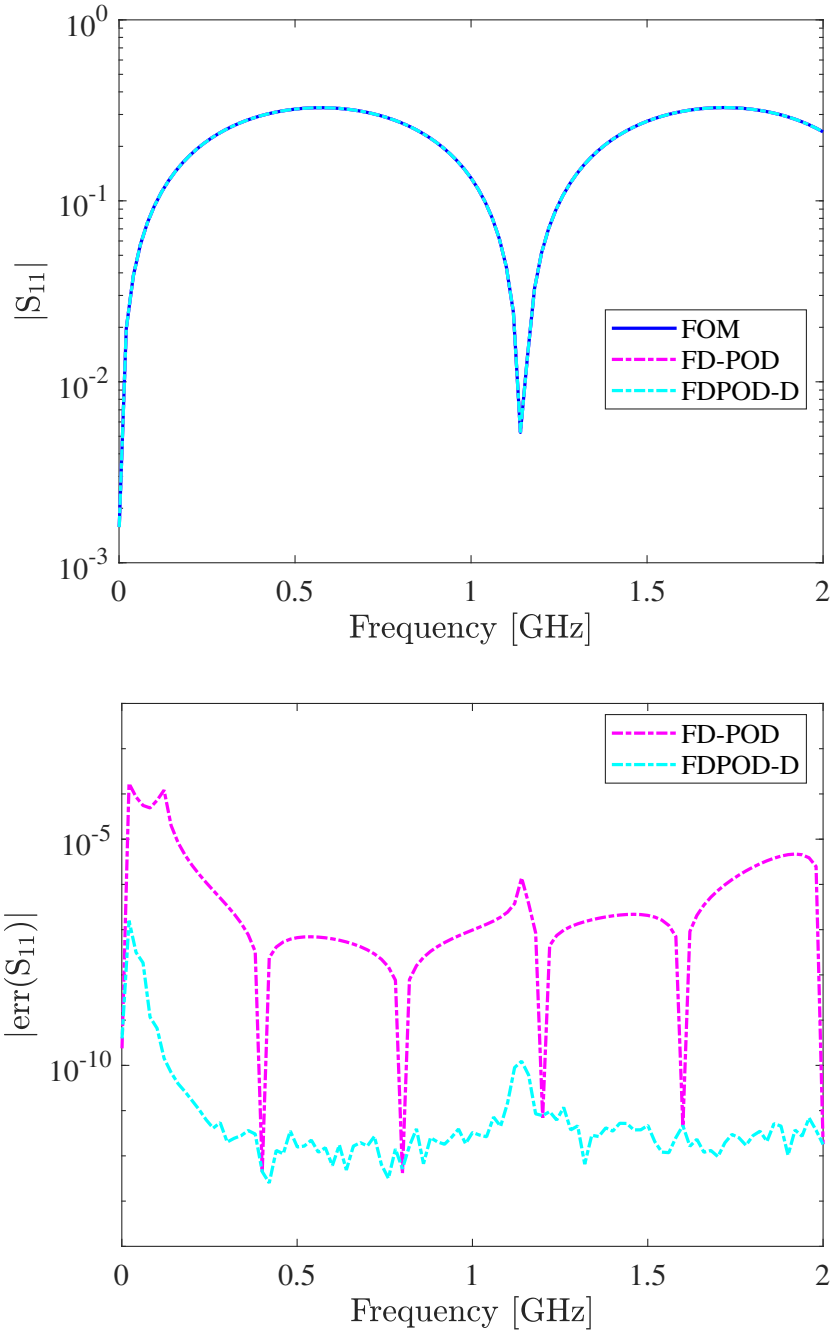


Figure 6.5: Magnitude of S_{11} (top). absolute error for S_{11} (bottom).

Likewise, a similar trend can be observed for S_{21}, S_{31}, S_{41} and all other entries of the scattering parameter matrix [180]. A set of 101 frequency samples is used for

these results. The maximum error for all 16 terms of the scattering matrix over the 101 frequency samples is equal to -97 dB for FD-POD and -173 dB for FDPOD-D. Additionally, we assess the efficiency of the proposed MOR methodology by comparing the CPU time needed to build the reduced-order models and to evaluate each model over 101 frequency samples, as shown in Table 6.2.

Model	Size	Construction Time (s)	Prediction Time (s)
FOM	20080	-	12041
FD-POD	48	562	0.0450
FDPOD-D	96	607	0.0960

Table 6.2: Reduced order model construction time.

The memory occupied by the matrices of the original and reduced order models is: 752 MB (original model), 617 KB (FD-POD model), 2455 KB (FDPOD-D model). We also check the results in time domain by exciting the first port using a sinusoidally modulated Gaussian pulse $Ve^{-0.5\left(\frac{t-t_d}{\sigma}\right)^2}\sin(2\pi ft)$ with $V = 1$ V, $t_d = 0.9$ ns, $f = 1.5$ GHz, $\sigma = 5 \times 10^{-10}$ s and a series resistor with value 50 Ω. All the other ports are terminated on 50 Ω. We evaluate the relative error by using $\left|\frac{original\ \ output - reduced\ \ output}{original\ \ output}\right|$. The models' prediction and the relative errors considering the far-end port are shown in Fig. 6.6.

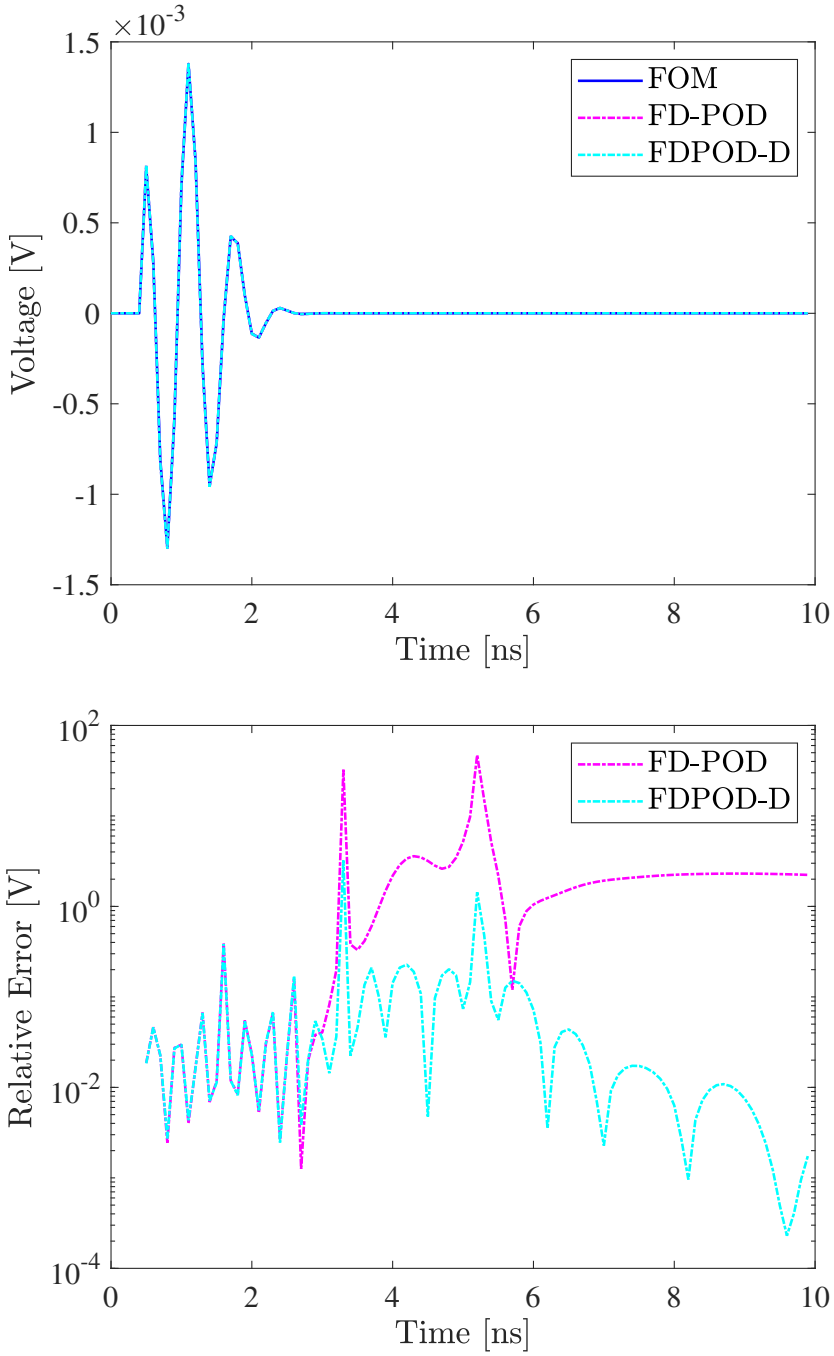


Figure 6.6: Models prediction and relative errors for the voltage at port 4 (far-end port).

We noticed that time-domain results for the given numerical example are accurate,

and better accuracy was achieved by including derivative snapshots. Since snapshots of derivatives have a lower computational cost than response-based snapshots, a computational advantage is evident in the overall cost of generating a reduced-order model. At the same time, the reduced order model built by including derivative snapshots is also very accurate in both the frequency domain and time domain.

Chapter 7

Conclusions and future work

7.1 Summary of contributions

This PhD thesis focused on the development and application of advanced model order reduction (MOR) techniques for delayed partial element equivalent circuit (PEEC) models. The primary objective was to reduce the computational burden associated with the simulation of large-scale electromagnetic (EM) systems modeled using neutral delay differential equations (NDDEs). The key contributions of this work can be summarized as follows:

7.1.1 Proper orthogonal decomposition-based model order reduction

Initially, we proposed the application of proper orthogonal decomposition (POD) in the frequency-domain as a MOR technique for delayed PEEC models. The method involved collecting snapshots of the transfer function and then performing a singular value decomposition (SVD) step to extract a low-dimensional representation. The reduced-order models (ROMs) obtained through this approach demonstrated a significant reduction in computational cost while maintaining accuracy in both frequency and time-domain simulations. A major challenge with standard POD is the computational cost associated with performing a large-scale SVD. To address this, an incremental POD technique in the frequency-domain was explored and investigated. Instead of computing the SVD over a single large snapshot matrix, incremental POD updates the reduced basis iteratively as new snapshots are added. This approach reduces memory requirements and computational complexity while maintaining high accuracy.

7.1.2 Derivative-enhanced proper orthogonal decomposition

To further enhance the accuracy and efficiency of POD-based reduction, we introduced a novel approach incorporating derivative information into the snapshot collection process. By considering frequency-domain derivatives of the transfer function, we improved the quality of the reduced basis while reducing the number of required snapshots. This enhancement not only increased the robustness of the MOR process but also led to more accurate ROMs for delayed PEEC systems.

7.1.3 Comparison with multipoint moment matching

A detailed comparison between the developed POD-based techniques and an existing multipoint moment matching (MM-mp) MOR approach was conducted. While MM-mp effectively captures the system behavior around selected expansion points, it often requires careful selection of these expansion points for optimal performance. Our results demonstrated that POD-based methods, particularly the derivative-enhanced variant, offer greater flexibility and improved accuracy across a broader frequency range.

7.2 Future work

While this work has made substantial progress in MOR for delayed PEEC models, several aspects remain open for further research and development.

7.2.1 Optimal selection of snapshots

One of the key challenges in POD-based MOR is the selection of snapshots. An adaptive approach for optimal snapshot selection could further enhance the efficiency of the the ROMs generation and use. An adaptive sampling techniques and error-based criteria to determine the most informative snapshots dynamically can be of high interest.

7.2.2 Higher derivative snapshots incorporation

Extending the derivative-enhanced POD approach by incorporating higher-order derivatives of the transfer function could provide additional accuracy improvements. This enhancement could allow for even better capturing of system dynamics, especially in highly frequency-sensitive models.

7.2.3 Extension to nonlinear systems

This work primarily focused on linear state-space representation of delayed PEEC models. Extending these techniques to nonlinear PEEC models could significantly enhance the applicability of ROM in complex electromagnetic systems. Developing MOR techniques that effectively handle nonlinearities would enable accurate and efficient simulations for a broader range of practical applications.

7.2.4 Parameterized model order reduction

Another interesting direction is the extension of the proposed methods to parameterized model order reduction (PMOR). This involves incorporating design parameters into the reduction framework, allowing the generation of ROMs that are valid over a range of design configurations. However, dealing with the curse of dimensionality that arises from the inclusion of multiple parameters remains a challenge and requires efficient strategies.

7.2.5 Error estimators and bounds for ROMs

An investigation of efficient error estimators and error bounds for ROMs is an essential future direction. Having efficiently estimated error values and theoretical error bounds on the accuracy of ROMs is important for their applicability for engineering designs and simulations and use by practitioners and designers.

7.3 Final remarks

This research has contributed to advancing MOR techniques for delayed PEEC models by developing and validating POD-based MOR approaches. The proposed methods offer robust and efficient ways of reducing the computational complexity of electromagnetic simulations while preserving accuracy. The insights gained from this study pave the way for future advancements in MOR, with promising directions in many directions. These developments will further enhance the applicability of MOR modeling in electromagnetics and engineering design.

Appendix A

List of publications

Articles in scientific journals with an international referee system

1. **M. A. Khattak**, D. Romano, G. Antonini, and F. Ferranti, "Efficient Frequency and Time-Domain Simulations of Delayed PEEC Models With Proper Orthogonal Decomposition Techniques," *IEEE Access*, vol. 12, pp. 168-178, December 2023.

2. **M. A. Khattak**, D. Romano, G. Antonini, and F. Ferranti, "Derivatives-Enhanced Proper Orthogonal Decomposition for PEEC Models with Delays," *IEEE Microwave and Wireless Components Letters*, vol. 34, no. 3, pp. 123-126, March 2024.

International conference papers

1. **M. A. Khattak**, D. Romano, G. Antonini, and F. Ferranti, "Proper Orthogonal Decomposition-Based Model Order Reduction of Delayed PEEC Models," *2023 International Conference on Electromagnetics in Advanced Applications (ICEAA)*, pp. 554-558, Venice, Italy, October 2023.

Invited contribution for a special session. Conference abstract.

1. **M. A. Khattak**, D. Romano, M. Bandinelli, A. Mori, M. Bercigli, G. Antonini, and F. Ferranti, "Proper Orthogonal Decomposition with Derivatives

for Delayed PEEC Models," *4th URSI Atlantic Radio Science (ATRASC)*, Gran Canaria, Spain, May 2024.

Bibliography

[1] G. Antonini. The partial element equivalent circuit method for EMI, EMC, and SI analysis. *ACES Newsletter*, 21(1):8–32, 2006.

[2] G Antonini, G Miscione, and Jonas Ekman. PEEC modeling of automotive electromagnetic problems. *Applied Computational Electromagnetics Society Newsletter*, 23(1):39–50, 2008.

[3] A.E. Ruehli, G. Antonini, and L. Jiang. *Circuit oriented electromagnetic modeling using the PEEC techniques*. John Wiley & Sons, 2017.

[4] A. E. Ruehli. Inductance calculations in a complex integrated circuit environment. *IBM Journal of Research and Development*, 16(5):470–481, Sept 1972.

[5] A. E. Ruehli and P. A. Brennan. Efficient capacitance calculations for three-dimensional multiconductor systems. *IEEE Transactions on Microwave Theory and Techniques*, 21(2):76–82, Feb 1973.

[6] A. E. Ruehli. Equivalent circuit models for 3-D multiconductor systems. *IEEE Transactions on Microwave Theory and Techniques*, 22(3):216–221, Mar 1974.

[7] A. E. Ruehli and H. Heeb. Circuit models for three-dimensional geometries including dielectrics. *IEEE Transactions on Microwave Theory and Techniques*, 40(7):1507–1516, Jul 1992.

[8] G. Antonini, A. E. Ruehli, and C. Yang. PEEC modeling of dispersive and lossy dielectrics. *IEEE Transactions on Advanced Packaging*, 31(4):768–782, Nov 2008.

[9] D. Romano and G. Antonini. Quasi-static partial element equivalent circuit models of linear magnetic materials. *IEEE Transactions on Magnetics*, 51(7):1–15, July 2015.

[10] D. Romano and G. Antonini. Augmented quasi-static partial element equivalent circuit models for transient analysis of lossy and dispersive magnetic materials. *IEEE Transactions on Magnetics*, 52(5):1–11, May 2016.

[11] D. Romano, G. Antonini, and A. E. Ruehli. Time-domain partial element equivalent circuit solver including non-linear magnetic materials. *IEEE Transactions on Magnetics*, 52(9):1–11, September 2016.

[12] D. Romano and G. Antonini. Quasi-static partial element equivalent circuit models of magneto-dielectric materials. *IET Microwaves, Antennas Propagation*, 11(6):915–922, 2017.

[13] D. Romano, G. Antonini, and A. E. Ruehli. Time-domain partial element equivalent circuit solver including non-linear magnetic materials. In *2015 IEEE MTT-S International Conference on Numerical Electromagnetic and Multiphysics Modeling and Optimization (NEMO)*, pages 1–3, August 2015.

[14] J. Ekman. *Electromagnetic modeling using the partial element equivalent circuit method*. PhD thesis, Luleå tekniska universitet, 2003.

[15] M. Enohnyaket. *PEEC modeling and verification for broadband analysis of air-core reactors*. PhD thesis, Luleå tekniska universitet, 2007.

[16] A. E. Ruehli. *The Method of Partial Element Equivalent Circuits (PEEC Method)*, chapter 4, pages 179–260. John Wiley & Sons, Ltd, 2009.

[17] R. Torchio. *Extending the unstructured PEEC method to magnetic, transient, and stochastic electromagnetic problems*. PhD thesis, Université Grenoble Alpes; Università degli studi (Padoue, Italie), 2019.

[18] R. F. Harrington. *Field Computation by Moment Methods*. Macmillan, New York, 1968.

[19] C. A. Balanis. *Advanced Engineering Electromagnetics*. WILEY, 1989.

[20] L. W. Nagel. SPICE: A computer program to simulate semiconductor circuits. Electr. Res. Lab. Report ERL M520, University of California, Berkeley, May 1975.

[21] A. E. Ruehli and A. C. Cangellaris. Progress in the methodologies for the electrical modeling of interconnects and electronic packages. *Proceedings of the IEEE*, 89(5):740–771, May 2001.

[22] W. Pinello, A. C. Cangellaris, and A. Ruehli. Hybrid electromagnetic modeling of noise interactions in packaged electronics based on the partial-element equivalent-circuit formulation. *IEEE Transactions on Microwave Theory and Techniques*, 45(10):1889–1896, Oct 1997.

[23] C. Wollenberg and A. Gurisch. Analysis of 3-D interconnect structures with PEEC using SPICE. *IEEE Transactions on Electromagnetic Compatibility*, 41(4):412–417, Nov 1999.

[24] G. Antonini and A. Orlandi. A wavelet-based time-domain solution for PEEC circuits. *IEEE Transactions on Circuits and Systems I: Fundamental Theory and Applications*, 47(11):1634–1639, Nov 2000.

[25] A. E. Ruehli, G. Antonini, J. Esch, J. Ekman, A. Mayo, and A. Orlandi. Nonorthogonal PEEC formulation for time- and frequency-domain EM and circuit modeling. *IEEE Transactions on Electromagnetic Compatibility*, 45(2):167–176, May 2003.

[26] G. Antonini, D. Frigioni, and G. Miscione. Hybrid formulation of the equation systems of the 3-D PEEC model based on graph algorithms. *IEEE Transactions on Circuits and Systems I: Regular Papers*, 57(1):249–261, Jan 2010.

[27] L. Lombardi, D. Romano, and G. Antonini. Partial element equivalent circuit method modeling of silicon interconnects. *IEEE Transactions on Microwave Theory and Techniques*, 65(12):4794–4801, December 2017.

[28] M. Bandinelli, A. Mori, M. Bercigli, D. Romano, and G. Antonini. A surface PEEC formulation for the analysis of electrical networks in airplanes. In *2013 IEEE International Symposium on Electromagnetic Compatibility*, pages 694–700, August 2013.

[29] T. Vali, G. Marotta, L. De Santis, G. Antonini, D. Romano, and G. De Luca. Full-wave modeling of inductive coupling links for low-power 3D system integration. In *2013 IEEE International Symposium on Electromagnetic Compatibility*, pages 17–21, August 2013.

[30] G. Antonini, A. E. Ruehli, D. Romano, and L. Jiang. Tests for time domain EM solvers for stability and towards passivity. In *2013 IEEE 22nd Conference on Electrical Performance of Electronic Packaging and Systems*, pages 263–266, October 2013.

[31] P. Belforte, L. Lombardi, D. Romano, and G. Antonini. Digital wave formulation of quasi-static partial element equivalent circuit method. In *2016 IEEE 20th Workshop on Signal and Power Integrity (SPI)*, pages 1–4, May 2016.

[32] A. Hartman, J. Ekman, G. Antonini, and D. Romano. A descriptor form implementation of PEEC models incorporating dispersive and lossy dielectrics. In *2016 IEEE International Symposium on Electromagnetic Compatibility (EMC)*, pages 206–211, July 2016.

[33] G. Antonini. The fast multipole method for PEEC circuits analysis. In *2002 IEEE International Symposium on Electromagnetic Compatibility*, volume 1, pages 446–451 vol.1, Aug 2002.

[34] M. Bebendorf. Approximation of boundary element matrices. *Numer. Math.*, 86:565–589, Jun 2000.

[35] G. Antonini and D. Romano. Adaptive-cross-approximation-based acceleration of transient analysis of quasi-static partial element equivalent circuits. *IET Microwaves, Antennas Propagation*, 9(7):700–709, 2015.

[36] G. Antonini and D. Romano. Multiscale decomposition based analysis of PEEC models. In *2013 International Conference on Electromagnetics in Advanced Applications (ICEAA)*, pages 1095–1098, September 2013.

[37] G. Antonini and D. Romano. Efficient frequency-domain analysis of PEEC circuits through multiscale compressed decomposition. *IEEE Transactions on Electromagnetic Compatibility*, 56(2):454–465, April 2014.

[38] G. Antonini and D. Romano. Acceleration of time-domain nodal-analysis of partial element equivalent circuits through multiscale compressed decomposition. *IEEE Transactions on Electromagnetic Compatibility*, 56(4):970–979, August 2014.

[39] G. Antonini and D. Romano. A vectorized multiscale compressed decomposition-based solver for partial element equivalent circuit method. *International Journal of Numerical Modelling: Electronic Networks, Devices and Fields*, 28(4):419–432, 2015.

[40] F. Ferranti, G. Antonini, T. Dhaene, and L. Knockaert. Guaranteed passive parameterized model order reduction of the partial element equivalent circuit (PEEC) method. *IEEE Transactions on Electromagnetic Compatibility*, 52(4):974–984, Nov 2010.

[41] F. Ferranti, G. Antonini, T. Dhaene, L. Knockaert, and A. E. Ruehli. Physics-based passivity-preserving parameterized model order reduction for PEEC circuit analysis. *IEEE Transactions on Components, Packaging and Manufacturing Technology*, 1(3):399–409, Mar 2011.

[42] F. Ferranti, M.S. Nakhla, G. Antonini, T. Dhaene, L. Knockaert, and A.E. Ruehli. Multipoint full-wave model order reduction for delayed PEEC models with large delays. *IEEE Transactions on Electromagnetic Compatibility*, 53(4):959–967, Nov 2011.

[43] E.R. Samuel, F. Ferranti, L. Knockaert, and T. Dhaene. Passivity-preserving parameterized model order reduction using singular values and matrix interpolation. *IEEE Transactions on Components, Packaging and Manufacturing Technology*, 3(6):1028–1037, 2013.

[44] Y. Dou and K. L. Wu. Direct mesh-based model order reduction of PEEC model for quasi-static circuit problems. *IEEE Transactions on Microwave Theory and Techniques*, 64(8):2409–2422, Aug 2016.

[45] M. D. Lauretis, J. Ekman, G. Antonini, and D. Romano. Enhanced delay-rational Green's method for cable time domain analysis. In *2015 International Conference on Electromagnetics in Advanced Applications (ICEAA)*, pages 1228–1231, September 2015.

[46] D. Romano and G. Antonini. Partitioned model order reduction of partial element equivalent circuit models. *IEEE Transactions on Components, Packaging and Manufacturing Technology*, 4(9):1503–1514, September 2014.

[47] D. Romano, G. Antonini, D. Daroui, and J. Ekman. A fast sparse reluctance- and capacitance-based solver for the partial element equivalent circuit method. *IEEE Transactions on Electromagnetic Compatibility*, 56(5):1077–1086, October 2014.

[48] A. Mori, M. Bandinelli, G. Sammarone, J.P. Parmantier, S. Bertuol, I. Junqua, F. Vipiana, M. A. Echeverri Bautista, G. Antonini, D. Romano, J. Genoulaz, and T. Lebreton. The ARROW project. modelling of lightning indirect effects on composite aircraft equipped with current return networks. In *Proceedings of Amerem*, New Mexico (USA), July 2013.

[49] M. Bandinelli, A. Mori, G. Antonini, D. Romano, and G. M. Sammarone. Numerical analysis of avionic grounding structures with surface PEEC formulation. In *2015 9th European Conference on Antennas and Propagation (EuCAP)*, pages 1–5, May 2015.

[50] F. Ferranti, D. Romano, G. Antonini, and L. D. Camillis. Stochastic collocation for uncertainty quantification of systems described by neutral delayed differential equations. In *2017 International Applied Computational Electromagnetics Society Symposium - Italy (ACES)*, pages 1–2, March 2017.

[51] A. Glisson and D. Wilton. Simple and efficient numerical methods for problems of electromagnetic radiation and scattering from surfaces. *IEEE Transactions on Antennas and Propagation*, 28(5):593–603, Sep 1980.

[52] S. Rao, D. Wilton, and A. Glisson. Electromagnetic scattering by surfaces of arbitrary shape. *IEEE Transactions on Antennas and Propagation*, 30(3):409–418, May 1982.

[53] S. M. Rao and D. R. Wilton. Transient scattering by conducting surfaces of arbitrary shape. *IEEE Transactions on Antennas and Propagation*, 39(1):56–61, Jan 1991.

[54] J. J. H. Wang. *Generalized Moment Method in Electromagnetics*. Wiley, 1991.

[55] B. M. Kolundzija and B. D. Popovic. Entire-domain Galerkin method for analysis of metallic antennas and scatterers. *IEE Proceedings H - Microwaves, Antennas and Propagation*, 140(1):1–10, Feb 1993.

[56] C. Gianfagna. *Time Domain Analysis of Electrical Systems through PEEC Method*. Doctoral dissertation, UniversitÃ degli Studi dell'Aquila, 2019.

[57] F. W. Grover. *Inductance calculations: Working formulas and tables*. Dover, 1962.

[58] P. A. Brennan, N. Raver and A. E. Ruehli. Three-Dimensional Inductance Computations with Partial Element Equivalent Circuits. *IBMJRD*, 23(6):661–668, Nov 1979.

[59] A. E. Ruehli and P. A. Brennan. Capacitance models for integrated circuit metallization wires. *IEEE Journal of Solid-State Circuits*, 10(6):530–536, Dec 1975.

[60] G. Antonini, A. Orlandi, and A. E. Ruehli. Analytical integration of quasi-static potential integrals on nonorthogonal coplanar quadrilaterals for the PEEC method. *IEEE Transactions on Electromagnetic Compatibility*, 44(2):399–403, May 2002.

[61] G. Antonini, A. E. Ruehli, and A. Haridass. Including dispersive dielectrics in PEEC models. In *Electrical Performance of Electrical Packaging (IEEE Cat. No. 03TH8710)*, pages 349–352, Oct 2003.

[62] G. Antonini, A. E. Ruehli, A. Haridass. Including dispersive dielectrics in PEEC models. In *EPEP*, pages 349–352, Princeton, NJ, USA, Oct 2003.

[63] G. Antonini, A. E. Ruehli, A. Haridass. PEEC Equivalent Circuits for Dispersive Dielectrics. In *PIERS*, Pisa, Italy, Mar 2004.

[64] A.E. Ruehli, J. Garrett, and C. Paul. Circuit models for 3D structures with incident fields. In *1993 International Symposium on Electromagnetic Compatibility*, pages 28–32, Aug 1993.

[65] Alfio Quarteroni, Riccardo Sacco, and Fausto Saleri. *Numerical Mathematics*. Springer, 2010.

[66] Y. Saad, M. Schultz. GMRES: A Generalized Minimal Residual Algorithm for Solving Nonsymmetric Linear Systems. *SIJSSC*, 7(3):856–869, 1986.

[67] N. Engheta, W. D. Murphy, V. Rokhlin, M. S. Vassilou. The fast multipole method (FMM). In *PIERS*, Jul 1991.

[68] R. Coifman, V. Rokhlin, and S. Wandzura. The fast multipole method for the wave equation: a pedestrian prescription. *IEEE Antennas and Propagation Magazine*, 35(3):7–12, June 1993.

[69] J. M. Song and W. C. Chew. Multilevel fast-multipole algorithm for solving combined field integral equations of electromagnetic scattering. *Microwave and Optical Technology Letters*, 10(1):14–19, 1995.

[70] G. Antonini and A. E. Ruehli. Fast multipole and multifunction PEEC methods. *IEEE Transactions on Mobile Computing*, 2(4):288–298, Oct 2003.

[71] J. R. Phillips and J. K. White. A precorrected-FFT method for electrostatic analysis of complicated 3-D structures. *IEEE Transactions on Computer-Aided Design of Integrated Circuits and Systems*, 16(10):1059–1072, Oct 1997.

[72] C.W. Ho, A.E. Ruehli, and P. Brennan. The modified nodal approach to network analysis. *IEEE Transactions on Circuits and Systems*, 22(6):504–509, Jun 1975.

[73] G. Antonini, D. Romano, L. Lombardi, and A.E. Ruehli. *Partial element equivalent circuit method in time-domain*, chapter Chapter 6, pages 181–216. 2024.

[74] B. P. Rynne, D. A. Vechinski, and S. M. Rao. Comments on "A stable procedure to calculate the transient scattering by conducting surfaces of arbitrary shape". *IEEE Transactions on Antennas and Propagation*, 41(4):517–520, April 1993.

[75] A. E. Ruehli, U. Miekkala, and H. Heeb. Stability of discretized partial element equivalent EFIE circuit models. *IEEE Transactions on Antennas and Propagation*, 43(6):553–559, Jun 1995.

[76] J. E. Garrett, A. E. Ruehli, and C. R. Paul. Accuracy and stability improvements of integral equation models using the partial element equivalent circuit (PEEC) approach. *IEEE Transactions on Antennas and Propagation*, 46(12):1824–1832, Dec 1998.

[77] J. Pingenot, S. Chakraborty, and V. Jandhyala. Polar integration for exact space-time quadrature in time-domain integral equations. *IEEE Transactions on Antennas and Propagation*, 54(10):3037–3042, Oct 2006.

[78] J. Ekman, G. Antonini, A. Orlandi, and A. E. Ruehli. Impact of partial element accuracy on PEEC model stability. *IEEE Transactions on Electromagnetic Compatibility*, 48(1):19–32, Feb 2006.

[79] A.E. Ruehli, U. Miekkala, A. Bellen, and H. Heeb. Stable time domain solutions for EMC problems using PEEC circuit models. In *Proceedings of IEEE Symposium on Electromagnetic Compatibility*, pages 371–376, Aug 1994.

[80] A. Bellen, N. Guglielmi, and A. E. Ruehli. Methods for linear systems of circuit delay differential equations of neutral type. *IEEE Transactions on Circuits and Systems I: Fundamental Theory and Applications*, 46(1):212–215, Jan 1999.

[81] E. Hairer and G. Wanner. *Solving Ordinary Differential Equations II, Stiff and Differential Algebraic Problems*. Springer-Verlag, New York, 1991.

[82] A. Bellen, M. Zennaro. Strong contractivity properties of numerical methods for ordinary and delay differential equations. *ANM*, 9:321–346, 1992.

[83] G. Antonini. Fast multipole method for time domain PEEC analysis. *IEEE Transactions on Mobile Computing*, 2(4):275–287, Oct 2003.

[84] M. E. Wall, A. Rechtsteiner, and L. M. Rocha. Singular value decomposition and principal component analysis. In *A practical approach to microarray data analysis*, pages 91–109. Springer, 2003.

[85] G. Berkooz, P. Holmes, and J. L. Lumley. The proper orthogonal decomposition in the analysis of turbulent flows. *Annual review of fluid mechanics*, 25(1):539–575, 1993.

[86] S. Gugercin and A. C Antoulas. A survey of model reduction by balanced truncation and some new results. *International Journal of Control*, 77(8):748–766, 2004.

[87] G. A. Baker Jr and J. L. Gammel. The Padé approximant. *Journal of Mathematical Analysis and Applications*, 2(1):21–30, 1961.

[88] C. Brezinski. *Padé-type approximation and general orthogonal polynomials*, volume 50. Springer, 1980.

[89] P.J. Schmid. Dynamic mode decomposition of numerical and experimental data. *Journal of fluid mechanics*, 656:5–28, 2010.

[90] A. C. Antoulas, S. Lefteriu, A. C. Ionita, P. Benner, and A. Cohen. A tutorial introduction to the loewner framework for model reduction. *Model Reduction and Approximation: Theory and Algorithms*, 15:335, 2017.

[91] P. Benner, S. Gugercin, and Karen Willcox. A survey of projection-based model reduction methods for parametric dynamical systems. *SIAM Review*, 57(4):483–531, nov 2015.

[92] C. W. Rowley, T. Colonius, and R. M. Murray. Model reduction for compressible flows using pod and galerkin projection. *Physica D: Nonlinear Phenomena*, 189(1-2):115–129, 2004.

[93] J.L. Lumley. The structure of inhomogeneous turbulent flows. *Atmospheric turbulence and radio wave propagation*, pages 166–178, 1967.

[94] D.D. Kosambi. Statistics in function space. *DD Kosambi: Selected Works in Mathematics and Statistics*, pages 115–123, 2016.

[95] M. Loève. Sur les fonctions aléatoires stationnaires du second ordre. *Revue Scientifique*, 83:297–303, 1945.

[96] K. Karhunen. Zur spektraltheorie stochastischer prozesse. *Ann. Acad. Sci. Fennicae, AI*, 34, 1946.

[97] S. Volkwein. Proper orthogonal decomposition: Theory and reduced-order modelling. *Lecture Notes, University of Konstanz*, 4(4):1–29, 2013.

[98] M. Rathinam and L. R. Petzold. A new look at proper orthogonal decomposition. *SIAM Journal on Numerical Analysis*, 41(5):1893–1925, 2003.

[99] K. Kunisch and S. Volkwein. Optimal snapshot location for computing pod basis functions. *ESAIM: Mathematical Modelling and Numerical Analysis*, 44(3):509–529, 2010.

[100] S. Lall, J. E. Marsden, and S. Glavaški. A subspace approach to balanced truncation for model reduction of nonlinear control systems. *International Journal of Robust and Nonlinear Control: IFAC-Affiliated Journal*, 12(6):519–535, 2002.

[101] C.P. Homme, D.V. Rovas, K. Veroy, L. Machiels, Y. Maday, A.T. Patera, and G. Turinici. Reliable real-time solution of parametrized partial differential equations: Reduced-basis output bound methods. *J. Fluids Eng.*, 124(1):70–80, 2002.

[102] U. Baur, C: Beattie, P. Benner, and S. Gugercin. Interpolatory projection methods for parameterized model reduction. *SIAM Journal on Scientific Computing*, 33(5):2489–2518, 2011.

[103] B.N. Bond and L. Daniel. A piecewise-linear moment-matching approach to parameterized model-order reduction for highly nonlinear systems. *IEEE Transactions on Computer-Aided Design of Integrated Circuits and Systems*, 26(12):2116–2129, 2007.

[104] T. Bui-Thanh, K. Willcox, and O. Ghattas. Model reduction for large-scale systems with high-dimensional parametric input space. *SIAM Journal on Scientific Computing*, 30(6):3270–3288, 2008.

[105] B. Haasdonk and M. Ohlberger. Reduced basis method for finite volume approximations of parametrized linear evolution equations. *ESAIM: Mathematical Modelling and Numerical Analysis*, 42(2):277–302, 2008.

[106] P. Benner, L. Feng, S. Li, and Y. Zhang. Reduced-order modeling and rom-based optimization of batch chromatography. In *Numerical Mathematics and Advanced Applications-ENUMATH 2013: Proceedings of ENUMATH 2013, the 10th European Conference on Numerical Mathematics and Advanced Applications, Lausanne, August 2013*, pages 427–435. Springer, 2015.

[107] C. Lieberman, K. Willcox, and O. Ghattas. Parameter and state model reduction for large-scale statistical inverse problems. *SIAM Journal on Scientific Computing*, 32(5):2523–2542, 2010.

[108] A. C. Antoulas. *Approximation of Large-Scale Dynamical Systems*. SIAM, 2005.

[109] E.J. Grimme. *Krylov Projection Methods for Model Reduction*. PhD thesis, University of Illinois at Urbana-Champaign, 1997.

[110] A. Odabasioglu, M. Celik, and L. T. Pileggi. PRIMA: Passive reduced-order interconnect macromodeling algorithm. *The Best of ICCAD: 20 Years of Excellence in Computer-Aided Design*, pages 433–450, 2003.

[111] P. Benner and T. Breiten. On H2-model reduction of linear parameter-varying systems. *PAMM*, 11(1):805–806, 2011.

[112] V. Druskin and V. Simoncini. Adaptive rational Krylov subspaces for large-scale dynamical systems. *SIAM Journal on Matrix Analysis and Applications*, 32(4):1185–1205, 2011.

[113] J. H. Mathews and K. K. Fink. *Numerical Methods Using MATLAB*. Prentice-Hall Inc., Upper Saddle River, New Jersey, 4th edition, 2004.

[114] G. A. Baker and P. Graves-Morris. *Padé Approximants*. Cambridge University Press, Cambridge, 2nd edition, 1996.

[115] D. C. Sorensen and A. C. Antoulas. Model reduction via balanced truncation and low-rank approximate gramians. *Numerical Algorithms*, 15(1):161–200, 1997.

[116] S. Gugercin, A. C Antoulas, and C. Beattie. $\mathcal{H}_2$ model reduction for large-scale linear dynamical systems. *SIAM journal on matrix analysis and applications*, 30(2):609–638, 2008.

[117] A. Ruhe. Rational krylov: A practical algorithm for large sparse nonsymmetric matrix pencils. *SIAM Journal on Numerical Analysis*, 21(5):1001–1014, 1984.

[118] K. Gallivan, A. Vandendorpe, and P. Van Dooren. Model reduction of MIMO systems via tangential interpolation. *SIAM Journal on Matrix Analysis and Applications*, 26(2):328–349, 2004.

[119] S. Melchior, V. Legat, and P. Van Dooren. Gramian based model reduction of nonlinear MIMO systems. *Proceedings of the Mathematical Theory of Networks and Systems, Melbourne, Australia*, pages 9–13, 2012.

[120] K. A. Gallivan, E. Grimme, and P. Van Dooren. Sylvester equation and the linear-quadratic optimal control problem. *Linear Algebra and its Applications*, 379:19–55, 2004.

[121] P. Benner and T. Breiten. Model reduction for parametrized systems. *Advances in Computational Mathematics*, 41(5):833–859, 2015.

[122] E. S. S. H. Sinha. Frequency-weighted balanced truncation. *IEEE Transactions on Automatic Control*, 46(8):1304–1309, 2001.

[123] H. Chen. Model reduction of nonlinear dynamical systems using balanced truncation. *Journal of Sound and Vibration*, 291(3-5):1047–1060, 2006.

[124] P. Benner, P. Kurschner, and J. Saak. Efficient handling of complex shift parameters in the low-rank Cholesky factor adi method. *Numerical Algorithms*, 62:225–251, 2013.

[125] P. Benner, J.R. Li, and T. Penzl. Numerical solution of large-scale lyapunov equations, Riccati equations, and linear-quadratic optimal control problems. *Numerical Linear Algebra with Applications*, 15:755–777, 2008.

[126] A. C. Antoulas and C. Beattie. System identification and model reduction using the loewner framework. *IEEE Transactions on Automatic Control*, 48(3):464–468, 2003.

[127] P. Benner and T. Breiten. Data-driven model order reduction for linear parametric systems. *SIAM Journal on Scientific Computing*, 37(1):A174–A194, 2015.

[128] P. Benner and T. Breiten. Low-rank methods for model order reduction of large-scale systems: A survey. *Computational Methods in Applied Mathematics*, 19(4):569–590, 2019.

[129] R. F. Harrington. *Field Computation by Moment Methods*. Wiley-IEEE Press, New York, 1968.

[130] A.E. Ruehli. Equivalent circuit models for three-dimensional multiconductor systems. *IEEE Transactions on Microwave Theory and Techniques*, 22(3):216–221, 1974.

[131] C. A. Balanis. *Advanced Engineering Electromagnetics*. Wiley-IEEE Press, New York, second edition, 2012.

[132] G. Antonini, A. E. Ruehli, D. Romano, and F. Loreto. The partial elements equivalent circuit method: The state of the art. *IEEE Transactions on Electromagnetic Compatibility*, 65(6):1695–1714, 2023.

[133] A. E. Ruehli, G. Antonini, and L. Jiang. *Circuit Oriented Electromagnetic Modeling Using the PEEC Techniques*. John Wiley & Sons, Inc., Hoboken, New Jersey., 2017.

[134] W. H. Schilders, H.A. Van Der Vorst, and J. Rommes, editors. *Model order reduction: Theory, research aspects and applications*. The European Consortium for Mathematics in Industry. Springer, Berlin, Germany, 2008 edition, aug 2008.

[135] D. Romano and G. Antonini. Partitioned model order reduction of partial element equivalent circuit models. *IEEE Transactions on Components, Packaging and Manufacturing Technology*, 4(9):1503–1514, 2014.

[136] M. A. Farhan, N. M. Nakhla, M. S. Nakhla, and R. Achar. Fast transient analysis of tightly coupled interconnects via overlapping partitioning and model-order reduction. *IEEE Transactions on Components, Packaging and Manufacturing Technology*, 4(10):1648–1656, 2014.

[137] T.S. Nguyen, T.L. Duc, T.S Tran, J.M. Guichon, O. Chadebec, and G. Meunier. Adaptive multipoint model order reduction scheme for large-scale inductive PEEC circuits. *IEEE Transactions on Electromagnetic Compatibility*, 59(4):1143–1151, 2017.

[138] Y. Dou and K.L. Wu. A passive peec-based micromodeling circuit for high-speed interconnection problems. *IEEE Transactions on Microwave Theory and Techniques*, 66(3):1201–1214, 2018.

[139] L. De Camillis, F. Ferranti, Giulio Antonini, Dries Vande Ginste, and Daniël De Zutter. Parameterized partial element equivalent circuit method for sensitivity analysis of multiport systems. *IEEE Transactions on Components, Packaging and Manufacturing Technology*, 2(2):248–255, 2011.

[140] W. Tseng, C. Chen, Emad Gad, M. Nakhla, and R. Achar. Passive order reduction for rlc circuits with delay elements. *IEEE Transactions on Advanced Packaging*, 30(4):830–840, 2007.

[141] F. Ferranti, M. S. Nakhla, G. Antonini, T. Dhaene, L. Knockaert, and A. E. Ruehli. Multipoint full-wave model order reduction for delayed peec models with large delays. *IEEE Transactions on Electromagnetic Compatibility*, 53(4):959–967, 2011.

[142] E. Rasekh and A. Dounavis. Multiorder Arnoldi approach for model order reduction of PEEC models with retardation. *IEEE Transactions on Components, Packaging and Manufacturing Technology*, 2(10):1629–1636, 2012.

[143] S. N. Lordejani, B. Besselink, A. Chaillet, and N. van de Wouw. Model order reduction for linear time delay systems: A delay-dependent approach based on energy functionals. *Automatica*, 112:108701, 2020.

[144] S. Naderi Lordejani, B. Besselink, A. Chaillet, and N. van de Wouw. *On Extended Model Order Reduction for Linear Time Delay Systems*, pages 191–215. Springer International Publishing, Cham, 2021.

[145] D. Alfke, L. Feng, L. Lombardi, G. Antonini, and P. Benner. Model order reduction for delay systems by iterative interpolation. *International Journal for Numerical Methods in Engineering*, 122(3):684–706, 2021.

[146] H. Heeb and A. E. Ruehli. Three-dimensional interconnect analysis using partial element equivalent circuits. *IEEE Transactions on Circuits and Systems I: Fundamental Theory and Applications*, 39(11):974–982, Nov 1992.

[147] M. Taskinen and P. Yla-Oijala. Current and charge integral equation formulation. *IEEE Transactions on Antennas and Propagation*, 54(1):58–67, Jan 2006.

[148] D. Gope, A. Ruehli, and V. Jandhyala. Solving low-frequency EM-CKT problems using the PEEC method. *IEEE Transactions on Advanced Packaging*, 30(2):313–320, 2007.

[149] F. Ferranti, M. S. Nakhla, G. Antonini, T. Dhaene, L. Knockaert, and A. E Ruehli. Multipoint full-wave model order reduction for delayed PEEC models with large delays. *IEEE Transactions on Electromagnetic Compatibility*, 53(4):959–967, 2011.

[150] J. Cullum, A.E. Ruehli, and T. Zhang. A method for reduced-order modeling and simulation of large interconnect circuits and its application to peec models with retardation. *IEEE Transactions on Circuits and Systems II: Analog and Digital Signal Processing*, 47(4):261–273, 2000.

[151] J. R. Phillips, E. Chiprout, and D. D. Ling. Efficient full-wave electromagnetic analysis via model-order reduction of fast integral transforms. In *Proceedings of the 33rd annual design automation conference*, pages 377–382, 1996.

[152] Y. Su, J. Wang, X. Zeng, Z. Bai, C. Chiang, and D. Zhou. SAPOR: Second-order Arnoldi method for passive order reduction of RCS circuits. In *Proc. IEEE Int. Conf. Comput.-Aided Design*, pages 74–79, San Jose, CA, nov 2004.

[153] Z. Bai and Y. Su. Dimension reduction of second-order large-scale dynamical systems via a second-order Arnoldi method. *SIAM J. Sci. Comput.*, 26(5):1692–1709, 2005.

[154] Z. Bai and Y. Su. SOAR: A second-order Arnoldi method for the solution of the quadratic eigenvalue problem. *SIAM J. Matrix Anal.*, 26(3):640–659, 2005.

[155] H. Wu and A. Cangellaris. Krylov model order reduction of finite element models of electromagnetic structures with frequency-dependent material properties. In *IEEE MTT-S Int. Microw. Symp. Dig.*, pages 52–55, jun 2006.

[156] B. Salimbahrami, R. Eid, and B. Lohmann. Model reduction by second order Krylov subspaces: Extensions, stability and proportional damping. In *Proc. IEEE Int. Symp. Intell.*, pages 2997–3002, oct 2006.

[157] K. Afanasiev and M. Hinze. Adaptive control of a wake flow using proper orthogonal decomposition. *Lecture Notes in Pure and Applied Mathematics*, 216:317–332, 2001.

[158] H. T. Banks, M. L. Joyner, B. Wincheski, and W. P. Winfree. Nondestructive evaluation using a reduced-order computational methodology. *Inverse Problems*, 16(4):929, 2000.

[159] P. Benner, E. Sachs, and S. Volkwein. Model order reduction for PDE constrained optimization. *Trends in PDE constrained optimization*, pages 303–326, 2014.

[160] M. A. Khattak, D. Romano, G. Antonini, and F. Ferranti. Proper orthogonal decomposition-based model order reduction of delayed PEEC models. In *2023 International Conference on Electromagnetics in Advanced Applications (ICEAA)*, pages 554–558. IEEE, 2023.

[161] M. A. Khattak, D. Romano, G. Antonini, and F. Ferranti. Efficient frequency and time-domain simulations of delayed PEEC models with proper orthogonal decomposition techniques. *IEEE Access*, 12:168–178, 2024.

[162] L. Sirovich. Turbulence and the dynamics of coherent structures. I. coherent structures. *Quarterly of Applied Mathematics*, 45(3):561–571, 1987.

[163] R. Mancini and S. Volkwein. An inverse scattering problem for the time-dependent maxwell equations: nonlinear optimization and model-order reduction. *Numerical Linear Algebra with Applications*, 20(4):689–711, 2013.

[164] Z. Luo and J. Gao. A pod reduced-order finite difference time-domain extrapolating scheme for the 2D Maxwell equations in a lossy medium. *Journal of Mathematical Analysis and Applications*, 444(1):433–451, 2016.

[165] T. Kim. Frequency-domain karhunen-loeve method and its application to linear dynamic systems. *AIAA journal*, 36(11):2117–2123, 1998.

[166] G. Dergham, D. Sipp, J. C. Robinet, and A. Barbagallo. Model reduction for fluids using frequential snapshots. *Physics of Fluids*, 23(6):064101, 2011.

[167] W. Wang, G. N. Paraschos, and M. N. Vouvakis. Fast frequency sweep of FEM models via the balanced truncation proper orthogonal decomposition. *IEEE Transactions on Antennas and Propagation*, 59(11):4142–4154, 2011.

[168] P. Benner, S Gugercin, and K. Willcox. A survey of projection-based model reduction methods for parametric dynamical systems. *SIAM Review*, 57(4):483–531, 2015.

[169] K.T. J. Gladwin and K.J. Vinoy. An efficient SSFEM-POD scheme for wideband stochastic analysis of permittivity variations. *IEEE Transactions on Antennas and Propagation*, 71(2):1654–1661, 2022.

[170] M. Brand. Fast low-rank modifications of the thin singular value decomposition. *Linear algebra and its applications*, 415(1):20–30, 2006.

[171] H. Fareed, J. R. Singler, Y. Zhang, and J. Shen. Incremental proper orthogonal decomposition for pde simulation data. *Computers & Mathematics with Applications*, 75(6):1942–1960, 2018.

[172] N. K´uhl, H. Fischer, M. Hinze, and T. Rung. An incremental singular value decomposition approach for large-scale spatially parallel and distributed but temporally serial data-applied to technical flows. *arXiv preprint arXiv:2302.09149*, 2023.

[173] J. Demmel, L. Grigori, M. Hoemmen, and J. Langou. Communication-optimal parallel and sequential QR and LU factorizations. *SIAM Journal on Scientific Computing*, 34(1):A206–A239, 2012.

[174] E. Rasekh and A. Dounavis. Multiorder arnoldi approach for model order reduction of PEEC models with retardation. *IEEE Transactions on Components, Packaging and Manufacturing Technology*, 2(10):1629–1636, 2012.

[175] The MathWorks Inc. Matlab version: 9.10.0 (r2021a), 2021.

[176] Jan R. Magnus and Heinz Neudecker. *Matrix differential calculus with applications in statistics and econometrics*. John Wiley & Sons, 2019.

[177] M. A. Khattak, D. Romano, M. Bandinelli, A. Mori, M. Bercigli, Giulio Antonini, and F. Ferranti. Proper orthogonal decomposition with derivatives for delayed PEEC models. In *4th URSI AT-RASC*, 2024.

[178] M. A. Khattak, D. Romano, G. Antonini, and F. Ferranti. Derivatives-enhanced proper orthogonal decomposition for PEEC models with delays. *IEEE Microwave and Wireless Technology Letters*, 34(10):1135–1138, 2024.

[179] The MathWorks Inc. Matlab version: 23.2.0 (r2023b), 2023.

[180] D. M. Pozar. *Microwave engineering: theory and techniques*. John wiley & sons, 2021.

Vita

Muhammad Altaf Khattak received a Bachelor's degree in Electrical Engineering from the National University of Computer and Emerging Sciences, Islamabad, Pakistan, in 2016 and completed a master's degree in Computational Sciences and Engineering from the National University of Sciences and Technology, Islamabad, Pakistan, in 2021.
From August 2020 to December 2021, he was a Research Assistant at the Research Center for Modeling and Simulation, Pakistan, focusing on computational engineering, model order reduction (MOR) of quadratic bilinear systems, and data-driven MOR of linear systems.
From 2022, he is working as a joint Ph.D. scholar at the Universitá degli Studi dell'Aquila, Italy and Vrije Universiteit Brussel, Belgium.

Tesi redatta con il sostegno finanziario del programma
FSE-REACT-EU, PON “Ricerca e Innovazione” 2014-2020 (D.M. 1061/2021)
Asse IV “Istruzione e ricerca per il recupero – REACT-EU”
Azione IV.5 “Dottorati e Contratti di ricerca su tematiche green”

